

Charged particle production in $p+p$ collisions at $\sqrt{s} = 200$ GeV

Bjørn H. Samset
Institute of Physics
University of Oslo
January, 2006



Dissertation presented for the degree of
Philosophia Doctor (PhD) in Physics

Preface

What happens when two heavy atomic nuclei collide at very close to the speed of light? Do they briefly melt into a new state of matter, the conditions inside this nuclear fireball approximating those of the entire universe just after the Big Bang? Do they fuse and form a miniature black hole, which then immediately evaporates due to Hawking radiation? Or is the whole collision just a sum of interactions between individual nucleons, and the fact that we are colliding big nuclei essentially irrelevant?

These are some of the central questions posed by *heavy ion physics*, a cross field between particle and nuclear physics that has been ever growing since the 1980s. Heavy ion physics is the study of the phase diagram of strongly interacting matter, and its main goal is to understand the properties of the strong nuclear force.

In this thesis are presented some more small pieces to fit into the puzzle. For the last four years, I have worked with the BRAHMS experimental collaboration, part of the RHIC accelerator group at Brookhaven National Laboratory in New York, on studying the production of charged particles in proton–proton ($p + p$) and deuteron–gold ($d+Au$) collisions at $\sqrt{s} = 200$ GeV. We study these ‘simpler’ collisions between single nucleons in addition to interactions between two heavy nuclei, because the former tell us what to expect from the latter if no new physics is present. Any deviation from this expectation tells us that we have seen something unknown and interesting. Such deviations in $d+Au$ collisions are the first topic of this thesis.

However, as I will show both in the introduction to the thesis and also in the reprinted papers, particle production in ‘simple’ proton–proton collisions is itself not fully understood. This is especially true away from midrapidity, and many interesting features can be seen in the data. In interpreting comparisons of $p + p$ collisions to $Au+Au$, it is easy to make implicit assumptions on the similarity of the physics of the two systems at the same center-of-mass energy. If these assumptions turn out to be wrong, so may our conclusions. We therefore need a thorough study also of $p + p$ collisions, so that comparisons can be safely made.

In other words the nucleon–nucleon interaction at high energy is doubly interesting, as it is both a relatively clean system in which to study the strong nuclear force, and a means with which to understand the immensely complex interactions that occur in an ultrarelativistic heavy ion collision. The second topic of this thesis is a thorough study of bulk particle production, both identified and unidentified, in $p + p$ collisions at $\sqrt{s} = 200$ GeV.

How this thesis is organized

The main results in this thesis are presented in a self contained way as four papers in chapter 5. Three are already published, while the fourth is being finalized for publication by the collaboration at this time. The first paper discusses results on the rapidity dependence of the nuclear modification factor in deuteron–on–gold collisions, i.e. collisions between a light and a heavy system. This was the first major analysis effort I collaborated on as part of my PhD work. The second paper is a conference proceeding where I discuss the results in the first paper together with other BRAHMS results. Later in my work I have focused on the $p + p$ collisions recorded by BRAHMS in 2001/2002, and the third paper presents an analysis of the rapidity dependence of charged like–particle ratios from this system. The fourth paper then presents normalized identified particle production as a function of rapidity and transverse mass in $p + p$ collisions at $\sqrt{s} = 200$ GeV, and discusses some related results on unlike–particle ratios, baryon stopping and mean transverse momenta.

This thesis is also intended to serve two purposes in addition to presenting the results in the papers. Firstly, it serves as a thorough documentation of my analysis on $p + p$ collisions for the BRAHMS collaboration. Secondly, as it is already clear that other students in Oslo will follow up on the results presented here, I hope that it can serve as a guide to some of the main theoretical and experimental topics connected with the study of such collisions.

Consequently, the rest of the thesis is organized as follows: Chapter 1 introduces the field of heavy ion physics and some relevant terminology, and gives a brief summary of the main results from RHIC at this time. Chapter 2 then focuses on proton–proton collisions, discussing the most accepted theoretical description of soft particle production in such events. I also review some results from other experiments and accelerators, and a number of model calculations. Chapter 3 discusses the BRAHMS experimental setup, and chapter 4 gives details of the data analysis leading up to the results in the $p + p$ papers, which are reprinted in chapter 5. A brief introduction to the papers is also given here. Chapter 6 then summarizes the main conclusions, and draws some lines towards the next generation of heavy ion experiments at the LHC. Finally, the appendices contain some background kinematics and mathematics, a detailed description of the estimation of nuclear stopping discussed in the fourth paper, and a short writeup on the SNAccPack geometrical acceptance generation software I have written for the BRAHMS collaboration.

Acknowledgments

BRAHMS consists of approximately 50 physicists from 11 institutions in Europe and the United States, and over the last five years (MSc and PhD studies) I have had the pleasure of working with many of them. This has been a very rewarding experience, both educationally and on a more personal level. BRAHMS is a very easy-going collaboration, where a young student can grab a project that looks interesting and really get a lot of support for what he wants to do. So first of all, a great Thank You to all of BRAHMS. It's been great.

Then, of course, some special people deserve special mention. My supervisors in Oslo, Trine Tveter and Gunnar Løvholden, have taught, helped and supported me for many years now — thank you very much, both for good discussions and for good beer all over the world. The BRAHMS spokesman, Flemming Videbaek, has given me a lot of help and support both during my visits to BNL and at other times. At the Niels Bohr Institute, Ian Bearden has long been a motivating factor for me (even when not wielding an axe), and arranged for me to work there for a semester in 2003. Also at NBI, the PhD students Peter H. L. Christiansen, Djamel Ouerdane and Claus E. Jorgensen have taught me a great deal. They did the first major analyses of BRAHMS data and had to lay much of the groundwork, and this work is in turn echoed in the methods and discussions in this thesis. Thanks Danes, natural or not.

On the social side, from now on no office will ever feel complete without the presence of Thomas Vik, master of the Kalman Filter and guitar virtuoso. Also a heap of thanks to the Disciples of Tugor Hostegym, for giving me other things to think of now and then. New York will never be the same. . .

Finally but most importantly, I have in the last four years gotten both a wife and a daughter who make life worth living. For them, this finished thesis means they'll be getting a more attentive husband and father again - thank you for your patience while I wrote it. Spille sokk?

–Bjørn H. Samset

January 2006

Contents

I	Introduction, background and analysis details	1
1	Heavy Ion Physics	3
1.1	Elementary particles, strong interactions and melted nuclei	3
1.2	Geometry and evolution of a heavy ion collision	9
1.3	Selected results from RHIC	13
2	Proton–proton collisions	23
2.1	Theoretical description of a $p + p$ collision	23
2.2	The string model of hadronic interactions	25
2.3	Diquarks, junctions and fragmented physics	26
2.4	Monte Carlo and statistical modeling of $p + p$ events	28
2.5	Available data	34
3	The BRAHMS experimental setup	39
3.1	The Relativistic Heavy Ion Collider	39
3.2	BRAHMS detector overview	41
3.3	Global detectors	44
3.4	Trigger systems	46
3.5	Tracking detectors	46
3.6	Magnets	48
3.7	Time–of–flight systems	48
3.8	Cherenkov detectors	50
4	Analysis of the 2001 $p + p$ dataset	53
4.1	Data reduction	53
4.2	Particle identification	56
4.3	Analysis cuts	60
4.4	Corrections	63
4.5	Total corrections and data set combination	75
4.6	Final $d^2N/dydp_T$ maps	77
4.7	Like–particle ratios	79
4.8	Particle spectra	79
4.9	Fitting the spectra	81
4.10	Systematic errors	81

II	Papers and conclusions	87
5	Brief introduction to the papers	89
5.1	On the evolution of the nuclear modification factors with rapidity and centrality in $d + Au$ collisions at $\sqrt{s} = 200$ GeV	89
5.2	The rapidity and centrality dependence of nuclear modification factors at RHIC: What does bulk particle production tell us about the nuclear medium?	90
5.3	Forward and midrapidity like-particle ratios from $p + p$ collisions at $\sqrt{s} = 200$ GeV	90
5.4	Rapidity dependence of charged particle production from $p + p$ collisions at $\sqrt{s} = 200$ GeV (in preparation)	91
6	Conclusions and outlook	93
6.1	Conclusions	93
6.2	Outlook	94
III	Appendices	97
A	Kinematics and mathematics	99
A.1	Kinematic formulas	99
A.2	Invariant cross section and transverse momentum	100
A.3	Fit functions	101
A.4	Merging vertex bins and settings	102
B	BRAHMS spectrometer resolution	105
B.1	Angular and momentum resolution	105
B.2	Transverse momentum resolution	106
C	Estimating net-baryon production and stopping	109
C.1	Estimating the net-baryon distribution	109
C.2	Fit functions and results	112
D	SNAccPack, an acceptance package for BRAHMS	115
D.1	SNAccPack basics	115
D.2	Example maps	116
E	The BRAHMS collaboration	119
	List of figures	125
	Bibliography	133

Part I

Introduction, background and analysis details

Chapter 1

Heavy Ion Physics

The main goal of heavy ion physics is to better understand the strong nuclear force [1, 2]. But what is this force, where is its place in nature, and how much do we really know about it today?

This introductory chapter sets the stage for the main work of this thesis, by reviewing our understanding of how nature works at its smallest scales and discussing Quantum Chromo Dynamics (QCD), the current theory describing the strong force. Heavy ion physics is discussed in general terms, and a short review is given of some important results from the RHIC accelerator up to the present time, with a focus on physics related to what will be discussed in subsequent chapters.

1.1 Elementary particles, strong interactions and melted nuclei

Ever since the birth of natural philosophy, people have asked the question 'If I divide matter up into smaller and smaller pieces, do I eventually reach some smallest constituent of nature? Are there a set of simple building blocks that make up all that I see around me?' Since then a wide variety of answers have been given, and over the last 150 years it has been the domain of different branches of physics.

In the late 19th century, nature was supposed to be built of a number of different species of *atoms*, each the smallest part of a natural element. Examples are hydrogen, helium, lithium and all the other substances that today make up the periodic table of the elements. Elementarity was then the domain of atomic physics and chemistry.

Then, in 1911, Ernest Rutherford discovered the atomic nucleus, and in a while it was understood that an atom is composed of a very small but very massive core orbited in some fashion by extremely light particles called electrons. By 1932, it was also known that the

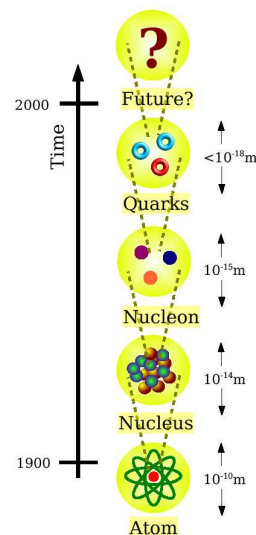


Figure 1.1: Elementarity, a history

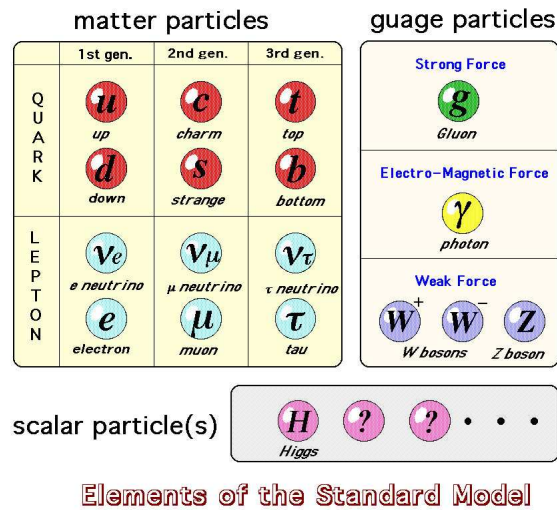


Figure 1.2: The elements of the Standard Model. Figure from [4].

nucleus was composed of two species of particle, the proton and the neutron. Elementarity was now discussed by the nuclear physicists.

After this a wide variety of small particles were discovered, that did not fit into the neat picture of everything being composed of atoms, in turn made up electrons, protons and neutrons. Some of these were found to be truly elementary, at least to our present knowledge, while many were composites of yet smaller particles — the quarks. At this point, what is elementary is studied by the field of particle physics.

The basic building blocks of matter

Today, most of what we know about the subatomic world is contained in the so-called *Standard Model of Particle Physics* (SM). (For a full description, see e.g. [3].) The SM lists all the particles that, to the best of our present knowledge, are elementary, how they can interact with each other and the forces that govern these interactions. See figure 1.2 for a concise listing of the elements of the model.

The Standard Model has three main elements — the quarks, the leptons and the gauge particles, or force carriers. The quarks are what build up most of ordinary matter, since both the protons and the neutrons of normal atomic nuclei consist of up- and down-quarks. In addition we have found four other heavier quarks, known as strange, charm, top and bottom.¹ The top was found only in 1995, the latest elementary particle to be discovered.

The lepton group consist firstly of the electron, the particle that orbits ordinary atomic nuclei and is what moves in an 'electric current' in solid matter, and its heavier relatives, the muon (μ) and the tau (τ). In addition, the three neutrinos (ν_e, ν_μ, ν_τ) are leptons. These neutral particles interact only through the weak nuclear force, and are therefore very hard to detect. They were long thought to be massless, but in 1998 it was found that they do indeed have a small mass [5].²

¹Another common name pair for this quark duo is *truth* and *beauty*.

²While this may solve long standing puzzles like the solar neutrino problem, it poses a problem for the

Finally, the gauge bosons are the force carriers of the theory. Currently the SM describes the electromagnetic force and the weak and strong nuclear forces. The electromagnetic and weak forces are combined into one unified description, known as the electroweak force, which is mediated by the photon and the W^+ , W^- and Z^0 bosons. Electroweak interactions are described theoretically by Quantum Electrodynamics (QED), the most precise theory in all of physics to date.³ The final gauge boson, the gluon, of which there are actually eight versions, is then what mediates the strong nuclear force. A theory of the strong interaction, Quantum Chromodynamics (QCD), also exists, but here numerical results are not so impressive due to its complex and intractable mathematical properties. The strong nuclear force is discussed in the next section, and indeed throughout this thesis.

Before moving on, note that there is one final section in figure 1.2, labeled 'scalar particles(s)', that has not been discussed. For the matter particles interacting through the electroweak force to have mass in the theory, as we know they do in nature, the Standard Model requires the existence of another boson, known as the Higgs particle. While actively sought for at several accelerator complexes, this boson has not yet been seen experimentally. Also note that we have not mentioned the fourth fundamental force of nature, gravity. No one has as of yet produced a quantum description of gravity, and therefore it is not part of the SM. Hence, and for a number of other reasons, while the SM is an extremely successful theory it is not the final description of the subatomic world (for a recent popular account of the successes and problems of the SM, see [7]). The search for nature's elementary building blocks and their behavior will continue.

Quantum Chromodynamics and the strong nuclear force

Interactions of hadrons, or particles composed of quarks, are dominated by the strong nuclear force, mediated by gluons. The strong interaction is described theoretically by Quantum Chromodynamics (QCD) which dictates the characteristic structure of hadronic matter.

The word *chromo* reflects that QCD introduces a charge called color, carried by both quarks and gluons. Quarks carry a single unit of color charge, while gluons carry a (possibly non-neutral) combination of one color and one anti-color charge unit. These color charges are usually named red, green or blue (or the corresponding anti-charges). Colored particles interact strongly, and the fact that gluons are colored, as opposed to the electrically neutral photon in QED, has important implications for the structure of hadronic matter. The gluon-gluon coupling leads to a complicated form of the strength of the interaction, known as the running coupling constant. As the momentum transfer between strongly interacting particles (usually denoted Q^2) becomes larger, (or, from uncertainty principle, the distance shorter) the effective coupling $\alpha_s(Q)$ becomes smaller and vice versa, as shown in figure 1.3⁴. The effective potential between two colored objects grows linearly with distance in the strong coupling regime, i.e. at large distances,

conventional Standard Model since the neutrinos here are assumed to be massless. This can, however, be remedied by extending the SM somewhat. See e.g. [6] for a review.

³It has been shown to reproduce experimental results with up to 12 decimal points precision, in measurements of the electron magnetic dipole moment [3].

⁴For this discovery, the 2004 Nobel Prize in physics was awarded to David J. Gross, H. David Politzer and Frank Wilczek.

and is therefore very different from the potentials of the other fundamental forces which all go asymptotically to 0 as the distance increases.

When the quarks approach each other, the effective coupling becomes weaker and at very small distances it almost vanishes. This is called the *asymptotic freedom* of QCD. When the distance between quarks grows, the effective coupling grows and at some point the energy becomes large enough to form a new quark–antiquark pair. These new quarks combine with the original ones and new hadrons are formed. Intuitively, one can think of the color field between the quarks as confined in a small tube which acts much like a rubber band. The gluon-gluon interaction makes the tube radius approximately constant. Eventually the tube breaks and energy is converted into new particles, one at each side of the break point. One consequence of this is that a single quark cannot be observed – quarks are confined in systems of two or more quarks, namely the hadrons. These systems are colorless, which means that they either contain the same amount of all three color charges (red, green and blue) or the same number of color and anti-color charges. The common configurations of valence quarks are $q_r q_g q_b$ (baryons) or $q_c \bar{q}$ (mesons), but both QCD calculations and recent measurements indicate the existence of short lived configurations of five quarks. (See [9] and refs. therein). The baryons and mesons also contain a large number of virtual quarks (the sea quarks) and a number of gluons that bind the quarks together.

In the large momentum transfer regime (hard scattering processes) perturbation theory can be applied and perturbative QCD (pQCD) calculations show good agreement with data (see e.g. figure 2.13 on page 38). However, in the small momentum transfer regime (soft processes) the perturbative approximation is not valid. In this regime, QCD calculations can still be performed by solving the QCD Lagrangian path integrals numerically on a discretized lattice in space-time – this is called lattice QCD (lQCD, for a review see ref. [10]). While lQCD in principle can calculate interactions over the whole Q^2 range, in practice crude approximations are needed in order to achieve reasonable simplicity of the numerical algorithms and computation times. Therefore the results from QCD lattice calculations are still somewhat uncertain. Also, a non vanishing baryon chemical potential complicates the calculations. It has only recently become possible to investigate this domain [11].

One of the early successes of lattice QCD calculations was the prediction that quark matter under normal conditions (densities and temperatures like in an atomic nucleus) will have the known structure with the quarks confined in hadrons [12].

It should be noted, however, that lattice QCD calculations give the properties of static equilibrated systems and can therefore not model the dynamics of heavy ions collisions which evolve on short time scales.

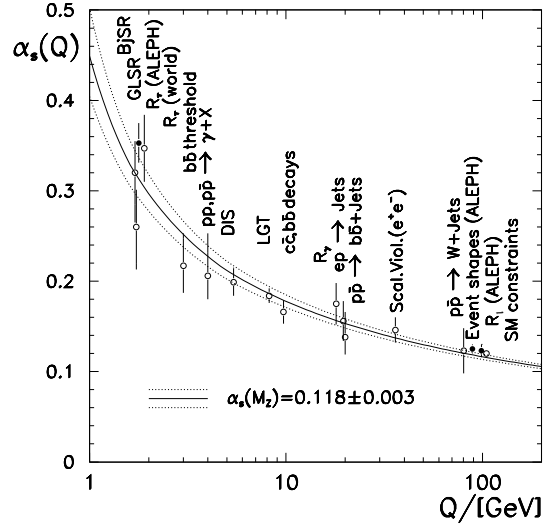


Figure 1.3: The strong coupling constant α_s as function of momentum transfer Q^2 . The plot is from ref. [8]

The structure of the nucleon

In the simplest view, an atomic nucleus consists of protons and neutrons, which in turn are built up of up and down quarks bound by gluons. The real picture is however more complicated, with the nucleons consisting of three valence quarks and a number of sea quarks, in addition to a very significant gluon component.

The detailed structure of the nucleons is studied in deep inelastic scattering experiments $e + p \rightarrow e + X$, e.g. at the HERA accelerator complex at DESY. They measure the so-called parton density functions (PDFs), or structure functions of the nucleons, which reveal the average contribution of the various partons to the composite particle. The measurements are made as function of the x variable, defined as the fraction of the nucleon momentum carried by the given parton, and of the momentum transfer Q^2 between the incident electron and the struck parton. The structure of the nucleon is found to be very different at different Q^2 scales.

Figure 1.4 shows a recent set of PDFs for the proton, incorporating NNLO⁵ QCD as well as QED contributions. Ref. [14] has more experimental data from the ZEUS collaboration, showing e.g. the Q^2 dependence of the PDFs. It is clear that at $Q^2 = 20\text{GeV}^2$, while there is still a large contribution from the valence u and d quarks, both sea quarks ($\bar{u}, \bar{d}, s, c, b$) and photons contribute significantly to the total makeup of the nucleon, and the gluon contribution is actually dominant below $x \sim 10^{-1}$.

This detailed picture of the nucleon and its evolution with Q^2 is naturally relevant for the understanding of heavy ion collisions, as the high-energy nucleon is the basic component of the reaction initial state. This will be discussed further at the end of this chapter, in the introduction to chapter 5 as well as in the two first reprinted papers.

The nuclear phase diagram and the Quark Gluon Plasma

Before the quark model and QCD were formulated, an upper temperature limit of hadronic matter in the normal state was proposed [15]. The arguments came from the observed rapid growth in the number of hadronic resonance states with the temperature of hadronic matter. The number of states indicated a divergent behavior with an upper temperature around $T_H \sim 165\text{MeV}$ – this is known as the Hagedorn limit.

Lattice QCD has confirmed this upper temperature limit of normal nuclear matter. The behavior of modeled thermodynamical quantities clearly shows the existence of a phase transition between a hot hadron gas and a so-called quark gluon plasma. Figure 1.5 shows the energy density ε divided by the temperature T to the fourth power as a

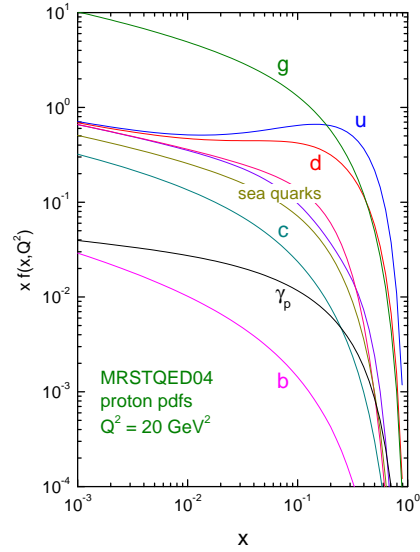


Figure 1.4: Proton parton density function vs. x at $Q^2 = 20\text{GeV}^2$, from [13]. The unlabeled 'sea quark' lines correspond to \bar{u}, \bar{d} and s respectively (top-to-bottom).

⁵NNLO = next-to-next-to-leading order.

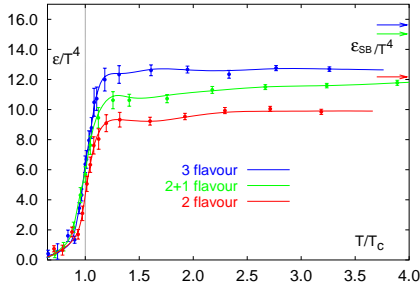


Figure 1.5: Lattice QCD calculations show that the number of thermodynamic degrees of freedom shows a drastic increase around the certain temperature (the critical temperature T_c). Stefan-Boltzmann temperature limits. The plot is from ref. [16].

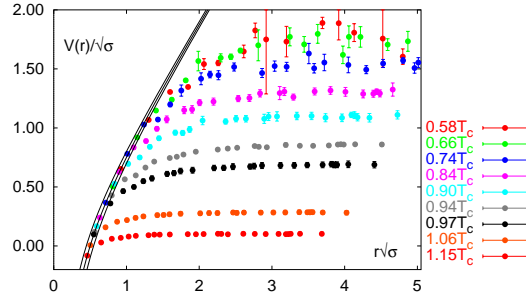


Figure 1.6: The effective quark-quark potential as function of distance for different fractions of the critical temperatures (both axis are normalized by the string tension $\sqrt{\sigma}$). The two lowest curves are for temperatures above the critical. The plot is from ref. [16].

function of the fraction of the critical temperature. The quantity ϵ/T^4 is proportional to the number of thermodynamic degrees of freedom of the system. A dramatic increase is seen around the critical temperature where the phase changes from confined to deconfined quark matter: the relevant degrees of freedom are no longer hadronic but partonic.

In the partonic environment, when the quarks are closely surrounded by many freely moving color charges, the quark–quark potential is screened. A similar effect is known in Quantum Electrodynamics, the Debye screening in a plasma of ions and electrons. The effective quark–quark potential becomes constant (flattens out) at some distance, which depends on the energy density. Figure 1.6 shows a lattice QCD study of this effect.

QCD also predicts the so called chiral symmetry restoration. As the energy density rises, the coupling between the quarks diminish due to the increase in mean momentum transfer. This has the consequence that the number of virtual quarks and gluons decreases (the quark condensate becomes less dense), and the light quarks lose their *constituent mass* and become nearly massless — so-called bare quarks. One commonly discussed possible signature for such a transition is the modification of vector meson masses, e.g. the ρ . In the limit of no masses, the left- and righthanded quarks⁶ decouple leading to a degeneracy in quark states of opposite parity. The QCD Lagrangian now has two symmetric terms describing the left- and right-handed quarks, a property known as chiral symmetry (the word *chiral* is Greek and simply refers to the handedness of the particles). At low energy density, when the quarks are confined, the symmetry is broken and the hadrons regain their non-degenerate masses.

Figure 1.7 summarizes these results as the *phase diagram of strongly interacting matter*. It plots the temperature as a function of the baryochemical potential μ_B , and includes both statistical parameters extracted from experimental data (see sec. 2.4) and predictions from theoretical modeling of heavy ion interactions. Dynamic collisions of strongly interacting systems and their relation to the study of the strong nuclear force are

⁶The *handedness* of a fermion refers to the direction of its spin relative to its momentum. For a righthanded particle they point in the same direction, for a lefthanded particle they are opposite.

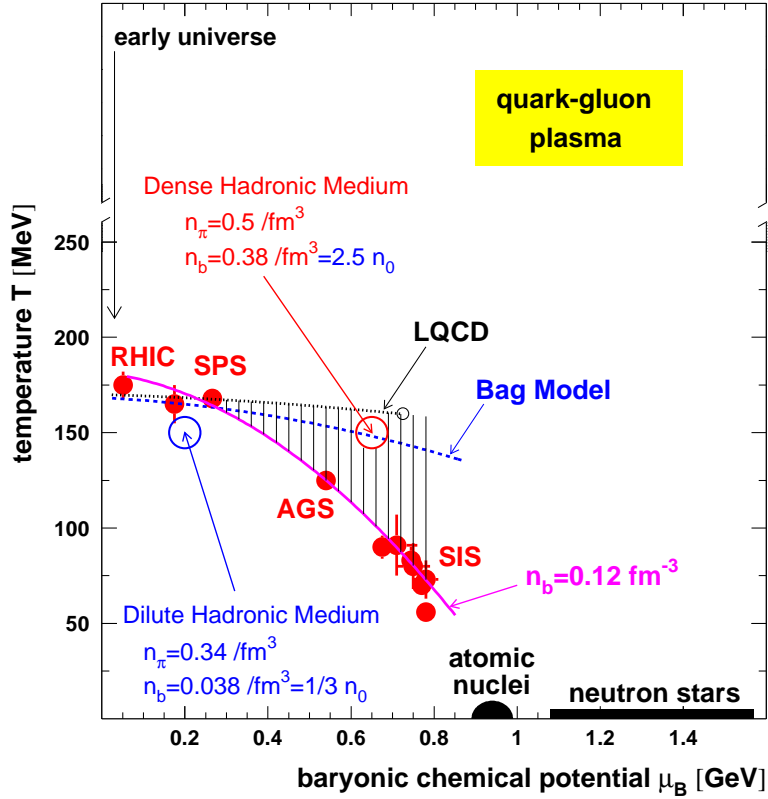


Figure 1.7: Phase diagram for nuclear matter. Temperature as function of the baryo-chemical potential extracted using a statistical model (figure from ref. [17]). Points show experimental results from various accelerators.

the subject of the next section.

Note that figure 1.7 also includes entries for neutron stars, which are thought to be extremely dense but at essentially zero temperature, and for the early universe. This refers to the state of the whole universe just fractions of a second after the Big Bang, when there was a high energy density (i.e. high temperature) but no net baryon density. A study of the nuclear phase diagram therefore also touches on these astrophysical subjects.

1.2 Geometry and evolution of a heavy ion collision

We have seen that QCD predicts the formation of a deconfined state of matter at extreme temperatures and/or densities, known as the Quark Gluon Plasma. Experimental attempts to create the QGP in the laboratory and measure its properties have been carried out for more than 20 years, by studying collisions of heavy nuclei and analyzing the fragments and produced particles emanating from such collisions.⁷ During that period, center of

⁷For a review of the most important kinematic variables used in the discussion below, e.g. \sqrt{s} , rapidity and transverse mass, see appendix A on page 99.

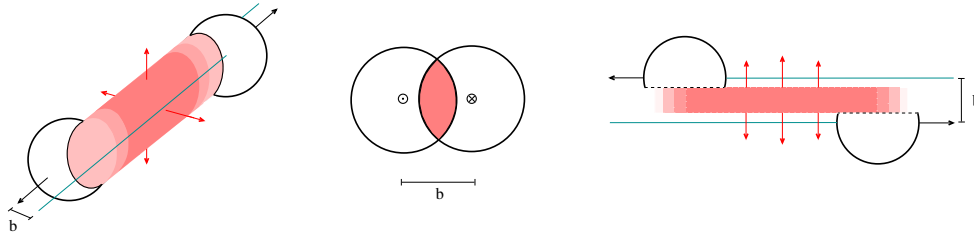


Figure 1.8: Schematic drawing of the geometry of a symmetric collision. The nuclei are depicted as hard spheres. The collisions is seen in perspective (left drawing), from the beam axis (middle drawing) and from the top (right drawing). Figure from [21].

mass energies per pair of colliding nucleons have risen steadily from the $\sqrt{s_{NN}} \approx 1$ GeV domain of the Bevalac at LBNL, to energies of $\sqrt{s_{NN}} = 5$ GeV at the AGS at BNL, and to $\sqrt{s_{NN}} = 17$ GeV at the SPS accelerator at CERN.

No decisive proof of QGP formation was found in the experiments at those energies, although a number of signals suggesting the formation of a "very dense state of matter" were found at the SPS [18, 19]. CERN is also where Large Hadron Collider (LHC) is under construction and is expected to start operations in 2007. Recent reviews of AGS and SPS physics can be found in ref. [20, 18].

This thesis will focus on heavy ion physics in the RHIC energy regime. At the Relativistic Heavy Ion Collider, RHIC, at Brookhaven National Laboratory, the center of mass energy in central collisions between gold nuclei at $100 \text{ AGeV} + 100 \text{ AGeV}$ is almost 40 TeV , the largest so far achieved in nucleus-nucleus collisions under laboratory conditions. This energy is so large that conversion of a sizable fraction of the initial kinetic energy into matter production creates many thousands of particles in a limited volume, leading to unprecedented energy densities and thus presumably ideal conditions for the formation of the quark gluon plasma. See section 3.1 for more details on the RHIC accelerator.

Collision centrality

Figure 1.8 shows a schematic drawing of a heavy ion collision at very high energy. The nucleons outside the overlap region (parallel to the beam axis) are called the spectators. After the collision, they move on with their initial momentum and fragment into smaller systems with little transverse momentum. The nucleons inside the overlap region are called the participants, and the ones that do not interact are known as spectators. The number of participants is related to the overlap volume and thus to the impact parameter, b , defined as the transverse distance between the centers of the colliding nuclei (see figure 1.8b). Note that for collisions with $b > 0$ we can define a plane from the beam axis and the vector between the centers of the colliding nuclei. This is known as the *reaction plane*.

The impact parameter cannot be directly measured – instead an experimental quantity, the centrality c , is used. Typically, the measured charged particle multiplicity is used to define the centrality. Collisions that give a charged particle multiplicity among the $N\%$ highest (of all inelastic collisions) have $c \leq N\%$. Normally, data from A+A collisions is presented in different centrality bins, for example $0 - 5\%$ or $20 - 40\%$. There will be

fluctuations in the number of produced particles for collisions with a given impact parameter. This means that the impact parameter distribution for events of a given centrality will have a certain intrinsic width. No centrality is defined for $p + p$ collisions, but they are sometimes subdivided into bins according to the total multiplicity of charged particles from a single event. While this does not have the same geometrical interpretation as shown in fig. 1.8, it is used in the same way to group events with similar properties.

Figure 1.9 shows the total charged particle multiplicity as a function of the impact parameter for Au+Au collisions at $\sqrt{s_{NN}} = 200$ GeV as given by the HIJING model [22]. The horizontal lines in the upper panel indicate different centralities and the lower panel shows the corresponding impact parameter distributions. It is clear, that for peripheral collisions, the centrality defined from the charged particle multiplicity gives large overlaps in the impact parameter distributions. When studying peripheral collisions, centrality can be defined from the correlation between charged particle multiplicity and the number of measured spectator neutrons at very small angles.

For A+A collisions two quantities, the number of participants N_{part} and the number of binary collisions N_{coll} , are often used instead of centrality (or as normalization parameters). The number of participants is simply the number of participating nucleons, i.e. the nucleons in the transverse overlap region of the two nuclei which suffer at least one interaction. The number of binary collisions is calculated by letting the two nuclei pass each other and, for each nucleon, count how many nucleons (from the other nuclei) it collides with. The number of binary collisions is then the sum of all the nucleon–nucleon collisions. The number of participants and number of binary collisions are normally derived using the so called Glauber approach. For details on this, see e.g. refs. [21, 23, 24].

Stopping vs. transparency

Once we know the amount of nuclear matter that will interact, we wish to know to what extent they stop each other at the point of impact. This relates to the total amount of energy available in the original fireball.

Figure 1.10 sketches two extreme scenarios. In the upper panel, two nuclei collide but pass straight through each other, leaving a zone of highly excited color strings at the center-of-mass rapidity y_{CM} . This collision view was first discussed by Bjorken in 1983 [25], and is known as the 'transparent' or simply 'Bjorken' scenario. It leads to a midrapidity region free of net baryon number, meaning that all particles in this region

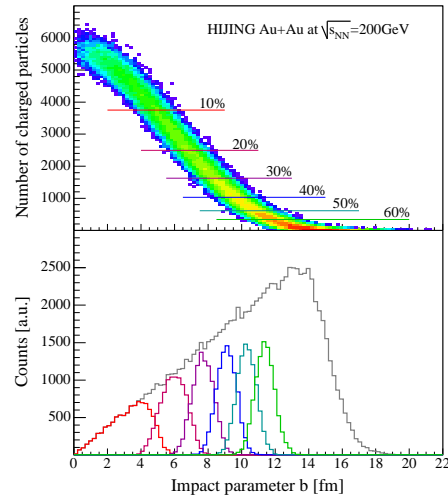


Figure 1.9: Upper panel: Total charged particle multiplicity versus impact parameter from the HIJING model. Lower panel: Impact parameter distributions for different centrality classes as selected from the charged particle multiplicity.

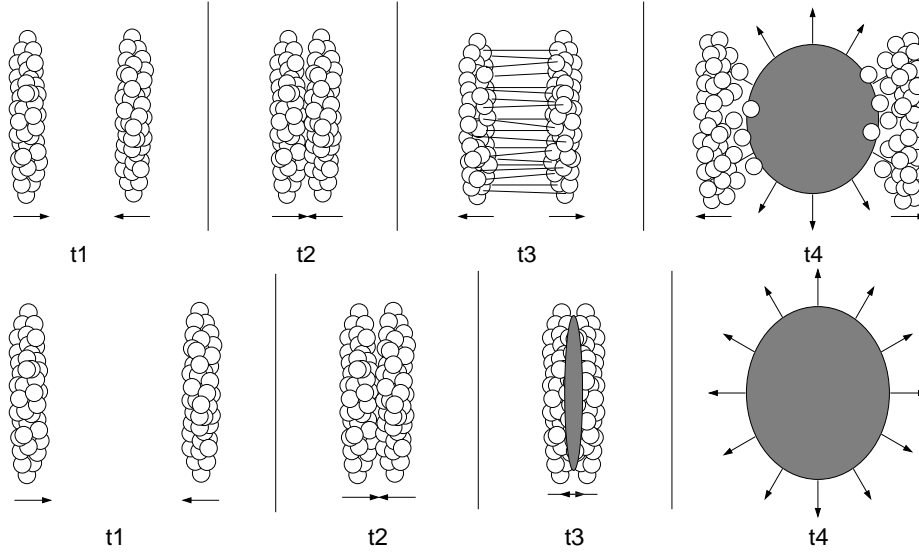


Figure 1.10: Two views of a central heavy ion collision. Upper panel: The so-called 'Bjorken scenario', where the nuclei pass through each other leaving only color strings, yielding a midrapidity region with vanishing net baryon number. Lower panel: The opposite scenario, where the nuclei are completely stopped at the point of impact. This yields a baryon rich midrapidity region. Figures from [23].

are produced from the breakup of the color strings.⁸ The lower panel shows the opposite possibility, where the colliding nuclei stop each other completely at y_{CM} and then expand collectively as a fireball. This yields a lot of available energy for reactions, but also a large net-baryon density that must be conserved. This view is known as the 'full stopping' scenario, or sometimes the 'Landau scenario' as this was the kind of fireballs discussed by Landau for his first hydrodynamical calculations of particle production in heavy ion collisions [26].

The degree of stopping seen at RHIC will be discussed below for Au+Au collisions, and then in the fourth paper in chapter 5 and in appendix C for $p + p$ collisions.

Collision evolution — the 'little bang'

Figure 1.11 lists the present understanding of the different stages in the evolution of a heavy ion collision at RHIC energy. The observations related to the different stages are listed on the right.

After the initial collision, a cylindrical zone of high energy density is built up between the fragments of the initial nuclei. Measurements of the elliptic flow indicate that shortly after the initial collisions ($t \lesssim 1 \text{ fm}/c$) the partonic matter interacts strongly and is highly thermalized. Here, elliptic flow refers to the anisotropic collective movement of the produced particles due to the pressure gradient set up in a non-central collision — see sec. 1.3 below. This hot and dense zone expands and cools down. Around $t \sim 5 \text{ fm}/c$ hadrons are created. The hadrons are either created in chemical equilibrium or they reach it quickly in the strongly interacting hadron gas. A large pressure gradient is built

⁸For more on the string model, see chapter 2.

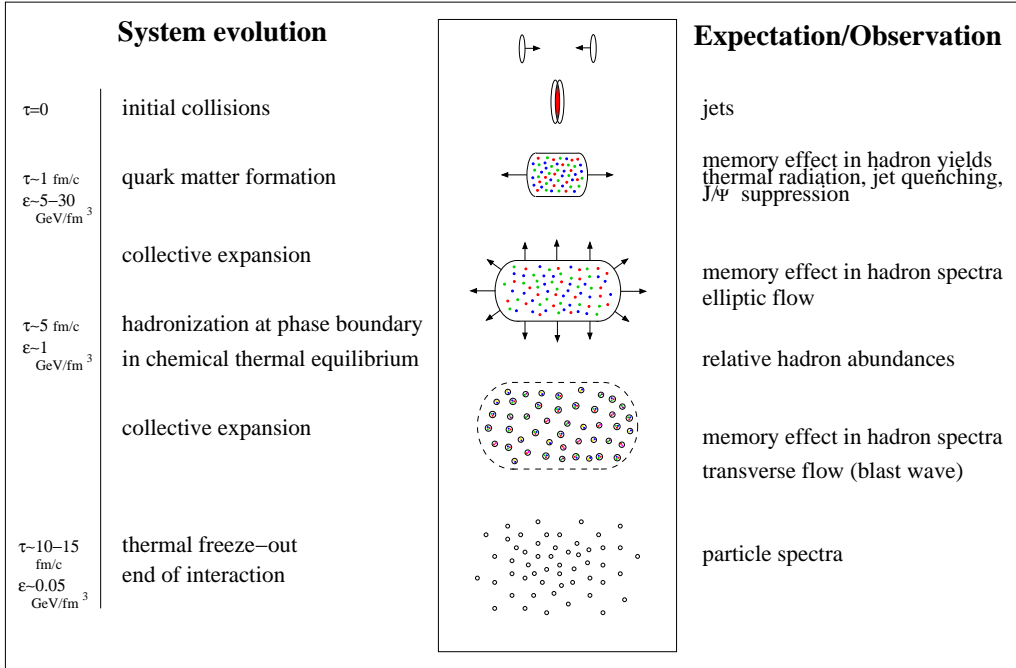


Figure 1.11: Schematic overview of the collision evolution at RHIC. Figure from ref. [21].

up and the hadron gas expands rapidly and cools. After an additional $\sim 6 - 10$ fm/c the hadrons stop interacting, first inelastically and then elastically, and the chemical and kinetic freezeout points are reached.⁹ The particle spectra at the kinetic freeze out indicates local thermal equilibrium and a large radial expansion velocity. This picture of the collision evolution is supported by the measurements presented in the sections 1.3. See also further discussion of figure 1.11 in ref. [27].

1.3 Selected results from RHIC

In the following, some of the main results from the RHIC experiments will be presented, with an emphasis on BRAHMS results. The text will roughly follow the time-line of the collision, starting with the charged particle multiplicity of the final state and then going back in time, from the shape of the particle spectra (linked to the kinetic freeze out) to measurements related to the initial conditions of the collision. The focus here will be on the bulk matter production in Au+Au collisions, since that is what is most important for comparison to the results to be shown in chapter 5. The results quoted in the following are for central Au + Au collisions at $\sqrt{s_{NN}} = 200$ GeV, unless differently stated.

For the experiments' own full, recent reviews of their data, including their views on the issue of QGP at RHIC, see refs. [28, 29, 30, 31].¹⁰

⁹It is at present not clear whether there are two distinct freezeout temperatures, or if they both occur at once. Most literature assumes them to occur at separate times, chemical equilibrium naturally being reached before kinetic.

¹⁰In December 2005, the combined conclusions from these four publications were selected as the Top

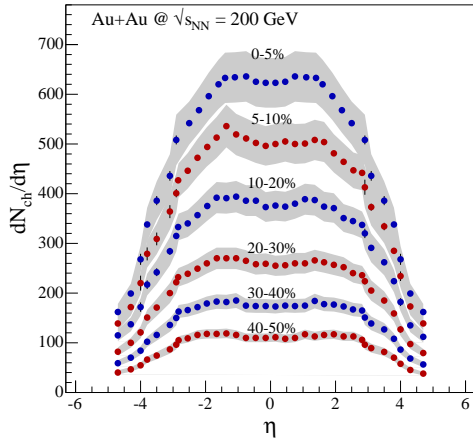


Figure 1.12: Pseudorapidity densities (multiplicities) of charged particles measured by BRAHMS for $\sqrt{s_{NN}} = 200 \text{ GeV}$ Au+Au collisions for various centralities. In 0 – 5% central events, we observe a total charged particle multiplicity of about 4600 [32]. Figure from ref. [30].

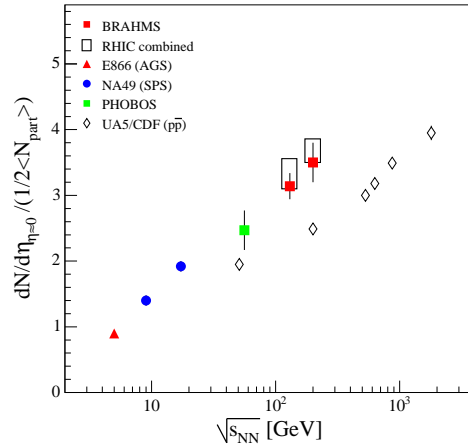


Figure 1.13: Multiplicity of charged particles per participant pair around midrapidity, as a function of $\sqrt{s_{NN}}$. The figure shows that the particle production in Au+Au collisions at the RHIC top energy, around $\eta = 0$, exceeds that seen in p+p collisions by 40-50%. Figure from ref. [30].

Charged particle production

The number of charged particles produced gives the first rough picture of an A+A collision, and it has ruled out a number of models proposed for the RHIC energy regime. Discussed in a number of early publications from the RHIC experiments (see e.g. [33, 34, 32, 35, 36, 37]), it has been related both to the interplay of soft and hard processes (see sec. 2.1), and to the concepts of parton saturation and nuclear shadowing. See figure 1.13 for an example of multiplicity distributions from Au + Au collisions at $\sqrt{s} = 200 \text{ GeV}$.

Figure 1.13 shows the multiplicity of charged particles per participant pair around midrapidity, as a function of $\sqrt{s_{NN}}$. For central collisions scaled by the number of participating nucleons, this number still exceeds that from $p + p$ collisions at the same energy by 40-50%. This result will be extended to cover identified particles in chapter 5.

The next step is to study the final composition of identified charged hadrons, preferably as a function of rapidity. At RHIC only BRAHMS is capable of doing this beyond $|y| \approx 0.5$, and the resulting measurement from central Au+Au collisions is shown in figure 1.14. We note a meson and antiproton production that follows the shape of the distribution of all charged hadrons¹¹, while the proton production is approximately constant out to the limit of the experimental acceptance. This is due to the presence of protons from the incident nuclei in the data sample.

Physics News Story of 2005 by the American Physical Society. See <http://www.aip.org/pnu/2005/split/757-1.html>

¹¹Note that the dip seen at $\eta = 0$ for charged hadrons disappears when you plot identified particles versus rapidity. This is a consequence of the η to y conversion.

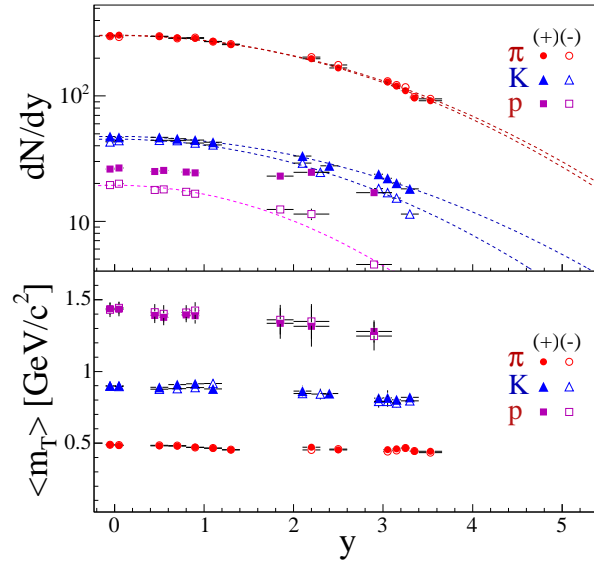


Figure 1.14: Top panel: Rapidity density distribution for positive and negative pions, kaons and protons in 0-5% central Au+Au collisions at $\sqrt{s} = 200$ GeV, as measured by BRAHMS. The shown data have not been corrected for feed down from weak decays. The lines show Gaussian fits to the measured distributions. Bottom panel: average m_T as a function of rapidity. From [30].

Soft spectra — thermal freeze-out

Figure 1.15, left panel, shows the identified particle production from central Au+Au collisions at midrapidity, as a function of transverse mass $m_T - m_0 = \sqrt{p_T^2 + m_0^2} - m_0$. The shape of such spectra in the low p_T region ($< 2 \text{ GeV}/c$) reflects the temperature and collective dynamics of the source of particles. According to statistical physics, the energies of particles emitted from a thermalized source will follow a distribution determined by the source temperature, and this has indeed been observed in $p + p$ collisions (see e.g. [39, 40]). In other words, normalized particle m_T spectra of different species should be describable by the same functional form. In A+A events it has been noted that the spectra from the different particle species exhibit a different behavior: the shape (and in particular, the steepness) of the spectra has a strong dependence on the particle mass. This can be interpreted using the so-called blast wave models [41]. In these models, the collision zone is described as locally thermalized with a fast collective radial motion – the energy of the emitted particles is partly thermal energy and partly translational kinetic energy from the blast. The blast originates from the pressure built up by the frequent scattering in the original dense system, combined with any density gradients set up by the collision geometry.

The shape of particle spectra is modeled by integrating the partial differential equations of hydrodynamics over the reaction zone by assuming certain thermal and velocity profiles. The resulting functions are normally used to fit spectra of several different particle species simultaneously, which gives a temperature T_k and a flow velocity $\langle \beta \rangle$ at the

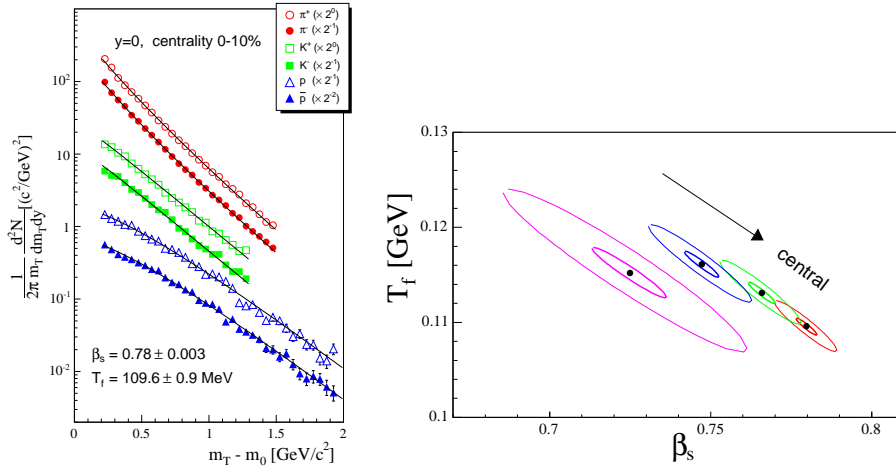


Figure 1.15: Left panel: Particle spectra from 0-10% central Au+Au at $\sqrt{s} = 200$ GeV, at $y = 0$. BRAHMS data from [38]. Lines are blast wave fits (see text). Right panel: Best-fit contours from blast wave analysis. The curves correspond to increasing centrality as β_s increases. Contours indicate 1σ and 3σ levels from the fits.

kinetic freeze out. The agreement between the blast wave fits and the soft particle spectra is remarkable and holds over a large energy span. In central collisions $T_k \approx 100$ MeV and $\langle\beta\rangle \approx 0.7c$ are extracted from such analyses [42, 38]. Figure 1.15 shows best fits (points), 1σ and 3σ contour lines from the fits shown overlain with the data in the left panel. There is a clear evolution with increasing centrality, with a rise of the flow velocity accompanied by a decrease in T_k .

Particle ratios — chemical freeze-out

The relative abundances of different particles are well reproduced by statistical thermal models. These models (see sec. 2.4 and e.g. [44, 45]) describe the source as a hadron gas in thermal equilibrium. Bose–Einstein and Fermi statistics, combined with conservation laws, predict the relative yields of the different particles. The only free parameters are the chemical freeze out temperature T_{ch} and the baryo-chemical potential μ_b . The interpretation of the fits to the data made from such models is not straight forward, however, since the model predicts the total (4π) yield from the grand-canonical ensemble, while the bulk of available A+A data are from a narrow region around mid-rapidity. Assuming that there is an independent, locally thermalized source of particles at each rapidity and that redistribution of particles in the longitudinal direction is limited, the model is still meaningful. The statistical model has been applied to RHIC data in e.g. refs. [42, 46, 43]. It is found that the temperature at the chemical freeze out is ≈ 170 MeV, while the baryochemical potential (at mid-rapidity) is ≈ 25 MeV – this is on the border of the phase transition to the quark gluon plasma as predicted by lattice QCD calculations (see also figure 1.7).

Figure 1.16 from [43] shows like-particle ratios (K^-/K^+ and \bar{p}/p) from Au+Au collisions at RHIC, together with data from lower energies. The observed correlation over three units of rapidity is reproduced by a thermal model [45] assuming a temperature

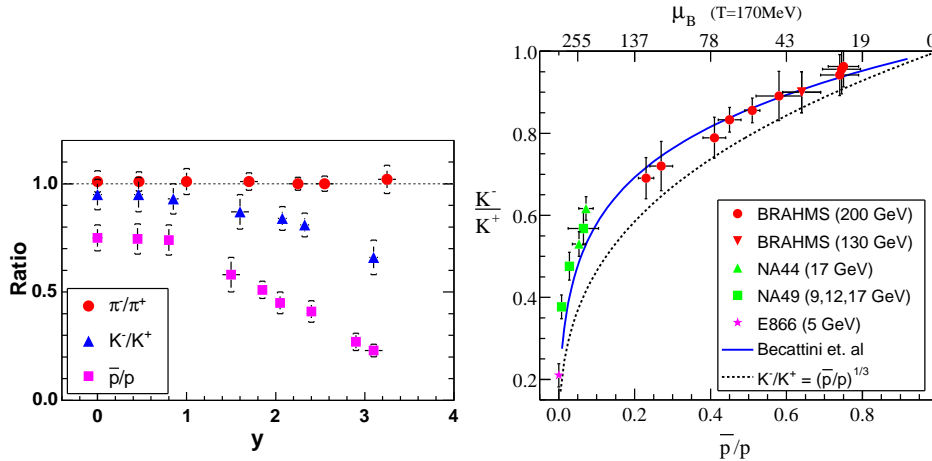


Figure 1.16: Left panel: Like-particle charged hadron ratios from central Au+Au collisions at $\sqrt{s} = 200$ GeV, as a function of rapidity. Right panel: Correlation of K^-/K^+ and \bar{p}/p ratios for different rapidities, compared with lower energy data and model calculations. See text for details. Plots are from [43].

of 170 MeV, a rapidity dependent μ_B and a finite (i.e. non-vanishing) value of the strange quark chemical potential μ_s . In chapter 5, this analysis will be extended to include like-particle ratios in $p + p$ collisions at $\sqrt{s} = 200$ GeV.

High- p_T suppression

One of the most striking results from RHIC so far is the observed deficit of particles with large transverse momenta, when compared with N_{coll} number of $p + p$ collisions. See figure 1.17, and e.g. references [47, 48, 49, 50].

The production of high- p_T particles is studied through the *nuclear modification factor* R_{AA} , defined as

$$R_{AA} = \frac{d^2N^{AA}/dp_T d\eta}{\langle N_{coll} \rangle d^2N^{NN}/dp_T d\eta}. \quad (1.1)$$

where the numerator is the production of charged hadrons in A+A collisions at a given p_T and pseudorapidity η , the denominator is the same for $p + p$ collisions and $\langle N_{coll} \rangle$ is the average number of binary collisions for the centrality class studied. If an A+A collision behaves just like a superposition of $p + p$ collisions, i.e. there is no effect of the nuclear medium, this ratio will be unity for all p_T .

At lower energies, it was observed in 1975 [51] that one sees an enhancement of this factor at moderate transverse momenta, both in $p+A$ and A+A collisions. This is known as the Cronin effect, and has been interpreted as a broadening of the incoming k_T distributions due to soft scattering of partons in the initial state. For RHIC, it was predicted (see e.g. [52]) that the high parton densities would lead to heavy energy loss from gluon bremsstrahlung, and consequently, if this effect was strong enough, one might rather see a suppression of high- p_T particles.

This was indeed observed, as shown in figure 1.17. Here, BRAHMS show a suppression in central Au+Au collisions at midrapidity (top left panel), and also at $\eta = 2.2$ (top right). For peripheral collisions (middle row) this suppression is not seen, indicating

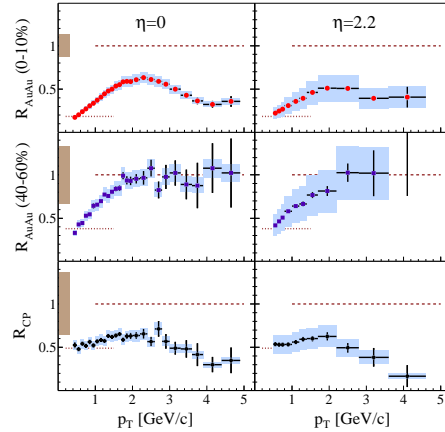


Figure 1.17: Nuclear modification factors for charged hadrons in Au+Au at $\sqrt{s} = 200$ GeV from BRAHMS. [47]

that some hot and dense medium is indeed produced in central collisions at RHIC. Also plotted (bottom row) is the ratio of central to peripheral events, scaled by the relevant $\langle N_{coll} \rangle$ for the two centrality classes, to exclude any systematic effects from the $p + p$ reference spectrum used. At that time this reference was based on extrapolated data from other experiments, since BRAHMS $p + p$ spectra were not yet available.

Later, analysis of R_{AA} factors at RHIC have been extended to cover both the properties of single jets (see e.g. ref. [28]) and of identified particle spectra. The latter result is discussed and extended in chapter 5.

Elliptic flow — early thermalization

Collective radial motion, or flow, can be studied by investigating the azimuthal anisotropy of the emitted particles relative to the reaction plane. It is quantified by the harmonic Fourier coefficients v_n in the azimuthal distribution of particles relative to this plane:

$$\frac{d^3N}{p_T dp_T dy d\phi} = \frac{d^2N}{2\pi p_T dp_T dy} (1 + 2\sum_n v_n(y, p_T) \cos[n(\phi - \Psi_{RP})]) \quad (1.2)$$

Ψ_{RP} is the azimuthal angle of the reaction plane and ϕ is the azimuthal angle of a single particle (with respect to the laboratory frame). The first harmonic v_1 measures the (asymmetric) flow of particles in the direction of the impact parameter vector (toward one of the colliding nuclei) – it is called directed flow. In a symmetric collision, the directed flow is zero at mid-rapidity, since the particles do not prefer the direction of one of the nuclei to the other – the size of v_1 typically becomes larger at forward or backward rapidities.

The second harmonic v_2 describes the symmetric flow of particles both parallel and perpendicular to the impact parameter vector. A large v_2 is caused by an elliptic shape of the source and is therefore called the elliptic flow. Data from RHIC exhibit a large elliptic flow, consistent with predictions from hydrodynamics. Figure 1.18 shows measurements from STAR of the elliptic flow for identified particles as a function of p_T [28]. In ref. [53]

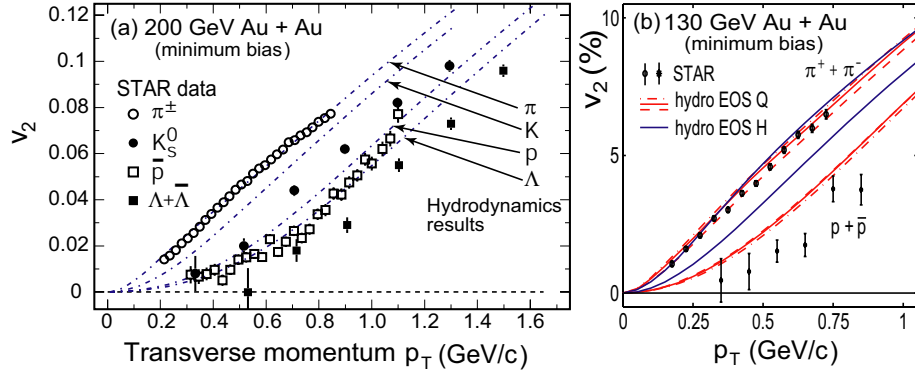


Figure 1.18: v_2 from STAR. Plot from [28].

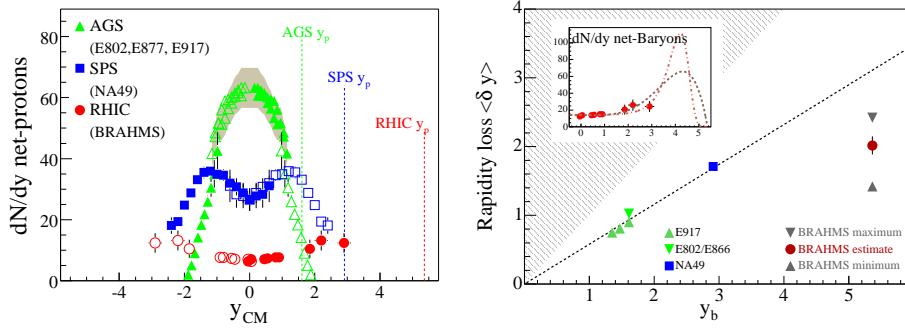


Figure 1.19: Stopping in A+A collisions vs. energy. Data from [54].

Kolb and Heinz conclude from the RHIC data: "The data on elliptic flow can only be understood if thermalization of the early partonic system takes less than about 1 fm/c. At this early time, the energy density in the reaction zone is about an order of magnitude larger than the critical value for quark deconfinement, leading to the conclusion that a well-developed, thermalized quark-gluon plasma is created in these collisions which, according to hydrodynamics, lives for about 5 – 7 fm/c before is hadronizes."

Baryon stopping

As discussed above, the kinetic energy that is removed from the beam and which is available for the production of a state such as the QGP depends on the amount of stopping between the colliding ions.

The stopping can be estimated from the rapidity loss experienced by the baryons in the colliding nuclei. If incoming beam baryons have rapidity y_b relative to the CM (which has $y = 0$) and average rapidity

$$\langle y \rangle = \int_0^{y_b} y \frac{dN_B}{dy} dy / \int_0^{y_b} \frac{dN_B}{dy} dy \quad (1.3)$$

after the collision, the average rapidity loss is $\delta y = y_b - \langle y \rangle$ [55]. Here dN_B/dy denotes the number of net-baryons (number of baryons minus number of antibaryons) per unit of rapidity. Thus, for the case of full stopping: $\delta y = y_b$.

Figure 1.19, left panel, shows the evolution of the net-baryon distribution in A+A collisions from AGS energies up to RHIC [54]. There is a clear evolution from a full stopping scenario at $\sqrt{s_{NN}} = 5$ GeV, to an almost net-baryon free midrapidity region at $\sqrt{s_{NN}} = 200$ GeV. BRAHMS does not measure the expected fragmentation region peaks since they lie outside our acceptance at this energy, but we can still make estimates of the maximum and minimum amounts of stopping since we know the total amount of conserved baryon number. See the right panel of figure 1.19. The most probable value for the stopping corresponds to an energy loss of 73 ± 6 GeV per nucleon, or a total of 26 TeV deposited in the fireball [30].

The exact nature of the processes responsible for transport of baryon number away from beam rapidity is however not well known. Several scenarios exist (see e.g. [56, 57, 58]), but a consistent picture has not yet been developed. Chapter 2 gives more details. In chapter 5 and appendix C the above discussion is extended to cover $p + p$ collisions at $\sqrt{s} = 200$ GeV, with comparisons to the data presented here.

Initial energy density

If we assume a hydrodynamical expansion of the fireball, entropy will be preserved throughout this stage of the collision. Therefore, the entropy at thermalization is the same at freeze-out, when no more interactions between particles occur. If the initial entropy can be calculated, the final multiplicities can be predicted. The initial energy density ε can be deduced from the measured multiplicities dN/dy :

$$\varepsilon_{Bj} = \frac{\langle E \rangle}{V} = \frac{\langle m_T \rangle \cosh y \frac{dN}{dy} \Delta y}{\pi R^2 \tau_0 \cosh y \Delta y} = \frac{\langle m_T \rangle}{\pi R^2 \tau_0} \frac{dN}{dy} \quad (1.4)$$

where τ_0 is the initial formation time, usually taken to be the thermalization time-scale 1 fm/c as a conservative upper limit (see e.g. [59] for a realistic estimate), and πR^2 is the transverse area of the collision zone. The relation $z = \tau_0 \gamma \beta = \tau_0 \sinh(y)$ has been used to calculate the length of the interacting volume: $\Delta z = \tau_0 \cosh(y) \Delta y$. This estimate is known as the Bjorken energy density [25].

In central Au+Au collisions ($R \approx 6$ fm) at $\sqrt{s_{NN}} = 200$ GeV the mean transverse mass is found to be ≈ 0.6 GeV and the rapidity density is ≈ 950 . Using the conservative estimate of $\tau_0 = 1$ fm/c, equation (1.4) gives $\varepsilon_{Bj} \approx 5$ GeV/fm³ [30]. This is 5 times higher than the critical energy density as determined from QCD lattice calculations [60], indicating that conditions are indeed fulfilled for the production of a QGP.

The initial state of a heavy ion interaction

Finally, interesting physics may be found even before the collision takes place, in the initial states of the colliding nuclei. Studies of deep inelastic scattering of leptons on protons and nuclei have revealed a large component of gluons with small- x (i.e. fraction of the nucleon momentum) that appears to diverge with decreasing x [61, 62, 63]. However, it has also been suggested that the density of gluons remains finite due to the increased role of gluon-gluon correlations ('gluon fusion'), forcing an upper limit on the total number of highly delocalized small- x gluons [64, 65]. Phenomenological descriptions of HERA $e + p$ and Fermilab results [66, 67] based on gluon saturation appear to successfully describe the data. Consequently, nuclei at high energies may be thought

of as highly correlated systems of small- x gluons. On the basis of this, a QCD based theory for dense small- x systems, termed the Color Glass Condensate (CGC) has been developed [68, 69].

Collisions between hadronic systems at $\sqrt{s} = 200$ GeV provide a window on the small- x gluon distributions of swiftly moving nuclei. In particular, collisions between deuterons and gold nuclei in which hadrons with $p_T > 1$ GeV/ c , mostly produced by quark-gluon interactions, are detected close to the deuteron beam direction, allow for probing the small- x components of the wave function of the gold nuclei. It has been predicted that gluon saturation effects will manifest themselves as a suppression in the transverse momentum distribution below a value that sets the scale of the effect [68, 69, 70]. The transverse momentum scale for the onset of gluon saturation depends on the gluon density and thus on the number of nucleons, and is connected with the rapidity y of measured particles by $Q_s^2 \sim A^{1/3} e^{\lambda y}$, where $\lambda \sim 0.2 - 0.3$ is obtained from fits to HERA data. Thus saturation effects are most evident at large y or pseudorapidity η , i.e. at small angles relative to the beam direction. At RHIC energies and at midrapidity the saturation scale for Au ions is expected to be ~ 2 GeV² [68, 69, 70].

Of the four RHIC experiments, this kinematic region is only accessible to BRAHMS. In the introduction to chapter 5 I will discuss the Color Glass Condensate hypothesis in a bit more detail, and results on charged hadron nuclear modification factors as a function of rapidity in d +Au collisions will be presented and discussed in the first and second paper.

Chapter 2

Proton–proton collisions

Heavy ion physics aims to understand the physics of extended hadronic matter under extreme conditions, by colliding heavy nuclei composed of protons and neutrons. As seen in the previous chapter, such experiments yield a rich variety of interesting data and phenomena, but the real challenge lies in interpreting and understanding these results.

At the present time there is however no fundamental theory that describes even the most elementary hadronic interaction, the proton–proton (or $p - \bar{p}$) collision, in a satisfactory way. This system shows vastly different characteristics at varying incident energies and kinematic regions (see sec. 2.5), and is therefore very interesting to study in itself. For heavy ion collisions such interactions are also frequently used as a baseline measurement to search for effects of a nuclear medium (as with the nuclear modification factors in sec. 1.3). It is therefore vital to the experimental study of the strong nuclear force that the properties of this system are measured and understood over a wide range of energies.

This chapter contains a brief discussion of theoretical modeling of a $p + p$ collision, with focus on the string picture of hadronic interactions. The Monte Carlo event generators PYTHIA, PHOJET and HIJING/B are presented, and some predictions are shown. I review some of the available data on $p + (\bar{p})p$ interactions at different energies, and also touch on some other relevant topics such as baryon junctions and isospin conservation.

2.1 Theoretical description of a $p + p$ collision

A high–energy $p + p$ collision can be seen as an interaction between two bound systems of quarks and gluons. Each system has three valence quarks (uud) with quark quantum numbers conserved by the strong force, and carries one conserved unit of baryon number. In addition there will be a large number of gluons and sea quarks, as shown in figure 1.4.

The total interaction cross section of $p + (\bar{p})p$ reactions has been accurately measured over several orders of magnitude in incident energy. See figure 2.9 in section 2.5. The total cross section σ_{tot} can be sub–divided into a number of phenomenologically different terms:

$$\sigma_{tot} = \sigma_{el} + \sigma_{SD} + \sigma_{NSD} \quad (2.1)$$

where

- σ_{el} is the cross section for elastic processes, i.e. $p + p \rightarrow p + p$ where the target

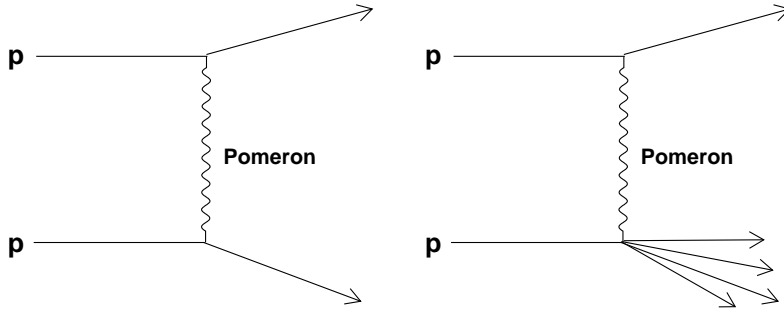


Figure 2.1: Diagrams for elastic (left) and single diffractive (right) scattering in a $p + p$ collision.

and projectile particle just scatter elastically through e.g. an electromagnetic interaction (or in the dual parton model discussed below, through the exchange of a single pomeron). See the left panel of figure 2.1.

- σ_{SD} stands for single diffractive processes, which proceed as an elastic scattering except that one incoming proton breaks up as a result of the pomeron exchange. See the right panel of figure 2.1.
- σ_{NSD} stands for non single diffractive processes, where both protons break up into several particles. This term collects both double diffractive processes and all more complicated hard and soft interactions that lead to multi particle final states on both sides.

As shown in figure 2.9 on page 35, at RHIC energies ($\sqrt{s} = 200$ GeV) the non-elastic processes completely dominate. Also, as will be discussed in chapter 3, BRAHMS is not equipped to measure elastic or single diffractive processes. I will therefore in the following focus on non single diffractive interactions.

An interplay of soft and hard processes

How do we model a non single diffractive $p + p$ interaction? First of all we note that at $\sqrt{s} = 200$ GeV we can expect interactions with a large transfer of four-momentum Q^2 , where the strong coupling constant α_s becomes small (see section 1.1). Such *hard processes* should be describable by perturbative QCD (pQCD), and indeed it has been shown that for $Q^2 > 2$ GeV leading-order pQCD reproduces experimental results quite well. For $Q^2 > 1$ GeV next-to-leading-order pQCD can be used. See e.g. refs. [71, 72] for recent comparisons of pQCD calculations to experimental results.

However, even at RHIC energies, most processes in a $p + p$ collision have a lower momentum transfer than this. See figure 2.14 on page 38, which shows particle production at midrapidity as a function of transverse momentum for several energies. The bulk of produced particles lies in the p_T region below 1 GeV/c.

So to model a $p + p$ collision at this energy, we need to split it into two parts. Hard processes can be calculated through straight pQCD, but for the soft part we need a phenomenological approach. One such method that is often used and quite mathematically

rigorous, is Regge theory [73, 74]. A phenomenological theory of the strong interaction at high energies, this approach employs a perturbative expansion in the parameters $1/N_c$ or $1/N_f$, i.e. the number of active colors c or flavors f , rather than in the strong coupling constant α_s . While this makes it possible to calculate particle production at lower energies than with pQCD, an inconvenient point of this approach is the large number of free parameters, i.e. the various cross sections, which have to be fixed by comparison to experiment. Subsequently, various QCD–motivated models based on quark–parton interactions have also been introduced.

2.2 The string model of hadronic interactions

Today, most detailed models of hadron–hadron interactions employ the so–called string picture on one or more levels. Developed first in the early 1980s (see e.g. [76]) on the foundations of the dual resonance model [77], such models assume that the strong, or colored, force field between two interacting hadrons can be approximated by a string with a certain tension κ , which can then break to form decay products. See figure 2.2. A nice, detailed review of the string model as well as various Monte Carlo implementations of it is given in ref. [78].¹ Only a short description will be given here, as a basis for the discussion of Monte Carlo models in section 2.4.

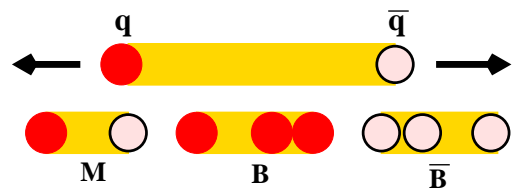


Figure 2.2: An excited string between a quark and an antiquark, which subsequently hadronizes into a meson (M), a baryon (B) and an antibaryon (\bar{B}) through creation of quark–antiquark pairs. Figure from [75].

The motivation for the string picture is the fact that the quark–antiquark attractive force appears increase linearly at large distances. This has been found both through the experimental study of the spectrum of quarkonium states, and from lattice QCD calculations. (See e.g. [1] and fig. 1.6 on page 8.) Such a force is reminiscent of a classical elastic string, $F(x) = -\kappa \cdot x$, where one parametrizes the attractive force as a function of the stretching x through a string tension κ . For the strong interaction, a string tension of about $\kappa_s=1$ GeV/fm is found.

In a hadronic interaction, one can form such strings between the target and the projectile. The strings stretch and store energy according to the momentum transfer Q^2 of the interaction, and in some models they can also have excitations in the form of ‘kinks’ in the transverse direction.

A schematic view of a $p + p$ interaction in the simplest version of the string picture is shown in figure 2.3. Two incoming protons, each containing three valence quarks, interact and two strings form between them. Each string has a quark at one end and a diquark, an association of two quarks, at the other. At this point two main classes of models exist. One forms the strings between the valence quarks of the initial protons (scenario (a) in fig. 2.3), and no exchange of quantum numbers occurs. This is known as longitudinal excitation, and models that use this mechanism are e.g. PYTHIA, HIJING, FRITIOF and UrQMD (see discussion of models in sec. 2.4). The other class, shown as scenario (b) in fig. 2.3, forms one string between a diquark from the projectile proton and

¹This is actually a long writeup of the physics behind the VENUS model, but the author also discusses other models at length.

a quark from the target, and one vice versa, i.e. there is a color exchange mechanism as part of the initial interaction. The models VENUS, DPM and PHOJET use this picture. The color exchange is treated as a soft process with almost no associated momentum transfer, so the main difference between the two model classes is that in the latter case the quark and diquark are in octet states to form a color singlet at each end, rather than in the original triplets. [75, 78]

After the strings are formed, they are allowed to decay to form hadrons. The mechanism for this is to let the string break at some point, forming a $q\bar{q}$ pair at the ends and assigning a new momentum, minus the mass of the newly formed quark pair, to the two new strings. This process then continues until all the excitation energy of the string is used up. There are several methods in use to determine just what quarks to produce and how to distribute their momenta [78], all of which lead to a distribution of on-shell hadrons with a certain y and p_T distribution. In some models, the produced particles are then allowed to rescatter. Finally, resonances and unstable particles are allowed to decay according to their known decay modes [79].

In addition to being a very fruitful model picture for hadronic interactions, the string model as a description of particle production is well established from $e^+e^- \rightarrow \gamma^* \rightarrow q\bar{q}$ reactions [76, 80]. It is used in modern models and still expanded upon, see e.g. [75] for a critical discussion of string formation in $p+p$ collisions in the framework of the neXus model [81].

2.3 Diquarks, junctions and fragmented physics

A large number of other concepts not explicitly treated by the simplest string models will also play a role in a complex event such as a $p+p$ collision. Some that will be touched upon later in this thesis are the leading baryon effect, diquark breaking, limiting fragmentation, baryon junctions and isospin conservation. All of these effects are treated in one way or another by the Monte Carlo models discussed in the next section, and will be briefly introduced below.

Leading baryons

The leading baryon effect is the observation [82] that in a high energy baryon-baryon interaction there tends to be among the reaction products a 'leading' particle, i.e. one that carries away a significant amount of the incident momentum. In terms of the so-called Feynman- x variable (denoted x_F , see app. A), the leading particle lies in the region $x_F \sim 0.2-0.8$. This effect has been observed for all types of final state baryons (p , n , Λ , Σ etc.) and over several orders of magnitude in incident energy, and is thought to arise because the target and projectile tend to split in a quark and a diquark connected by an excited color string. The average amount of momentum carried by this quark-diquark

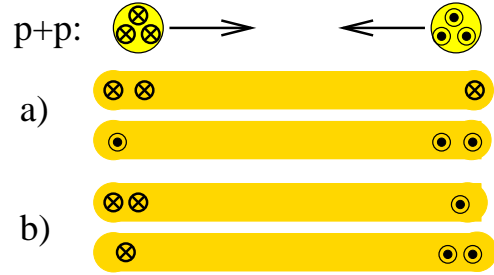


Figure 2.3: Two string formation mechanisms for a $p+p$ collisions: a) Longitudinal excitation. b) Color exchange. Figure from [75].

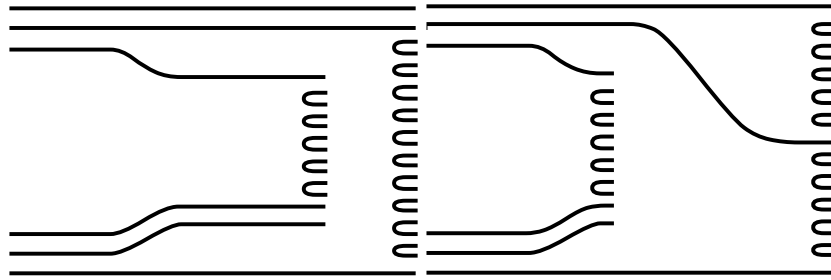


Fig. 1

Fig. 2

Figure 2.4: Two diagrams for nucleon–nucleon interactions in Regge theory. Left: Diquark conserving term. Note that both incoming nuclei are split into a quark and a diquark. Right: Diquark breaking term, where the topmost nucleon is split into three quarks through the exchange of another pomeron. Figures from [57].

pair, relative to the amount of energy stored in the string, will depend on the degree of stopping, but will in general be quite large. The diquark then picks up a quark from the fragmenting string, and a high momentum baryon has been produced. This also conserves the incoming baryon number.

Limiting fragmentation

Related to the leading baryon effect is the concept of limiting fragmentation [83], which has been observed both for hadron–hadron [84] and nucleus–nucleus interactions [32, 85, 86] over a wide range of energies. This hypothesis states that the excitation of the leading protons saturates at a moderate energy, leaving more available kinetic energy for particle production below the beam rapidity. The effect of this is that there will be a universal behavior of particle production over a limited rapidity interval if we plot it as function of $y - y_b$, i.e. the particle rapidity minus the beam rapidity. In other words, the global features of the physics of the fragmentation region will be similar independent of the center–of–mass energy, dominated by the properties of the valence quarks, while the major differences will be seen at lower rapidities.²

Diquark breaking

In its simplest implementation, the string picture discussed above splits the target and projectile hadrons into a quark and a diquark, connected by an excited color string, as assumed by the leading baryon effect. However, this approach has historically underpredicted the degree of baryon number transport to the midrapidity region (see e.g. [87]). In other words, some additional mechanism is needed to move the baryon number away from the fragmentation regions. One such mechanism is the breakup of the initial diquark into two quarks, connected by another excited string, which then also hadronizes according to the string model assumptions. See figure 2.4 for a schematic from Regge

²This is one reason why most modern heavy ion experiments are designed with coverage at midrapidity only.

theory. Diquark breaking is discussed e.g. in [57, 88] for baryon–baryon interactions, and treated for nucleus–nucleus collisions at SPS energies in the framework of the Dual Parton Model in [89].

Baryon junctions

Another mechanism for baryon transport from the fragmentation regions to midrapidity is the baryon junction, originally discussed in [90] and ‘revived’ for SPS and RHIC energies by D. Kharzeev in [56]. In this approach, the incoming baryon number is traced by a topological Y–shaped junction of three gluons, each originally connected to a valence quark. In a highly excited baryonic state the strings connecting these valence quarks fragment via multiple $q\bar{q}$ into mesons, finally leaving three sea quarks around the junction. See figure 2.5. In this sense, the junction traces the incoming baryon number without it being bound to the original quarks. Being purely gluonic in nature, and not tied to the initial valence quarks, the baryon junction is more easily transported to the midrapidity region e.g. through multiple gluon–gluon interactions.

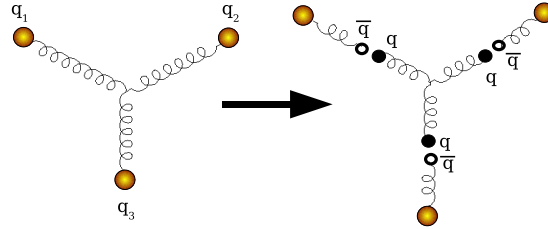


Figure 2.5: Schematic baryon junction. Left: A baryon with valence quarks q_1, q_2, q_3 bound by a junction. Right: All three strings are stretched and broken, forming three $q\bar{q}$ pairs, leaving a new baryon carrying the baryon number and three mesons carrying the original valence quarks.

Charge and isospin conservation

In a $p + p$ collision, not only is the conservation of baryon number important for the final state. We also have a net isospin and electromagnetic charge in the initial state which must be accounted for. In an A+A collision the multiplicity of final state hadrons is very large, and the redistribution of a few units of quantum number will not have a noticeable effect on the overall physics. For a $p + p$ interaction, however, where the multiplicity is relatively low (see e.g. section 2.5 and chapter 5), we may expect the fragmentation region physics to be affected by these constraints. As will be shown in chapter 5, at $\sqrt{s} = 200$ GeV we see a difference in the positive and negative pion production cross section at high rapidity that is consistent with this interpretation.

2.4 Monte Carlo and statistical modeling of $p + p$ events

Historically, particle production in relativistic hadronic collisions was early on described within the hydrodynamic approach [26], which treats the collision fireball as a liquid system that follows the relativistic Landau hydrodynamical equations. Then Regge theory [73, 74] was developed for soft interactions, and subsequently, various QCD–motivated models based on quark–parton interactions have also been introduced.

Currently, a vast variety of models for hadronic- and nuclear collisions exist. They may be subdivided into macroscopic (statistical and hydrodynamical) models [91, 92, 93], and microscopic (string-, transport-, cascade-, etc.) models, e.g. PYTHIA [94], PHOJET [95], UrQMD [96], QGSM [97], HIJING [22] and its extension HIJING/B [98], and several others (see e.g. [99, 100, 101]). In the hydrodynamical (thermal) model one assumes local (global) equilibrium, while the dynamics are characterized by the equation of state employed. The microscopic models instead try to follow the evolution of the individual interacting partons and treat all their interactions separately. A full discussion of all these approaches is beyond the scope of this text, but the ones that are employed further in the papers in chapter 5 will be treated in more detail below.

PYTHIA

PYTHIA [94] is a model of hadronic and lepton–hadron interactions commonly used at RHIC energies and above. It contains “theory and models for a number of physics aspects, including hard and soft interactions, parton distributions, initial and final state parton showers, multiple interactions, fragmentation and decay”³ PYTHIA is mainly a pQCD model, meaning that it contains a rigorous treatment of hard scatterings using perturbation theory, according to the parton model. It also includes both initial and final state radiation, where a virtual parton with a squared mass Q^2 can radiate a parton leaving a remainder parton with reduced Q^2 .

As noted above, for $p + p$ collisions one needs a phenomenological approach to soft interactions in addition to the hard scatterings. PYTHIA solves this by using pQCD for all interactions, but by ‘eikonalizing’ the cross section and using special methods to treat the divergent low- p_T parts.⁴ For a given impact parameter b , PYTHIA performs multiple parton scatterings according to a Poissonian distribution, with the average number of scatterings being b -dependent according to a profile function $A(b)$.

Two (main) ways of dealing with the low- p_T divergences within these multiple scatterings are implemented. One, known as the ‘simple’ scenario, is to simply introduce a cut-off parameter p_T^{cut} , such that $d\sigma/dp_T = 0$ for $p_T < p_T^{cut}$. This is the default scenario, with $p_T^{cut} = 1.9$ GeV/c. Another way, the so-called ‘complex scenario’, is to correct all divergent terms by a factor $p_T^4/(p_T^2 + p_{T0}^2)$ and replace p_T^2 by $p_T^2 + p_{T0}^2$ in determining α_s . p_{T0} is here a cut-off parameter as in the first scenario, but the cut-off is continuous rather than abrupt. The first of these scenarios is equivalent to introducing a maximum impact parameter b_{max} above which there are no interactions, while the second assumes some matter distribution around the edges of a hadron. A third option is to turn off multiple scatterings completely, leaving PYTHIA as a simple two-string model. This is described by the authors as a ‘toy model only’, pointing out the importance of this multiple scattering treatment in the model.⁵

After calculating the interactions and treating the initial and final state radiation, PYTHIA performs hadronization using the string picture as described in the previous

³According to the PYTHIA webpage, <http://www.thep.lu.se/~torbjorn/Pythia.html>

⁴Here, ‘eikonal’ is a word borrowed from Gribov–Regge theory, where one studies minijets by assuming that the Pomeron (see the next section) can be split into a soft and a hard component. In other words, the cross section for a given interaction can be split into two contributions, coming from soft and hard processes respectively. Also, p_T refers to the transverse component of the momentum transfer Q^2 .

⁵For reference, these processes are controlled in PYTHIA via the program parameter MSTP(82). See sec. 11.5 of the PYTHIA manual.

section. Programatically this is done using the code JETSET, now part of the PYTHIA package.

PYTHIA is a very flexible, well documented and tunable model. All aspects of the program are controllable by the user, and the manual (available in updated form at the project homepage) documents all options thoroughly. Amongst these options, it offers a parameter for tuning the probability for quark-diquark breakup discussed above. The value of this parameter can be used to better reproduce experimental results in $p + p$ collisions, especially for proton transport to midrapidity. Such a study is however beyond the scope of the present work. In chapter 5, comparisons to PYTHIA are done using the default parameters only, meaning also that the 'simple' scenario for multiple scatterings is used.

PHOJET

PHOJET is a Monte Carlo-based event generator much like PYTHIA, except that instead of pQCD it uses the Gribov-Regge phenomenology and calculations briefly discussed above. It is intended to be used for simulations of hadronic multi particle production at high energies in hadron-hadron, photon-hadron, and photon-photon interactions

(where hadron = proton, antiproton, neutron, or pion). The generator also includes photon flux simulation for photon-hadron and photon-photon processes in lepton-lepton, lepton-hadron, and A+A collisions.

The ideas and methods used in PHOJET are based mainly on the Dual Parton Model (DPM) [99]. The DPM is a partonic version of the dual resonance model [77], where the basic observation is that in hadronic interactions through the formation of intermediate states, i.e. resonances, the s -channel and t -channel amplitudes (see fig. 2.6) will be equal. This *duality* gives the model its name. The amplitude can be written down as a convergent sum of interactions with varying s known as the Veneziano amplitude, and this, combined with experimental high energy phenomenology, led to the description of such interactions through the exchange of a *pomeron* [102]. The pomeron is an effective particle with vacuum quantum numbers, in Regge theory identified with a trajectory with intercept $\alpha_0 = 1$ [1].⁶ The DPM extends the dual resonance models in the sense that it includes partons at the ends of the strings and interprets the hadrons in terms of the parton model.

Today the DPM represents an attempt to give an almost complete description of hadronic interactions at high energies. It combines results obtained within Regge theory and by perturbative as well as non-perturbative QCD expansions with generally accepted

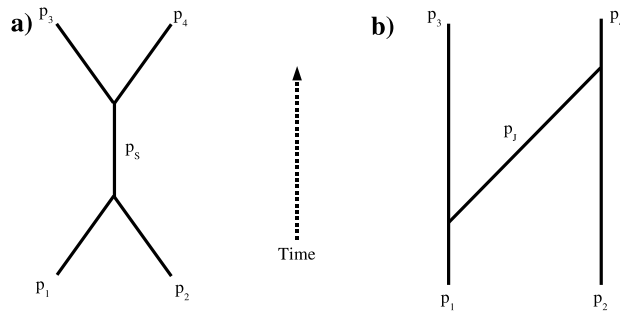


Figure 2.6: s -channel (a) and t -channel (b) scattering diagrams, through the exchange of a parton with momentum $p_s = p_1 + p_2$ and $p_t = p_1 - p_3$.

⁶Today, the pomeron is sometimes identified as a glueball. See e.g. [103].

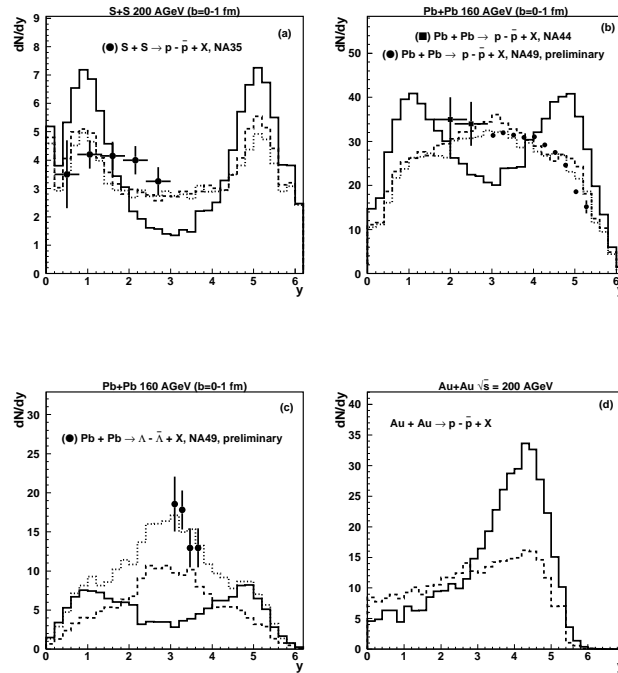


Figure 2.7: Predictions from the HIJING (solid), HIJING/B (dashed) and HIJING/B with 'ropes' (dotted) compared with experimental data from SPS. The upper two panels show net-proton distributions in A+A collisions, while the lower right panel shows predictions for Au+Au collisions at RHIC energies. Figure from [98].

arguments of unitarity and duality. Within this model one can calculate both elastic processes (i.e. cross sections) and inelastic processes (i.e. multi particle production) in a consistent way.

In order to combine the DPM treatment of soft processes with the predictive power of perturbative QCD, PHOJET is, like PYTHIA, formulated as a two-component model with cross sections split into a soft and a hard component. On the basis of the optical theorem, which relates the forward scattering amplitude in a reaction to the total cross section, Regge phenomenology is used to parametrize the total and elastic cross sections as well as a series of partial inelastic cross sections. To preserve unitarity, i.e. conservation of probability, PHOJET uses so-called 'multiple parton interactions' in one event, treating them through Gribov's Reggeon calculus. Since both soft and hard processes are treated in unified way, multiple soft and hard interactions may be generated in one event.

Hard scattering processes are simulated using lowest-order perturbative QCD. For the final fragmentation and hadronization of the parton configurations, the JETSET code is used, as for PYTHIA. Note that for baryon transport to midrapidity, diquark breaking is explicitly built into PHOJET through multiple Pomeron interaction diagrams.

Having a less phenomenological approach to soft physics than PYTHIA, PHOJET is a much used generator for $p + p$ physics studies at RHIC and LHC energies. PHOJET simulations of $p + p$ collisions at $\sqrt{s} = 200$ GeV, using default parameters, will be presented and compared with the present data in chapter 5.

HIJING/B

In 1994 the HIJING (Heavy Ion Jet INteraction Generator) Monte Carlo model [22] was presented by M. Gyulassy and X. N. Wang, putting special emphasis on the role of minijets in $p + p$, $p+A$ and $A+A$ reactions at ultrarelativistic energies. A minijet is the result of a hard scattering that is however not energetic enough to be identifiable as a jet by an experiment. The minijet production cross section was predicted to be high at RHIC energies (see e.g. [104] and references therein). HIJING takes input from the successful implementation of pQCD in PYTHIA, and also from low- p_T phenomenology used in the older FRITIOF model [105] (which is again based on PYTHIA), and in the Dual Parton Model. While its main use has been to describe $A+A$ collisions at RHIC, it also gives a reasonable description of a number of aspects of hadron–hadron interactions at ISR, RHIC and Tevatron energies (notably the energy and multiplicity dependence of charged particle rapidity and transverse momentum distributions). See ref. [106] for a thorough review.

Then in 1998, S. Vance together with the original authors incorporated a baryon junction mechanism into HIJING, re-releasing the model as HIJING/B [98, 58]. The aim was to better describe the high amount of baryon transport to midrapidity observed at SPS [87], and as shown in figure 2.7 this approach was able to reproduce several experimental observables — most notably the net-baryon distribution versus rapidity. In chapter 5, HIJING/B predictions will also be compared to the present data.⁷

Statistical models

Another framework in which to describe the abundances of hadrons produced in high energy hadronic interactions is that of statistical models (see e.g. [45, 108, 109] and references therein). This macroscopic approach assumes that the colliding system eventually evolves into a hadron gas state in equilibrium, i.e. governed by statistical laws.

Formally, the system is described through a grand canonical partition function⁸ which specifies the weight Z_i (sum of possible states) for each particle or resonance specie i in a multi-hadronic mixed gas at temperature T :

$$\ln Z_i = \frac{g_i V}{6\pi^2 T} \int_0^\infty \frac{k^4 dk}{E_i(k) \exp[(E_i(k) - \mu_i)/T] \pm 1} \quad (2.2)$$

where g_i is the statistical degeneracy factor of specie i , V the total common volume shared by all species, $E_i^2(k) = k^2 + m_i^2$ the total energy of specie i at momentum k , and $\mu_i = \mu_B B_i + \mu_S S_i + \mu_I I_i$, the chemical potential of specie i . In the last relation B denotes baryon number, S strangeness and I the isospin.

From Eq. 2.2, the distribution of number density of specie i , i.e. the multiplicity divided by volume V , and energy density ε_i can be derived as

$$n_i = \frac{g_i}{2\pi^2} \int_0^\infty \frac{k^2 dk}{\exp[(E_i(k) - \mu_i)/T] \pm 1} \quad (2.3)$$

$$\varepsilon_i = \frac{g_i}{2\pi^2} \int_0^\infty \frac{E_i(k) k^2 dk}{\exp[(E_i(k) - \mu_i)/T] \pm 1} \quad (2.4)$$

⁷A further extension, labeled HIJING/BB [107] also exists, but will not be discussed here.

⁸A microcanonical description of $p + p$ collisions is also being developed. See ref. [110].

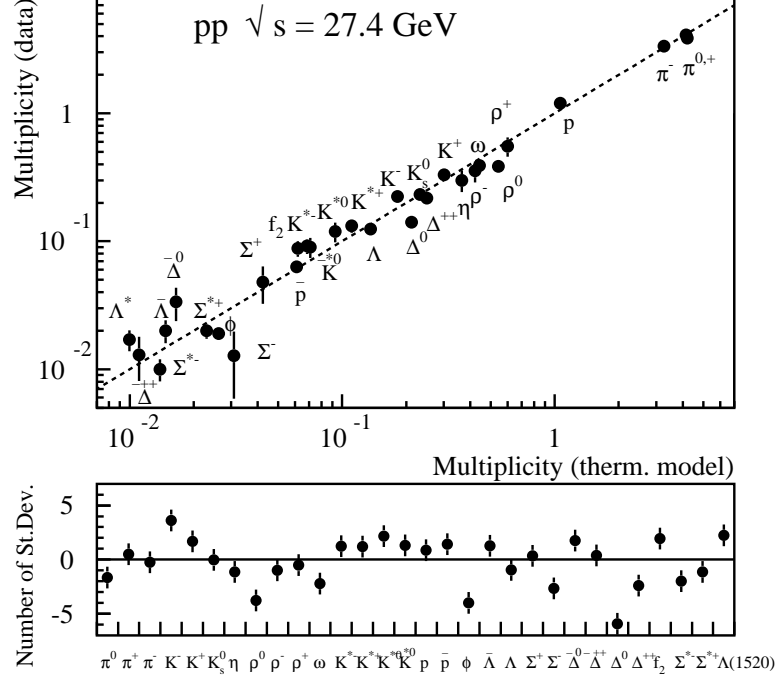


Figure 2.8: Statistical model description of particle multiplicities in $p + p$ collisions at $\sqrt{s_{NN}} = 27.4$ GeV. The lower panel shows the number of standard deviations of the individual data points from the thermal model fit. Figure from ref. [108].

where \pm distinguishes between bosons (-1) and fermions (+1). The total multiplicity of specie i in a collision is thus $N_i = n_i \times V$, and similar for the energy. Giving experimental measurements of multiplicities and particle ratios as input, the parameters of the model, T, V and $\mu_{B,S,I}$ can be determined.

Note that the three chemical potentials $\mu_{B,S,I}$ are not independent. From baryon, strangeness and isospin conservation, μ_S and μ_I can be expressed in terms of μ_B . Considering the quark chemical potentials μ_u, μ_d and μ_s of quarks u, d and s respectively, it follows that

$$\mu_u = \frac{\mu_B}{3} + \frac{2}{3}\mu_I \quad (2.5)$$

$$\mu_d = \frac{\mu_B}{3} - \frac{1}{3}\mu_I \quad (2.6)$$

$$\mu_s = \frac{\mu_B}{3} - \frac{1}{3}\mu_I - \mu_S \quad (2.7)$$

To find values for these parameters, T and μ_B are estimated first by investigating particle to antiparticle ratios. Using these results V can also be determined. For high temperatures, the Bose or Fermi statistics can be replaced by the Boltzmann statistics by dropping the ± 1 in the integral denominator of Eq. 2.3. The multiplicity ratio for particle

and antiparticle species i is then

$$\frac{N_i}{\bar{N}_i} = \frac{n_i V}{\bar{n}_i V} = \frac{n_i}{\bar{n}_i} \quad (2.8)$$

By using Eq. 2.3 in the Boltzmann approximation and noticing that statistics and phase-space are identical for particles and antiparticles, it follows that

$$\frac{N_i}{\bar{N}_i} = \exp \frac{\mu_i - \bar{\mu}_i}{T} = \exp \frac{2\mu_i}{T} \quad (2.9)$$

Statistical models have been successful in describing particle ratios and multiplicities in both A+A and $p + p$ collisions from SIS to RHIC energies ($\sqrt{s_{NN}} = 2$ GeV to $\sqrt{s_{NN}} = 200$ GeV). See figure 2.8, which shows a fit to SPS data from $p + p$ collisions at $\sqrt{s} = 27.4$ GeV. Even for such a small system the model shows a surprising ability to reproduce data, and it has been shown that it even reproduces features of e^+e^- interactions [111]. The reason for this success is not known. For fits to A+A data, see e.g. [112, 113].

From fits performed on data at all available energies, the phase diagram of nuclear matter can be drawn by correlating T and μ_B at the chemical freeze-out points. This is what was shown in figure 1.7 on page 9. In this thesis, some elements of the statistical model will be used for the discussion of particle ratio correlations over several units of rapidity, in the third paper of chapter 5.

2.5 Available data

This section reviews a small selection of the available data on particle production in $p + p$ and $p + \bar{p}$ collisions. Experiments have been performed at numerous laboratories over several orders of magnitude in center-of-mass energy. Figure 2.9 indicates the range of available measurements by plotting the total interaction cross sections for $p + p$ (upper panel) and $p + \bar{p}$ (lower panel) collisions versus \sqrt{s} . The data are collected by the Particle Data Group [79]. It is immediately clear that the cross sections have a highly non-trivial energy dependence, indicating that several relevant physics processes exist that dominate at different energies. It is also clear that as one goes above $\sqrt{s} \sim 10$ GeV the elastic cross section becomes low (<10%) compared to the inelastic cross section. In other words the probability for the particles to just scatter off each other without any more violent interaction is low. A third thing to notice is that as we reach $\sqrt{s} \sim 30-40$ GeV the inelastic $p + p$ and $p + \bar{p}$ cross sections become very similar, i.e. the annihilation cross section in $p + \bar{p}$ becomes negligible relative to other processes.

Unfortunately, not all the experiments whose cross section measurements are gathered in figure 2.9 have had full particle identification capabilities and those that do differ widely in their coverage of rapidities and transverse momenta. The data that are most relevant for comparisons with the dataset to be presented here, in order of increasing energy, come from the ISR and SPS at CERN, the other experiments at RHIC, and the Tevatron at Fermilab.

Data at lower energies

In ref. [114] is presented a compilation of all average charged particle multiplicities, up to and including ISR energies, available at that time. These results are replotted in

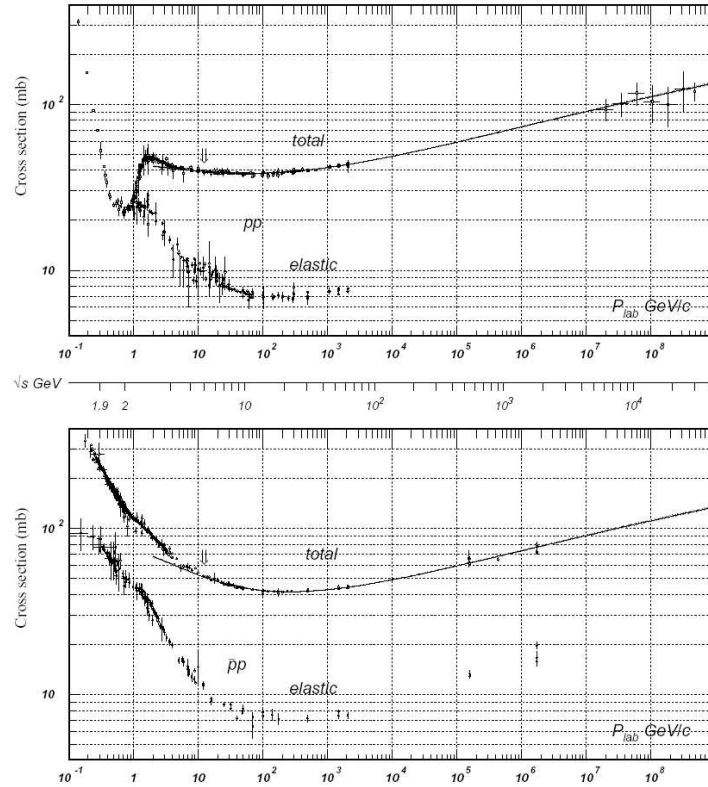


Figure 2.9: $p + p$ and $p + \bar{p}$ total and elastic cross sections, as a function of collision energy. Compilation of data by the PDG [79].

figure 2.10 as a function of \sqrt{s} .

The lines are phenomenological fits to the data, using the parameterizations

$$\langle n_i \rangle = A + B \cdot \ln(s) + C \cdot s^{-1/2} \quad (2.10)$$

$$\langle n_i \rangle = A + B \cdot \ln(s) + C \cdot s^{-1/2} \cdot \ln(s) \quad (2.11)$$

for mesons and baryons respectively. At high energies, it is expected from limiting fragmentation (or Feynman scaling) that the multiplicities increase as $\ln(s)$, while at lower collision energies power dependences s^α are expected [114]. These functional forms, sums of the high and low energy expectations, follow the data over the entire available range. Later, consistent measurements have also become available from SPS, notably from the NA27 [115] and NA49 [116, 117] collaborations. See the fourth paper in chapter 5 for a figure including their published pion multiplicities.

As an example of the rapidity dependence of charged particles from a $p + p$ collision, figure 2.11 shows pions and kaons at $\sqrt{s} = 17.3$ GeV from NA49. The pion data (upper panel) are well described by both a single and a double Gaussian in y , indicating that while there may be a central Bjorken plateau in the particle production it is not very pronounced at this energy.

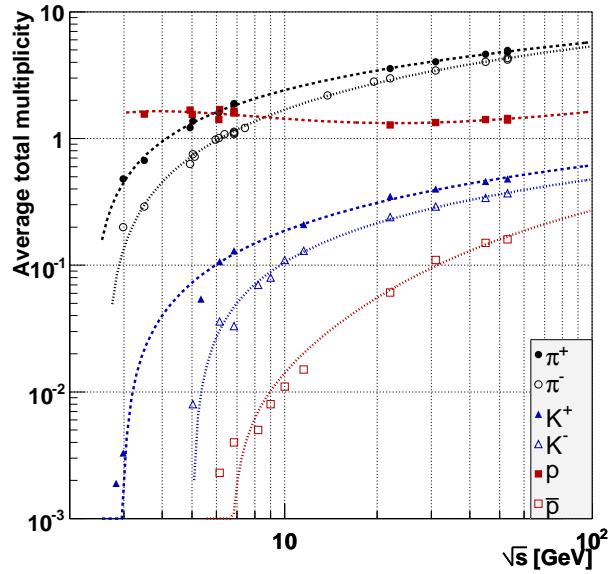


Figure 2.10: Average multiplicities up to ISR energies. Data from [114]. Fits have been re-done here.

RHIC data

At RHIC, all four experiments have recorded proton-proton collisions at $\sqrt{s} = 200$ GeV. While only BRAHMS has particle identification capabilities away from midrapidity, both the STAR and PHENIX collaborations have published various identified particle spectra at $y \sim 0$. Figure 2.12 shows identified charged particle spectra from $p + p$ and $d + \text{Au}$ collisions at $\sqrt{s} = 200$ GeV, averaged over the rapidity interval $-0.5 < y < 0$, as measured by STAR [118]. Further discussion of these midrapidity spectra can be found in the PhD dissertations of J. Ruan [119] (STAR) and E. F. Matathias [120] (PHENIX).

Figure 2.13 shows a midrapidity measurement of the invariant production vs. p_T of neutral pions from PHENIX [72]. The plot also shows two NLO pQCD calculations and the deviation of the data from these predictions. While π^0 production is not discussed further in this thesis, it is interesting to note that even at $\sqrt{s} = 200$ GeV NLO pQCD is capable of describing overall features such as this invariant p_T spectrum to a very high degree.

Comparison of charged hadron spectra at midrapidity

Finally, figure 2.14 shows a compilation (from ref. [31]) of unidentified charged hadron p_T spectra at midrapidity, from $\sqrt{s} = 53$ –1800 GeV. All spectra show a power-law dependence on transverse momentum, with the broadening at high p_T increasing with the incident energy. Note that the bulk of produced particles lie in the transverse momentum region below $p_T = 2$ GeV/c, indicating a strong contribution to the final spectra from soft processes.

In chapter 5 I will present a similar BRAHMS measurement at $\sqrt{s} = 200$ GeV. Comparisons with published data such as those in fig. 2.14 provide an important consistency check of the results.

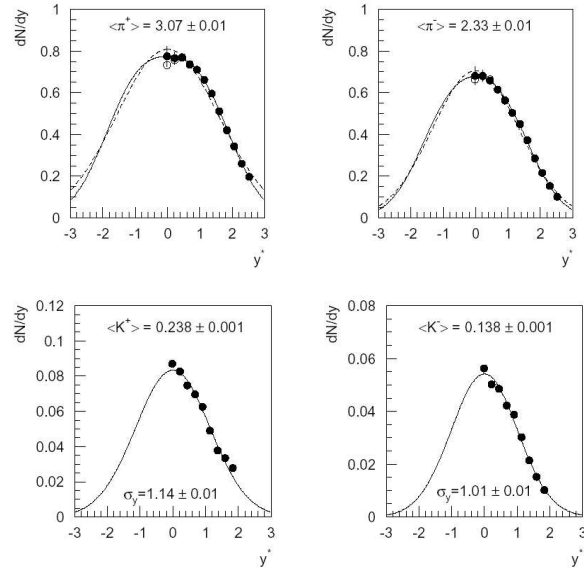


Figure 2.11: Meson production as a function of rapidity at $\sqrt{s} = 17.3$ GeV, as measured by the NA49 experiment at SPS. Plots from the thesis of C. Hoehne [117]. The pion data have recently been published in ref. [116].

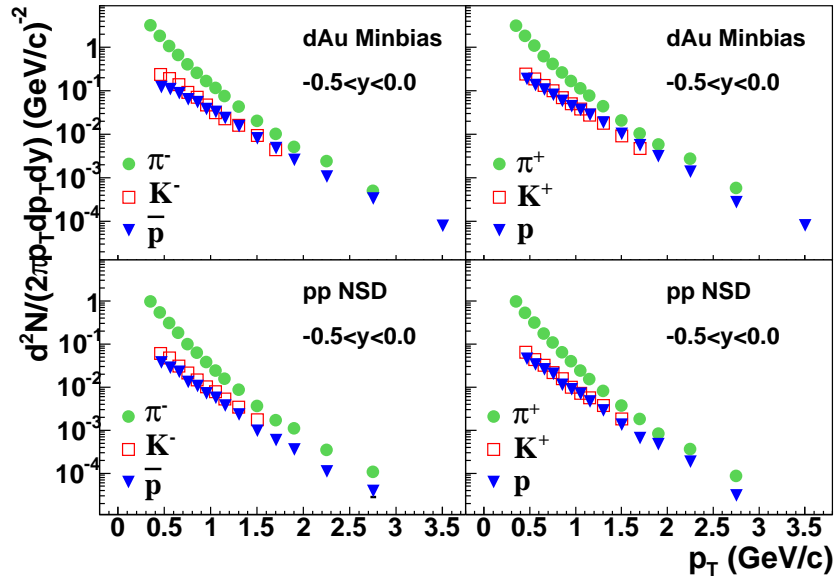


Figure 2.12: Identified charged particle spectra from $p + p$ and $d + \text{Au}$ collisions at $\sqrt{s} = 200$ GeV, averaged over the rapidity interval $-0.5 < y < 0.0$. Data from the STAR collaboration [118].

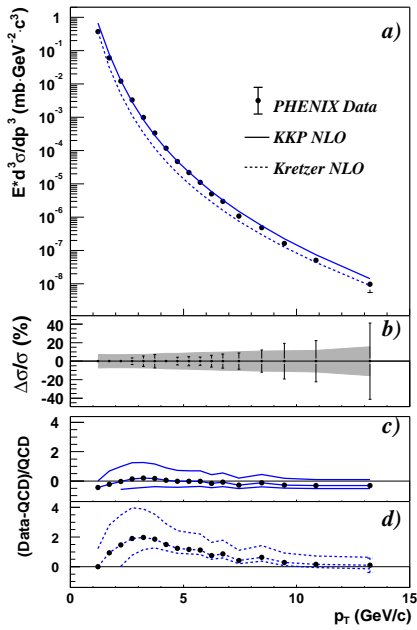


Figure 2.13: Neutral pion production in $p + p$ collisions at midrapidity, measured by the PHENIX collaboration. Data from ref. [72].

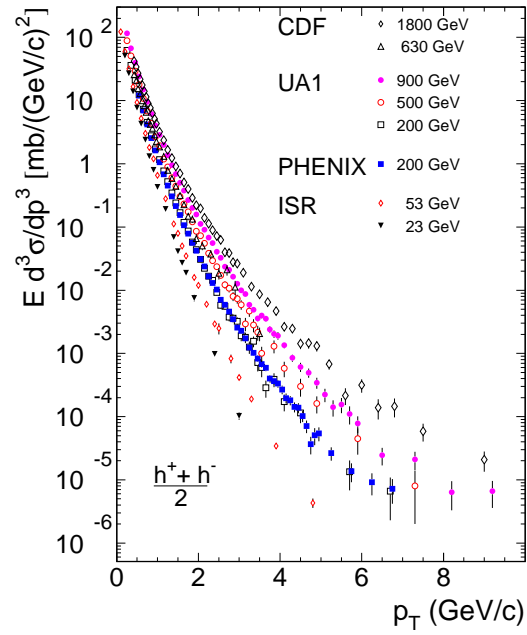


Figure 2.14: $(h^+ + h^-)/2$ at $y=0$ over two orders of magnitude in incident energy. Compilation from [31], see references therein for data.

Chapter 3

The BRAHMS experimental setup

The data presented in this thesis were collected with the BRAHMS experimental setup at RHIC accelerator, during its 2001–2002 and 2003 running periods. In the following sections I will briefly review the experiment as it was during this time. For a full, technical description of the BRAHMS detector, see ref. [121].

3.1 The Relativistic Heavy Ion Collider

RHIC, the Relativistic Heavy Ion Collider[122], is part of the accelerator complex at Brookhaven National Laboratory (BNL) in New York. It is at the present time the most powerful heavy ion colliding machine in operation, capable of colliding all nuclear species up to and including Au. The maximum center-of-mass energy available for Au+Au collisions is $\sqrt{s_{NN}} = 200$ GeV, while for $p + p$ collisions RHIC can theoretically reach $\sqrt{s} = 500$ GeV. As the time of writing, RHIC has only delivered collisions up to the maximum Au+Au energy, corresponding to a beam rapidity of

$$y_b^{200\text{GeV}} = 5.36 \quad (3.1)$$

Figure 3.1 shows a schematic view of the full BNL accelerator complex.

The design goal of RHIC is to collide heavy ions at ultrarelativistic energies to study the phase diagram of nuclear matter, and also to collide polarized protons to study their spin structure. Since starting operations in 2000 various species have been collided with high luminosities, providing good statistics for the participating experimental collaborations. See table 3.1 for a summary of RHIC runs during 2000–2005.

As a collider, RHIC consists of two separate accelerator rings which intersect at six points around the 3.8 km circumference. The ion beams are bunched to provide accurate collision timing and to reduce the width of the interaction region. Under normal

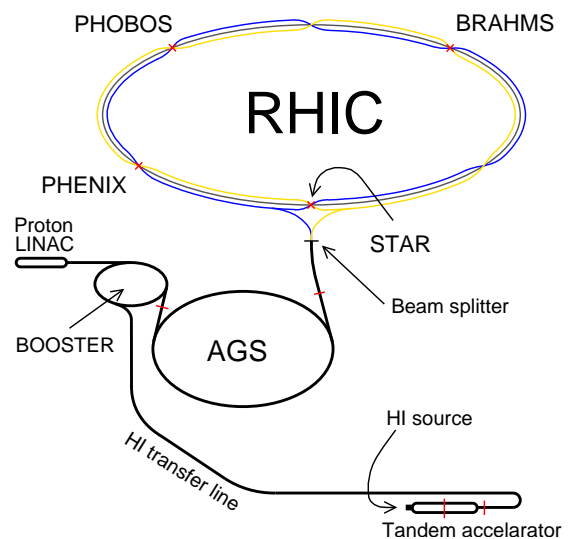


Figure 3.1: The RHIC accelerator complex. Figure from [21].

	System	$\sqrt{s_{NN}}$ [GeV]	Period
Run I	$Au + Au$	130	Summer 00
Run IIa	$Au + Au$	200	Fall 01
Run IIb	$p + p$	200	Fall 01
Run IIIa	$d + Au$	200	Winter 02/03
Run IIIb	$p + p$	200	Spring 03
Run IVa	$Au + Au$	200	Winter 03/04
Run IVb	$Au + Au$	62.4	Spring 04
Run IVb	$p + p$	200	Spring 04
Run Va	$Cu + Cu$	200	Winter 04/05
Run Vb	$Cu + Cu$	62.4	Spring 05
Run Vb	$p + p$	200	Spring 05

Table 3.1: The running periods at RHIC through 2005.

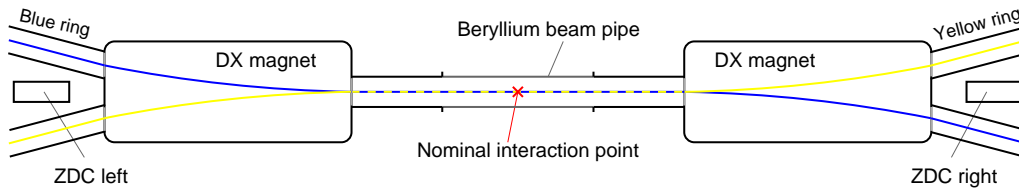


Figure 3.2: Schematic view of the RHIC interaction region. 'Yellow' and 'Blue' are the names of the two accelerator rings. Figure from [21].

Au+Au operations RHIC delivers 56 bunches of $\sim 10^9$ ions per beam, providing about 8 million bunch crossings per second. The RHIC design luminosity for Au+Au collisions at the maximum energy is $\mathcal{L} = 2 \cdot 10^{26} \text{cm}^{-2}\text{s}^{-1}$, giving a maximum reaction rate of $R = \mathcal{L} \cdot \sigma_{Au+Au} = 1400 \text{Hz}$ for the nominal hadronic cross section $\sigma_{Au+Au} = 7.2\text{b}$.

Four of the six interaction regions are used for experiments by the STAR [123], PHENIX [124], PHOBOS [125] and BRAHMS [121] collaborations. In addition an experiment dedicated to elastic polarized proton scattering, PP2PP [126], shared the BRAHMS experimental hall for the 2001 and 2003 $p + p$ runs.

The RHIC interaction region

In the interaction regions (IRs), two DX magnets steer the beams into a single beam pipe so that the nuclei collide at a small (but finite) angle. See figure 3.2 for a schematic. The transverse dimensions of the beams are typically 1 – 2 mm. The beam pipe between the DX magnets has a radius of 3.81 cm. Around the nominal interaction points ($\pm 0.75\text{m}$ in the BRAHMS IR) it is made of 1.2 mm thick beryllium in order to reduce secondary interactions. The width of the distribution of actual interaction points is determined by the bunch length and the crossing angle of the beams. The latter can be controlled to some degree, to maximize the relationship between luminosity and the desire for a narrow collision range.

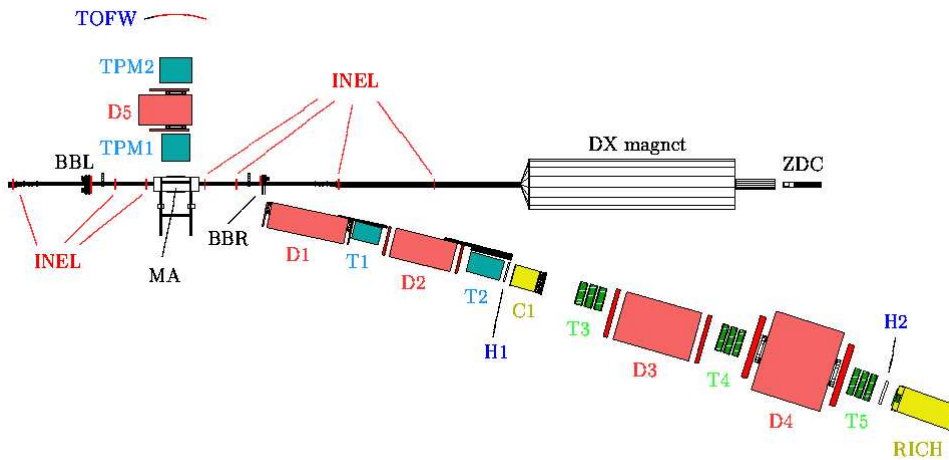


Figure 3.3: An overview of the BRAHMS detector setup for the 2001–2002 run.

3.2 BRAHMS detector overview

BRAHMS, or Broad RAnge Hadron Magnetic Spectrometer, is designed for precision measurements of charged hadron production over a wide range of rapidities and transverse momenta. Its strength at RHIC compared to the other experiments is its rapidity coverage, covering $0 < y < 4$ for pions, combined with excellent particle identification capabilities. Its drawbacks are the small solid angle coverage and limited event-by-event physics capabilities, meaning that only measurements of average properties of the final state are possible.

The experiment is run by the BRAHMS collaboration, consisting of approximately 50 physicists from 11 institutions.¹ So far BRAHMS has taken data during all RHIC running periods.

Measurements with BRAHMS

The BRAHMS detector is a two-arm magnetic spectrometer, combined with an array of global detectors for event characterization. See figure 3.3 for an overview. The two spectrometers can rotate in the floor plane to cover all angles from 90° to 2.3° with respect to the beam pipe.

Measuring the effects of an interaction with BRAHMS proceeds roughly as follows:

1. The global detectors provide triggering information, causing the event to be read out.
2. In each spectrometer, particles have deposited energy and can be tracked through separate time-projection chambers (TPCs) and drift chambers (DCs).
3. Momenta are determined by the particles' bending through several dipole magnets.
4. Timing information for individual particles have been recorded in several time-of-flight (TOF) systems, and hits are matched to the spectrometer tracks.

¹See appendix E for a full listing.

5. Tracking and time-of-flight information is supplemented by data from two Cherenkov detectors in the forward spectrometer for detailed particle identification over a wide range of momenta.

Combining the information from the above steps, stable charged hadrons can be uniquely identified over a wide area in rapidity and transverse momentum. Figure 3.4 shows the full acceptance of the spectrometer for identified particles when covering all accessible angles and magnetic field settings, as well as the coverage for some single settings. For pions, BRAHMS can measure identified particle production over four units of rapidity, i.e. to within 1.3 units of the beam rapidity.

The BRAHMS coordinate system

To discuss BRAHMS it is useful to first have defined the global coordinate system used. See figure 3.5 for an illustration, and additional discussion in appendix A.

The beam line is defined as the z axis, with positive z pointing in the direction of the forward spectrometer. The y coordinate is defined as the direction perpendicular to the axis of rotation of the spectrometer, i.e. the vertical direction, with positive y going upwards. x is then the direction perpendicular to the $y-z$ plane, with positive direction defined to make the coordinate system right-handed. The positive x axis runs through the midrapidity spectrometer when it is positioned at 90° .

Spectrometers and magnetic field settings

The two BRAHMS spectrometers rotate around a common axis, the vertical axis running through the origin of the global coordinate system. This origin, i.e. global $x = y = z = 0$, is known as the nominal interaction point (IP).

The **Midrapidity Spectrometer (MRS)** is a simple but flexible construction. It can rotate from 90° to 30° relative to the beam line, and is designed to be symmetric about a straight line drawn through the detectors from the IP. Outwards from the IP its main components are a TPC (TPM1) followed by a dipole magnet (D5) and a second TPC (TPM2) and finally a time-of-flight wall (TOFW). The symmetric design nominally gives equal acceptances for positively and negatively charged particles swept through the magnet. Also, the TPM1–D5–TPM2 complex can be moved back from the IP by up to 50 cm to reduce the track density for low-angle Au+Au runs.

For later runs, the MRS has been augmented by a Cherenkov detector and a second time-of-flight wall for extended particle identification, but these were not installed for the data sets presented in this thesis.

The **Forward Spectrometer (FS)** is actually two separate subsystems, known as the Front Forward Spectrometer (FFS) and the Back Forward Spectrometer (BFS). The FFS can rotate from 2.3° to 30° relative to the beam line, so that its range just overlaps with that of the MRS, while the BFS only covers from 2.3° to 15° . The FFS starts with a dipole magnet (D1) that sweeps particles away from the beamline, followed by a detector complex very like the MRS consisting of a TPC (T1), another magnet (D2), another TPC (T2) and a hodoscope (H1). In addition a threshold Cherenkov counter (C1) can be positioned after H1. Then follows the BFS, consisting of three drift chambers (T3, T4 and T5) interspaced by two magnets (D3 and D4), another hodoscope (H2) and finally a ring-imaging Cherenkov detector (RICH).

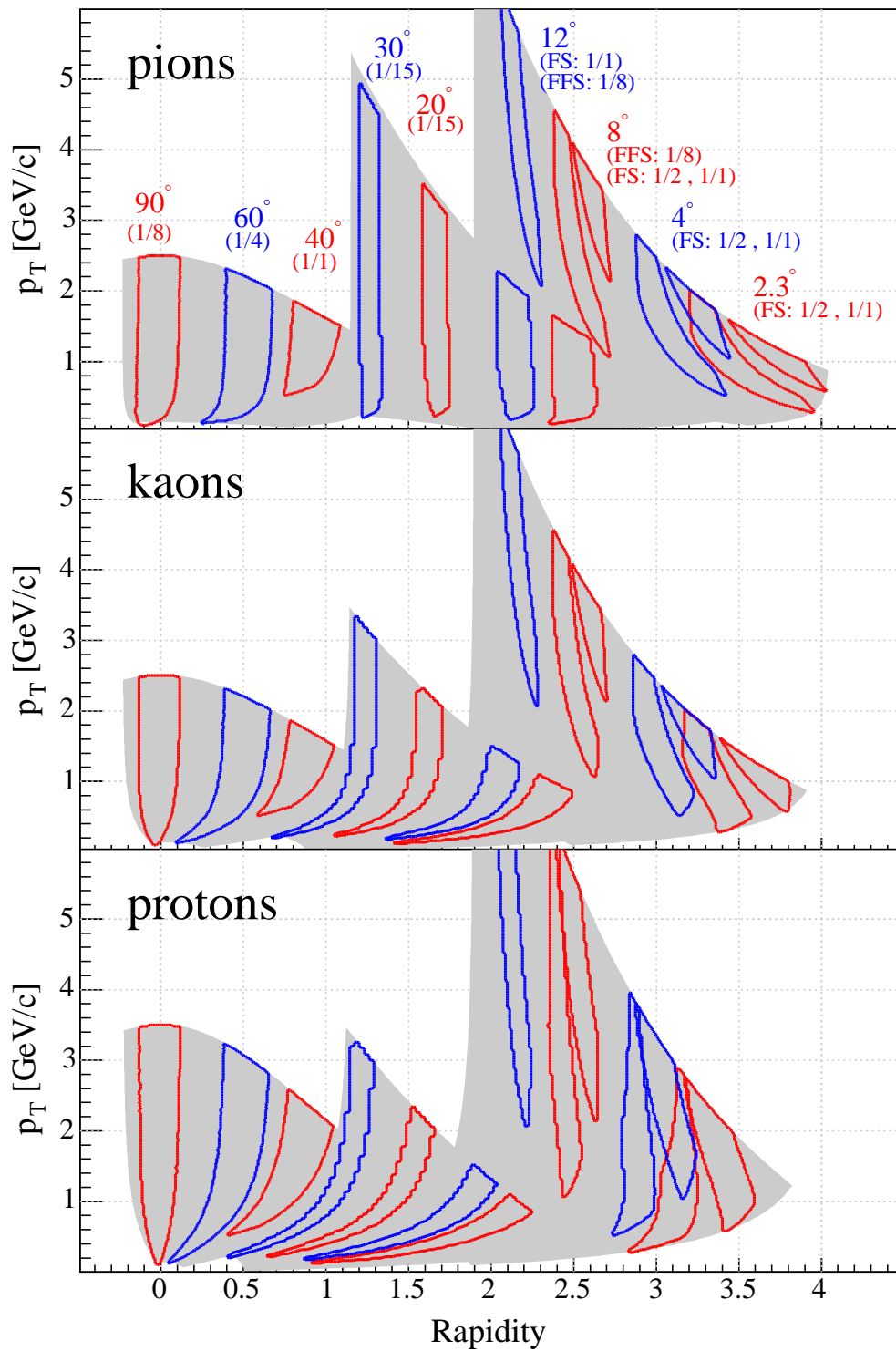


Figure 3.4: The full BRAHMS acceptance in $y - p_T$ for pions, kaons and protons. The gray region shows the area accessible to our PID systems, assuming design resolution, while the blue and red regions show the acceptances for example spectrometer settings. Figure from [21].

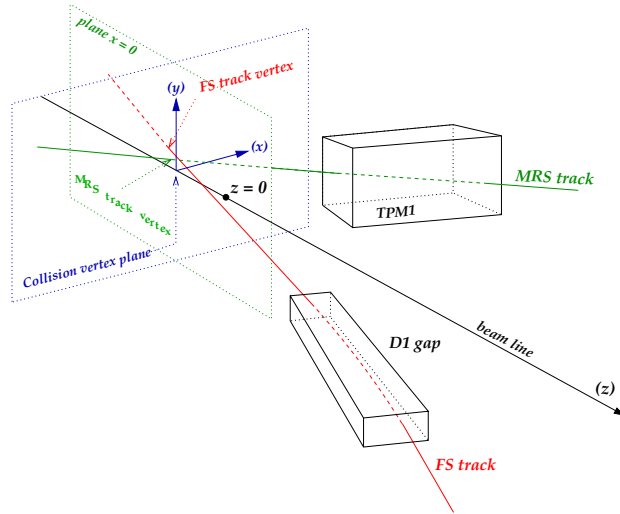


Figure 3.5: The BRAHMS coordinate system, relative to the beam line and the two spectrometers.

The detectors of the FS are placed on an arc bending away from the beamline, in such a way that with all the magnets at full field particles of momentum $p_{ref} = 22.5 \text{ GeV}/c$ will pass straight through the entire spectrometer. To select particles of lower momenta, fractional field settings are used. In addition, this setup will only select particles of one charge sign, so we must also change the polarity of the magnets to record both positive and negative particles.

Note that both spectrometers are positioned in the positive z hemisphere. For symmetric collisions like $p + p$ and Au+Au this has no effect, but for asymmetric systems like $d + \text{Au}$ it means that we will only measure one side of the interaction. For the 2003 $d + \text{Au}$ run, the orientation was such that BRAHMS saw the deuteron fragmentation side.

3.3 Global detectors

Event characterization and basic triggering information in BRAHMS is provided by a set of global detectors — the inelastic counters (INEL), a set of beam–beam counters (BB), a multiplicity array and two zero–degree neutron calorimeters (ZDCs).

INEL counters

The primary interaction trigger in $p + p$ collisions is provided by eight rings of plastic scintillator tiles, known as inelastic (INEL) counters, four on each side of the nominal interaction point. See fig. 3.6. The timing resolution of the INEL rings is 120 ps. The four rings are positioned at $z = \pm 75 \text{ cm}$, $\pm 115 \text{ cm}$, $\pm 416 \text{ cm}$ and $\pm 660 \text{ cm}$, and cover angles from 0.58° to 9.758° .

Simulations of the experimental setup using GEANT [127] show that for the 2001 setup these rings saw $71 \pm 5\%$ of the 41 mb $p + p$ total inelastic cross–section. In experimental $p + p$ data, we see an average of 7 hits in each of the two arrays per event. See sections 3.4 and 4.1 for more information on the trigger systems.

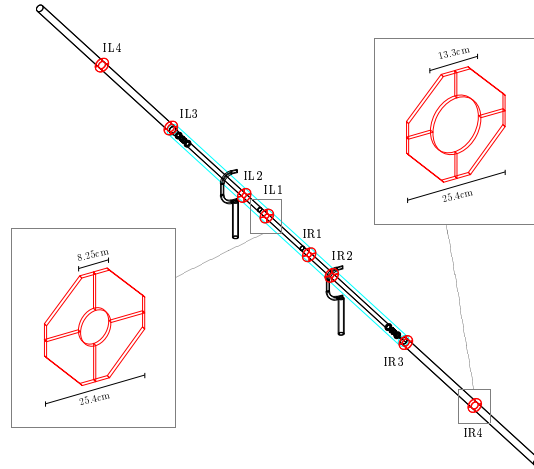


Figure 3.6: The inelastic counter setup.

The INEL rings also provide information on the event-by-event interaction point (vertex), through the difference in left and right arrival times of the first signal in an event (see page 54). For the data presented in this thesis, the experimental resolution of this determination is ~ 8 cm.

Beam-beam counters

On either side of the nominal interaction point are also positioned two arrays of plastic scintillator tubes known as the beam-beam (BB) counters, positioned at $z = \pm 2.19$ m and covering the pseudorapidity interval $2.2 < |\eta| < 4.6$. Like the INEL rings they give interaction point and triggering information, and also provide a forward pseudorapidity multiplicity measurement.

In central Au+Au collisions the BB counters give an experimental vertex resolution of 0.6 cm, corresponding to a timing resolution of 20 ps. For the present $p + p$ analysis, however, the average occupancy of the BB counters is too low for them to be of practical use.

Multiplicity array

Around the nominal interaction point BRAHMS also has two coaxial arrays of multiplicity detectors, one made up of silicon strips and one of plastic scintillator tiles. They provide mid- to intermediate pseudorapidity multiplicity information ($-2.2 < \eta < 2.2$), and have also been used for event plane determination and flow measurements in A+A collisions.

Like the BB counters, they have not been used for the present analysis.

Zero degree calorimeters

Finally, a pair of zero degree calorimeters (ZDCs) positioned at $z = \pm 18$ m are part of the experimental setup, providing centrality and interaction point information in A+A collisions by measuring spectator neutrons that are not swept away by the DX magnets.

The ZDC setup is common to all four RHIC detectors, and was intended to provide a common means of event characterization.

3.4 Trigger systems

The primary interaction trigger for the datasets presented here is the INEL array, as described in sec. 3.3. However, since the geometrical acceptance of each spectrometer arm is very low, two additional spectrometer triggers were implemented to increase the event sample with actual tracks. These triggers are defined as a coincidence between a hit in a spectrometer hodoscope (see below), and a trigger counter positioned at the front of the spectrometer. This counter also provides the start time for the track, for accurate calculation of the velocity. More information on the implementation of the triggers is given in sec. 4.1.

MRS start time counter

For the 2001 $p + p$ run, the MRS triggering and start time was provided by a single 50 cm wide plastic scintillator slat (TMRF) positioned in front of TPM1. Its size covers only part of the front of the detector, so the TMRF slat must be taken into account when calculating the spectrometer acceptance. This effect and the absorption effect of this slat on antiprotons is discussed in sec. 4.4.

For the 2003 runs, the TMRF trigger was segmented into 6 slats and renamed MrsT0. This gives the possibility of using the time measurement from this detector to extend the PID of the TOFW, as individual particles can be given individual start times. A proof-of-principle analysis has been done exhibiting usable particle identification capabilities for MrsT0, but it is not used as a PID detector for the present analysis.

FS start time counter

For both the 2001 and 2003 datasets, the FS start time and spectrometer triggering was provided by TD1, a set of three 11.5 cm wide scintillating slats positioned in front of D1. Again, the effects of this trigger detector, known as TD1, on acceptances, absorption etc. are discussed in sec. 4.4.

3.5 Tracking detectors

Particle position and directional information in BRAHMS is provided by a number of time-projection chambers (TPM1, TPM2, T1 and T2 in figure 3.3) and wire-based drift chambers (T3–T5 in fig. 3.3).

Time-projection chambers

The BRAHMS time-projection chambers, or TPCs, have active volumes ranging from 25 dm³ to 70 dm³. This volume is filled with a 90–10% gas mixture of Ar and CO₂, a combination which is easily ionized by passing charged particles. The freed electrons drift to a plane of anode wires and readout pads, along a homogeneous electric field in the global y direction. Three-dimensional “hits”, points along charged particle trajectories,

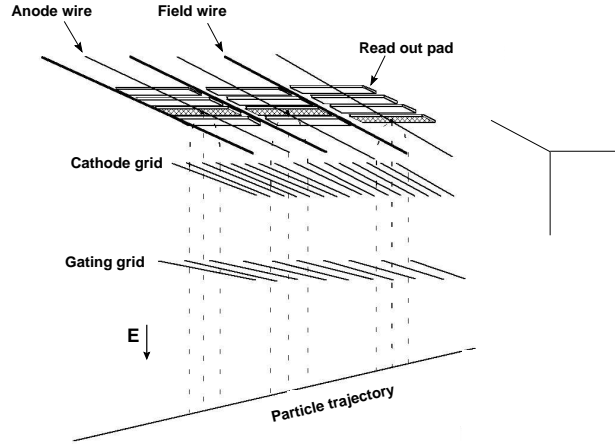


Figure 3.7: Schematic picture of the TPC readout plane and electron drift lines.

are reconstructed by combining the readout from several pads in a single row (giving the global x and z coordinates) with the electron drift time (giving the y coordinate from a known drift velocity).

See figure 3.7 for a schematic of the BRAHMS TPC design. Table 3.2 lists the actual sizes and other main characteristics of the individual TPCs. More details on both the TPC design and track reconstruction can be found in ref. [24].

Name	L (cm)	W (cm)	H (cm)	Gas mixture 90–10%	N_{row}	$N_{pads/row}$	$\langle v_{drift} \rangle$ (cm/ μ s)	$\langle \sigma_x \rangle$ (mm)	$\langle \sigma_y \rangle$ (mm)
T1	56.0	33.6	19.8	Ar–CO ₂	10 (14)	96	1.8	0.38	0.40
T2	75.5	39.6	19.8	Ar–CO ₂	8 (14)	112	1.8	0.37	0.41
TPM1	36.6	38.4	20.0	Ar–CO ₂	12 (12)	96	1.7	0.31	0.43
TPM2	50.0	67.7	19.8	Ar–CO ₂	10 (20)	144	1.6	0.39	0.49

Table 3.2: Main characteristics of the four BRAHMS TPC’s. L , W and H are respectively the length (z), width (x) and height (y) of the reactive volume, N_{row} the number of instrumented (total) pad rows, $N_{pad/row}$ the number of pads per row, $\langle v_{drift} \rangle$ is the measured average electron drift velocity along the drift lines (y direction) and the $\langle \sigma \rangle$ ’s are the average hit position resolutions.

Drift chambers

The three drift chambers in the BFS are wire chambers, each of them composed of three modules with 8–10 planes of parallel wires arranged in 1–4 “views” (azimuthal wire orientation). Like TPC’s, DC’s are also gas detectors but there is no homogeneous electric field. Instead, electrons created by gas ionization are attracted by a set of anode and field wires. When the correspondence between drift time and drift distance to the wire has been established, each hit in a view gives a line parallel with the view direction (wires), as shown in fig. 3.8. Since there is an ambiguity on the side of the wire the charged particle passed, at least two planes of the same view are needed. When the different views are combined, tracks can be determined by intersection of wires that were

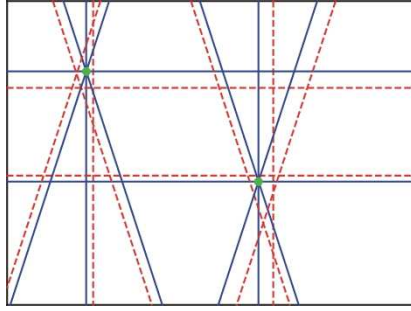


Figure 3.8: DC tracking in an ideal situation with two tracks crossing a wire plane containing four views. The DC is shown from its front and views are x (horizontal), y (vertical), u and v (intermediate angles). Each hit gives rise to two lines before the left/right ambiguity is solved (see text). The solid lines are the true ones. The green dots, intersections between the solid lines, belong to the two particle tracks.

hit (see fig. 3.8). More details on the DC design, tracking and performance can be found in [121, 128, 129].

3.6 Magnets

The five BRAHMS magnets are all conventional dipole electromagnets, with central apertures of approximately 30 cm by 10 cm. The field inside the aperture is approximately constant, having only a vertical (y coordinate) component. Field maps have been measured and are applied to the experimental data. Fringe fields have also been studied and are found to be minimal, not reaching the surrounding detectors.

Table 3.3 summarizes some characteristics of the magnets, including the mean momentum selected at a specified field fraction.

Name	Gap dim. (cm)			I_{max} (A)	B_{max} (T)	Average momentum $\langle p \rangle$ (GeV/c) per setting				
	L	W	H			1/8	1/5	1/4	1/3	1/2
D1	200	8.0	20.0	3450	1.26	p not determined				
D2	160	30.0	13.5	3000	1.68	2.0	3.0	3.5	5.0	6.5
D3	200	40.0	25.4	3000	1.22	3.0	4.5	5.5	7.2	10.0
D4	183	44.6	32.1	2750	1.19	3.0	4.5	5.5	7.2	10.0
						164	350	500	700	1000
D5	76.2	35.0	10.0	2500	1.45	0.30	0.35	0.40	0.45	0.55

Table 3.3: Characteristics of the BRAHMS magnets. I_{max} is the maximum current, i.e. at full field. By convention, MRS current settings are in A and not fractional like for the FS.

3.7 Time-of-flight systems

All BRAHMS time-of-flight systems, or hodoscopes, consist of scintillator slats with photomultiplier tubes attached at the top and bottom. They give a precise measurement

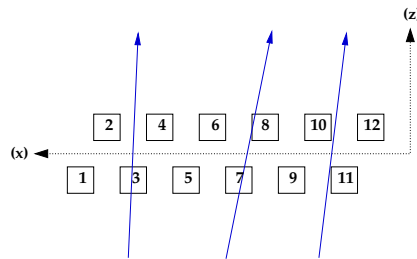


Figure 3.9: Track line extrapolation to hodoscope slats in the FS (H1 and H2) seen from top. The staggered construction improves the slat coverage, while the probability for a track to hit two slats is still very low.

of the time when a charged particle passes a slat, which combined with the start time from the trigger slat and the distance along the track from the hodoscope to the slat gives the particle velocity β . The hit y coordinate is also measured, from the time difference between signal readout on the top and bottom of the struck slat. Together with the particle momentum, this is enough to uniquely identify pions, kaons and protons in BRAHMS, up to certain velocity (see section 4.2). Table 3.4 summarizes the main characteristics of the three hodoscopes.

Forward spectrometer

In the forward spectrometer, the H1 and H2 hodoscopes are positioned at 8.7 m and 18.6 m from the IP respectively. H1 has 40 slats, while H2 has 32. Both hodoscopes have a nominal timing resolution of 75 ps, while the value obtained experimentally is $\sigma_t \leq 100$ ps depending on the track density.

The signal in a hodoscope comes from the particle energy deposition dE/dx as it traverses a slat. A potential problem then comes from tracks passing through only a corner of a slat or exactly between two, and not depositing the expected amount of energy. To reduce this efficiency problem, H1 and H2 are constructed with the slats in two staggered rows - see illustration in fig. 3.9.

Midrapidity spectrometer

In the MRS, the time-of-flight wall (TOFW) consists of six panels positioned in an arc around the center of the D5 magnet. Unlike H1 and H2, the TOFW slats are all in one plane and the light is transferred to the photomultiplier tubes via light guides. The experimental timing resolution of the TOFW is similar to H1 and H2.

For the 2001 RHIC run the TOFW was not fully implemented, with only four of six panels instrumented in an asymmetric configuration. The available panels started from the left-hand side of the TOFW as seen from the IP, resulting in positive particles being heavily favored for runs with polarity A on the D5 magnet and vice versa. The effects of this are discussed further in sec. 4.3. For the 2003 data is not so pronounced due to better instrumentation of the TOFW.

Name	Distance from IP (m)	N_{slat}	Slat dim. (cm)			Material (bicron)	σ_t (ps)	p_{max} (GeV/c)	
			L	W	H			π/K	K/p
TOF1	8.7	40	1.00	1.00	20	BC420	75	3.8	6.5
TOF2	18.6	32	1.00	1.50	40	BC420	75	5.8	9.7
TOFW	4.3	125	1.27	1.25	22	BC404	75	2.5	4.3

Table 3.4: Characteristics of the BRAHMS hodoscopes. σ_t is the nominal time resolution of each tube, p_{max} is the nominal PID capability in a 3σ cut assuming the overall TOF resolution equals 75 ps, i.e. the maximum momentum below which the particle can be identified. (The values listed are the best separation achievable. See sec. 4.2 for the experimentally achieved PID resolution.)

3.8 Cherenkov detectors

To extend the particle identification from time-of-flight, BRAHMS has several subsystems that can give PID information based on Cherenkov radiation, i.e. the light signal emitted if a particle has a velocity higher than the speed of light of the surrounding medium. This light emission takes place on a conical surface around the direction of the particle momentum, with an opening angle that depends only on the particle velocity β and the index of refraction n of the medium.

This implies that there is a mass-dependent threshold momentum below which particles do not produce Cherenkov light, given by

$$p_{th} = \frac{m}{\sqrt{n^2 - 1}} \quad (3.2)$$

where m is the particle mass and n is the refractive index. For a particle of charge Z above this momentum threshold value traversing a length L of detector material, the number of Cherenkov photons radiated is given by

$$N_\gamma \propto Z^2 L \left(1 - \frac{1}{\beta^2 n^2} \right) \quad (3.3)$$

The threshold values for the BRAHMS Cherenkov detectors are listed in table 3.5 along with some other detector characteristics.

Threshold Cherenkov detector

At the back of the FFS is a threshold Cherenkov counter (C1). It consists of a chamber with a radiator gas, a set of mirrors at the back that reflect the produced light up or down, and an array of photomultiplier tubes on the top and bottom of the detector to read out the signal. See the left panel of figure 3.10. C1 has 32 tubes, and covers the entire spectrometer aperture.

A concern has been that the amount of dense material in C1 might be a source of background for measurements with the BFS. Therefore, it is designed to be moved out of the spectrometer for low-angle, high-momentum settings where it is of little use for PID. For the present datasets, this was done for the 3° and 4° settings.

For later runs a threshold Cherenkov counter similar to C1 was also installed behind the TOFW in the MRS. This detector, known as C4, has 16 tubes but is otherwise of identical design to C1.

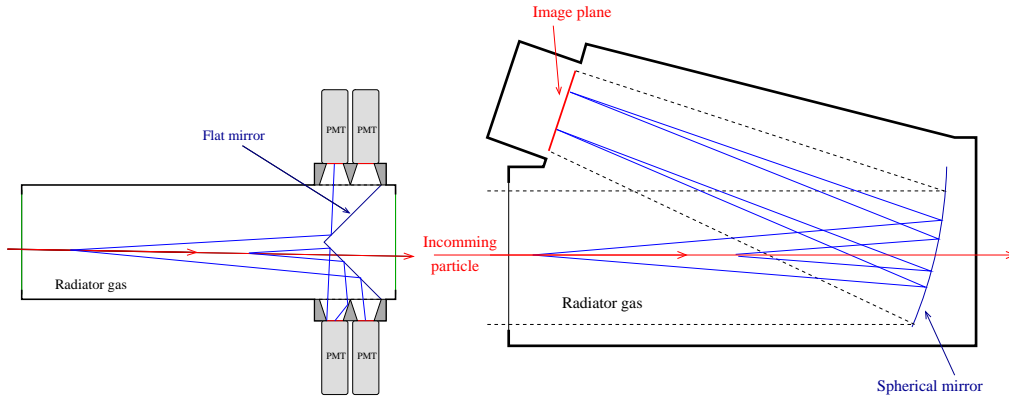


Figure 3.10: Side views of the Cherenkov detectors implemented for the 2001 and 2003 runs. Left: C1, a threshold detector. Right: RICH, a ring-imaging detector, with spherical focusing mirror and segmented image plane.

Ring imaging Cherenkov detector

At the back of the BFS is the final PID instrument, a ring-imaging Cherenkov detector (RICH). Like C1 it has a volume filled with radiator gas, but the RICH also has a spherical focusing mirror and a focal plane with a finely segmented light detector. All Cherenkov light emitted from the trajectory of one particle will be reflected onto one ring in the focal plane, with a ring radius determined by the opening angle of the cone. This allows us to measure the exact angle of the Cherenkov radiation and in turn calculate the particle velocity. Combined with the momentum, this gives particle identification over a very broad momentum range. The right panel of figure 3.10 shows a side view of the RICH.

	N_{tube}	Gas	n	p_{μ}	p_{π}	p_K	p_p
C1	32	C_4H_{10}	1.00138	2.01	2.65	9.39	17.85
RICH	4×80	C_4H_{10}	1.00202	1.66	2.19	7.76	14.75

Table 3.5: Characteristics of the BRAHMS Cherenkov detectors. The p 's are the momentum thresholds of the listed particles. Indices of refraction vary somewhat during a data run due to ambient pressure variations, and are subject to offline calibration.

Chapter 4

Analysis of the 2001 $p + p$ dataset

The results in this thesis are presented in a self contained way as a set of papers in chapter 5, together with a brief introduction. The main conclusions are summarized in chapter 6. The present chapter gives a more detailed outline of the process of data reduction, correction and analysis that has led up to the results.

The discussion is mainly focused on the $p + p$ dataset from the 2001 RHIC run, which has been the main subject of my work and is presented in the third and fourth included papers. Some comments relating to the $d + Au$ and $p + p$ datasets from 2003, used for the first papers in chap. 5, are also included where the process differs significantly from the main analysis.

I will first discuss the event selection, data reduction and the reconstruction of raw tracks and PID information, then the corrections applied to the data to get the normalized particle production for a given spectrometer setting. Finally I show how the different settings are combined into a unified measurement, and give some details on the construction and integration of particle spectra and the associated systematic errors.

4.1 Data reduction

Data reduction in BRAHMS consists of three main steps:

1. **Event selection** via a set of on-line triggers
2. **Track reconstruction**, first at the local level in each tracking detector and then globally through a whole spectrometer arm
3. **Particle identification** by combining a track with information from time-of-flight and Cherenkov detectors

Triggering and event selection

The first requirement for measuring an interaction is being able to recognize events with the required characteristics, and measuring just when they occur. This information is provided by the interaction trigger, and for the dataset discussed here this was provided by the two sets of inelastic counters discussed in section 3.3. See table 4.1 for a listing of trigger definitions used for the 2001 $p + p$ run. An interaction trigger is defined as

Trigger	5	3	6
Definition	INEL	TMRF + TOFW	TD1 + H1
Description	Interaction trigger	MRS trigger	FFS trigger

Table 4.1: The most important BRAHMS trigger definitions during the 2001 $p + p$ run.

hits in both the left and right arrays within a narrow time window, meaning that what we record is the non–single–diffractive (NSD) cross–section (see sec. 2.1). GEANT simulations with input from PYTHIA have shown that the coverage of the INEL rings lets us measure $71 \pm 5\%$ of the 41 mb $p + p$ total inelastic cross–section at $\sqrt{s} = 200$ GeV.

Since the geometrical acceptance of each spectrometer arm is very low, two additional spectrometer triggers were implemented to increase the event sample with actual tracks:

- The MRS trigger was defined as a coincidence between the start–time slat in front of TPM1, and a hit in the time–of–flight wall. The start–time slat is TMRSF for 2001 data and MrsT0 for 2003 data.
- The FS trigger was defined as a coincidence between the start–time slat TD1 in front of D1, and a hit in H1.

To record the maximum possible number of tracks within the available DAQ bandwidth each of the three triggers was scaled down by a suitable fraction n , meaning that only every n th trigger was recorded. To normalize the final spectra to the correct number of track per event, they must therefore be scaled by a factor

$$f_{norm} = \frac{n_{spec}}{n_{interaction} \cdot N_{rec.events}} \equiv f_{scaledown} \cdot \frac{1}{N_{rec.events}} \quad (4.1)$$

rather than just $1/N_{events}$. Here n_{spec} and $n_{interaction}$ are the scaledown factors of the spectrometer and interaction triggers and $N_{rec.events}$ is the number of events actually recorded.¹

For the 2001 dataset, n_{FS} is always 1, n_{MRS} varies between 1 and 6 and $n_{interaction}$ varies between 100 and 2000. Similar numbers apply for the 2003 data. Figure 4.1 shows the number of actual triggers selected for analysis for the various spectrometer angles used in the $p + p$ soft survey analysis presented here.

In all, the analysis of 2001 data consists of 4.1M events with tracks in the spectrometers and 3.2M NSD interactions for normalization, as recorded by the INEL trigger.

Interaction point determination

For each event, the interaction point, or **vertex**, is calculated from the time difference of hits in the INEL rings. If two rings with equal distance from the nominal interaction point were struck, the formula for calculating the event z coordinate is

$$z = \frac{c}{2} (\langle t_L \rangle - \langle t_R \rangle) \quad (4.2)$$

where $\langle t_L \rangle$ and $\langle t_R \rangle$ are the average time signals in the left and right detector, respectively. Extensions for rings with non–equal distances to $z = 0$ are straightforward. Time signals well outside the average for an event (outliers) are excluded, and both start–time and slewing calibrations are applied.

¹The factor $f_{scaledown}$ is used in the total correction factor applied to the spectra on page 75.

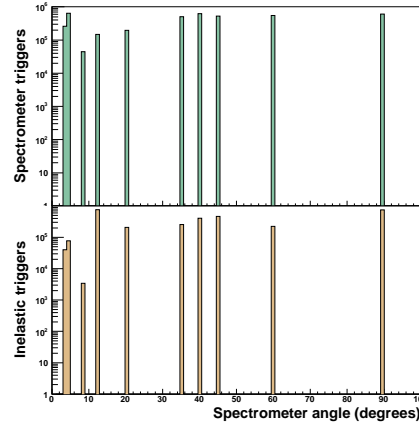


Figure 4.1: Number of triggers used in the analysis of the 2001 $p + p$ dataset. See also table 4.2 on page 59.

Figure 4.2 shows the experimental resolution of the vertex determination, by comparing the INEL vertex with the back-projection of tracks from events with the spectrometer trigger satisfied. The average value is

$$\langle \sigma_z^{INEL} \rangle \approx 8cm \quad (4.3)$$

Local and global tracking

In the first data reduction step, local tracks are reconstructed in each of the TPCs and DCs (see chapter 3 and refs. [24, 121] for details). For each pair of consecutive detectors, the tracks are then matched by tracing a helical arc through the magnet gap between them (see fig. 4.3). The particle momentum can then be determined from the bending angle:

$$p = \frac{qB\Delta L}{\Delta\theta} \frac{1}{\sqrt{1 - \alpha_y^2}}. \quad (4.4)$$

Here $\Delta\theta$ is the total bending angle between a pair of trackers and α_y is the slope of the track in the y direction. See appendix B for details.

For the midrapidity spectrometer, a matched track through the TPM1–D5–TPM2 complex gives a unique measurement of the particle trajectory and momentum. Cuts on the three-dimensional matching parameters and on the track distance from the iron in the magnet are imposed, and surviving tracks are flagged as good particles. (See sec. 4.3 for a discussion of the cuts imposed.)

This procedure is also used for the front forward spectrometer, where the relevant detectors are T1–D2–T2. Accepted tracks are then swum back through the D1 magnet using the momentum from D2, to find the intersection with the beamline and thus the assumed track origin.

For the full forward spectrometer, tracks are matched as above for the T1–D2–T2, T3–D3–T4 and T4–D4–T5 detector combinations. Matched tracks are then combined into one global track. This procedure yields three measurements of the momentum,

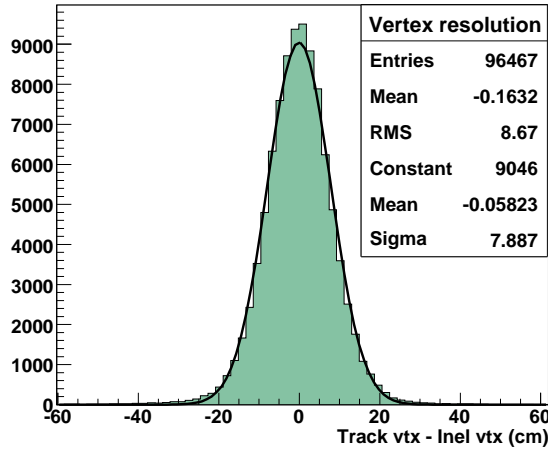


Figure 4.2: Example of experimental resolution of vertex determination from INEL counters.

which have been shown to be consistent after position and magnetic field map calibrations. See the left panel of figure 4.4 for an example correlation, here between the momenta determined from the D2 and D4 magnets. There are some systematic deviations, especially at low p , that need to be treated. For this, a refit is done using all available information assigned to a single track to yield the best possible FS trajectory and combined track momentum. The right panel of figure 4.4 plots this refitted FS momentum for the same dataset, versus the straight average of the momenta from D2 and D4. The refit is close to this average for all momenta, with only minor deviations due to other constraints, and on average correlates well with all individual momentum determinations.

Table 4.2 summarizes which detector subsystems are used for which setting.

4.2 Particle identification

After reconstructing the momentum and trajectory of a charged particle, the next step is to positively identify it as a pion, kaon or a proton. In BRAHMS this is done either through time-of-flight methods or by Cherenkov detectors, or a combination of the two principles. Table 4.2 summarizes which PID methods are used for each setting in the present analysis. The different methods and their experimental resolutions are briefly discussed below. For a more details on the BRAHMS tracking angular and momentum resolutions, see appendix B.

Time-of-flight PID

The present analysis uses time-of-flight (TOF) particle identification for all MRS settings, using the TOFW detector, and for the 20° and 12° FS settings using the H1 detector. Identification is done by plotting the particle mass (m^2), determined as

$$m^2 = p^2 \left(\frac{1}{\beta^2} - 1 \right) \quad (4.5)$$

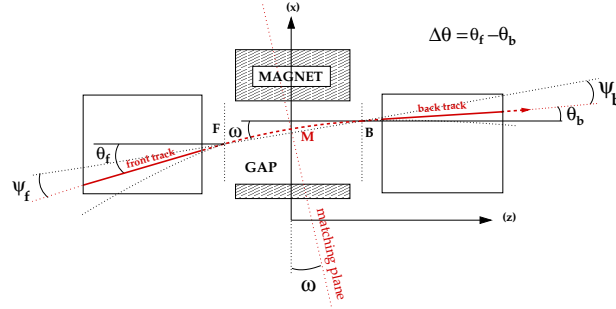


Figure 4.3: Top view of the matching geometry: tracking detector – magnet – tracking detector. F and B denotes the intersection point between the track and the effective edges of the magnetic field. The matching is done by comparing ψ_f and ψ_b which are the angle differences between the local tracks (front and back) and the line $|FB|$ in the $x-z$ plane. Cuts on the difference in y position and slope α_y of the tracks are also imposed. If the local tracks match (originate from the same particle), they should fulfill $\psi_f = \psi_b$. Figure from [21].

as a function of its momentum. See e.g. figures 4.5 and 4.6. In this representation, the resolution can be determined experimentally by differentiating this equation with respect to p and β . Propagation of errors then gives us that

$$\left(\frac{\sigma_{m^2}}{m^2}\right)^2 = 4\gamma^4 \left(\frac{\sigma_{p^2}}{p^2} + \frac{\sigma_{\beta}^2}{\beta^2}\right) \quad (4.6)$$

We now define a timing resolution σ_t from the determination of β :

$$\sigma_t^2 \equiv \frac{\sigma_{\beta}^2}{\beta^2} \quad (4.7)$$

and from the discussion in app. B (see eq. B.5) we can extract the dependences of the multiple scattering and angular determination contributions:

$$\frac{\sigma_{p^2}^2}{p^2} = p^2 \sigma_{\theta_{f+b}} + \beta^2 \sigma_{\theta_{ms}} \quad (4.8)$$

$$= p^2 \sigma_{\theta_{f+b}} + \left(1 + \frac{m^2}{p^2}\right) \sigma_{\theta_{ms}} \quad (4.9)$$

Here the σ s have been redefined to include all the detector constants discussed in the appendix. The total m^2 resolution then becomes (using $\gamma = E/m$)

$$\sigma_{m^2}^2 = 4(m^2 + p^2)^2 \left[p^2 \sigma_{\theta_{f+b}}^2 + \left(1 + \frac{m^2}{p^2}\right) \sigma_{\theta_{ms}} + \sigma_t^2 \right] \quad (4.10)$$

To get an experimental determination of this resolution, the m^2 distribution is plotted for narrow momentum slices and the widths $\sigma_{\pi}(p)$, $\sigma_K(p)$ and $\sigma_p(p)$ are determined by fitting with gaussians. For each particle, the width is fitted to Eq.4.10 as a function of momentum, and values for $\sigma_{\theta_{f+b}}^2$, σ_t^2 and σ_{ms}^2 can be extracted. The experimental

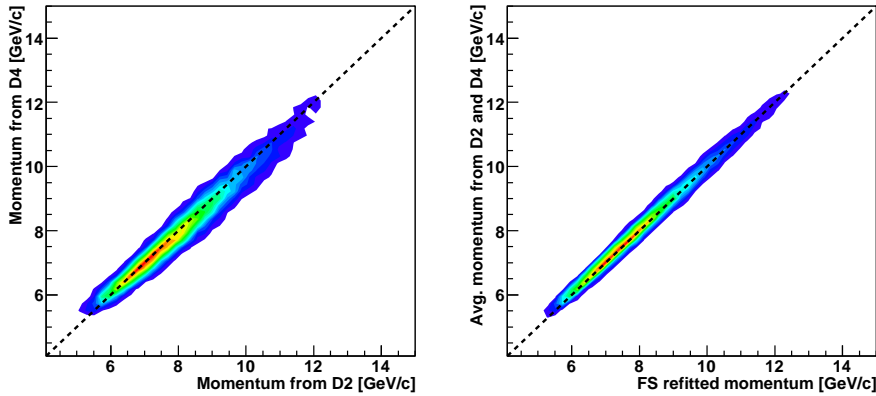


Figure 4.4: Left: Correlation of the momentum from D2 with the momentum from D4, for data from the 3° setting. The line is $p_{D2} = p_{D4}$. Right: The refitted FS momentum (see text) versus the average momentum from D2 and D4.

values obtained are consistent with the values calculated from spectrometer properties, as discussed in ref. [21].

Figures 4.5 and 4.6 show examples of the TOFW and H1 PID distribution, overlaid with the experimentally determined resolution. The curves in the left panels denote $2\sigma_m^2$ deviations from the mean. Particles can be uniquely identified in the regions where $|p|$ is lower than the intersection points of the lines, resulting in the separation shown in the right panels.

Threshold and Ring Imaging Cherenkov PID

For the most forward rapidities covered in this dataset, corresponding to the 4° and 3° spectrometer settings, PID is done using the RICH detector at the rear of the forward spectrometer. The RICH records a light ring for each charged particle traversing it, and plotting the radius of this ring versus the particle momentum yields a particle identification.

In more detail, the m^2 of a particle in the RICH can be written as

$$m^2 = p^2(n^2 \cos^2 \theta_C - 1) = p^2 \left(\frac{1}{\beta^2} - 1 \right) = p^2 \left(\frac{n^2 L^2}{L^2 + r^2} - 1 \right) \quad (4.11)$$

where r is the ring radius, L is the focal length of the RICH mirror and n is the refractive index of the detector gas. θ_C is the angle of the Cherenkov light cone. Note that while L is a geometrical constant of the detector, the refractive index n will vary with ambient and internal gas pressure. This is calibrated by tuning the centroids of the observed m^2 peaks to the known values.

Differentiating equation 4.11 with respect to r and p (n and L are assumed to be known constants) we can estimate the m^2 resolution:

Setting (deg.)	Spec. triggers	Inel. triggers	Detectors used	PID methods
90	602k	755k	TPM1, D5, TPM2, TOFW	TOF
60	551k	223k	TPM1, D5, TPM2, TOFW	TOF
45	526k	463k	TPM1, D5, TPM2, TOFW	TOF
40	620k	405k	TPM1, D5, TPM2, TOFW	TOF
35	504k	257k	TPM1, D5, TPM2, TOFW	TOF
20	195k	209k	T1, D2, T2, H1	TOF
12	148k	759k	T1, D2, T2, H1, C1	TOF, threshold Cherenkov
8	45k	4k	T1–T5, D2–D4, C1	TOF, thr. and ring imaging Cherenkov
4	640k	78k	T1–T5, D2–D4, RICH	Ring imaging Cherenkov
3	260k	40k	T1–T5, D2–D4, RICH	Ring imaging Cherenkov
Total	4.09M	3.19M		

Table 4.2: Summary of available data and subsystems used for the various spectrometer angle settings used in the analysis.

$$\frac{\sigma_{m^2}^2}{m^2} = \left(\frac{\partial(m^2)}{\partial p} \sigma_p \right)^2 + \left(\frac{\partial(m^2)}{\partial r} \sigma_r \right)^2 \quad (4.12)$$

$$= \left[2p \left(n^2 \frac{L^2}{L^2 + r^2} - 1 \right) \sigma_p \right]^2 + \left[2p^2 n^2 \frac{rL^2}{L^2 + r^2} \sigma_r \right]^2 \quad (4.13)$$

$$= \left[2p \left(\frac{1}{\beta^2} - 1 \right) \sigma_p \right]^2 + \left[2p^2 \frac{L\sqrt{\beta^2 n^2 - 1}}{\beta^2} \sigma_r \right]^2 \quad (4.14)$$

Here I have used the relation $1/\beta^2 = 1 + m^2/p^2$. As for the TOF systems, we can now experimentally determine the PID resolution and set $2\sigma_m$ cuts around the known particle mass values in the m^2 vs. p plot. Figure 4.7 shows an example distribution from the 3° setting.

Since the RICH has separate light thresholds for particles with different mass (see eq. 3.2 on page 50), it can also be used as a veto counter for protons in the momentum region above the kaon threshold. For the present analysis, if a track has a reconstructed momentum $p > 9.0$ GeV/c (1.0 GeV/c above the kaon threshold, since above this point the RICH is highly efficient — see figure 4.22 on page 74 for details) and intersects the RICH but has no associated ring, it is identified as a proton. An upper cut of $p > 16.0$ GeV/c is also set, corresponding to 2.0 GeV/c above the proton threshold. As is evident from fig. 4.7 there are very few (anti-)protons above threshold in the present analysis, so the RICH veto mode is the primary p , \bar{p} identification method at 3° and 4° . Note however that the proton sample from this method is prone to contamination of π and K due to RHIC inefficiencies or absorption/decays in the last parts of the FS. A correction for this effect is discussed in section 4.4.

For the 12° and 8° settings, a threshold Cherenkov detector (C1) is also used. Its sole function is to uniquely identify pions in the momentum region below the kaon threshold, and then to veto these from the H1 PID distribution. This allows for effective TOF PID of kaons up to the C1 kaon threshold. See figure 4.8 for an example plot from a 12° setting,

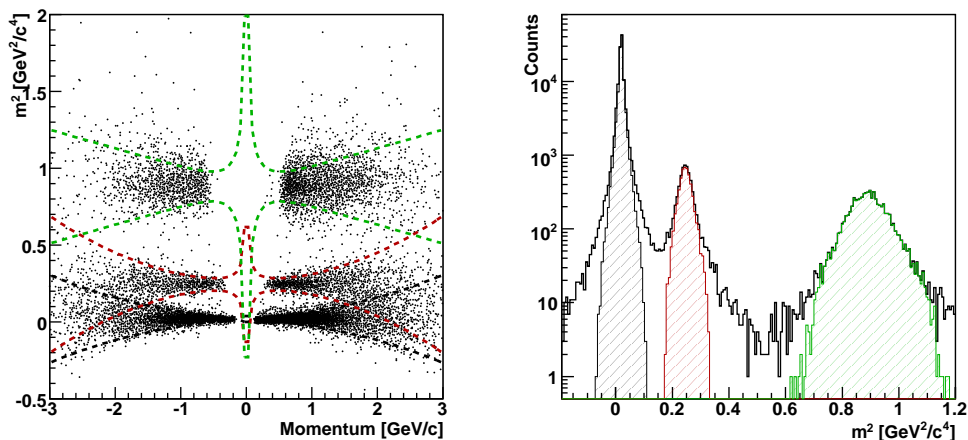


Figure 4.5: Particle identification from the MRS time-of-flight wall, from the 60° $1/4$ field setting. Left panel: m^2 vs. momentum with resolution fits as discussed in the text. Right panel: The resulting separation in experimental m^2 , where the unshaded histogram shows all accepted particles.

where the two right panels show H1 identification with and without pions identified in C1.

4.3 Analysis cuts

The sample of positively identified particles will still contain undesired secondary particles and misidentified tracks. To remove as many of these as possible, a range of cuts are imposed on the data sample:

1. A number of fiducial cuts are imposed to remove any edge effects due to the limited spectrometer size.
2. Cuts are set on the matching parameters through all tracker-magnet-tracker combinations, most importantly in the y and α_y coordinates (see sec. 4.1).
3. Secondaries are vetoed by projecting the track back to the known interaction point.

The cuts and their effects are discussed in detail below.

Fiducial cuts

The reason for having fiducial cuts is that it is hard to reconstruct the behavior of tracks near the edges of the spectrometer, i.e. close to TPC or magnet walls. They may be secondary particles from interactions with the detector walls or primaries that have undergone severe scatterings, or they may have traversed inhomogeneities in the magnetic or electric fields close to the edges. To remove any such effects, three cuts are imposed in the present analysis, all of which are also included in the acceptance corrections discussed in sec. 4.4.

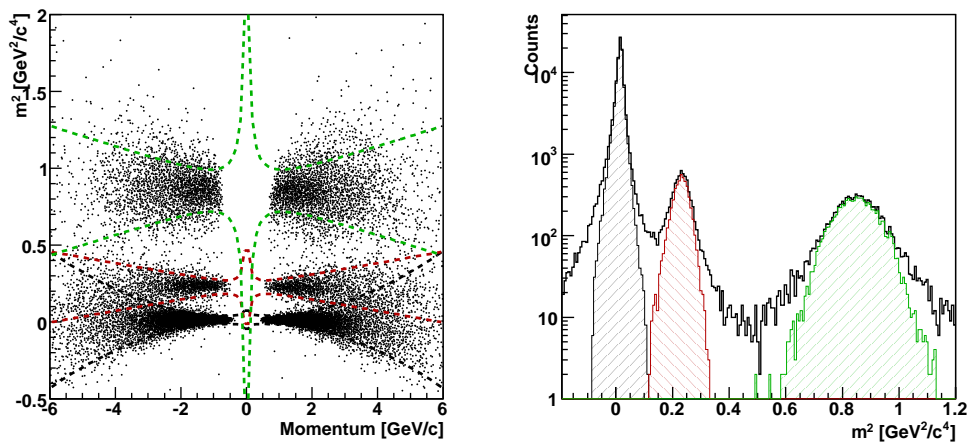


Figure 4.6: As figure 4.5, for H1 at 20° 1/12 field.

Magnets

A cut of 0.5cm on the closest distance of a track to the magnet wall is imposed. For the MRS this cut is set in the D5 magnet, for the FFS it is set in both the D1 and D2 magnets and for full FS tracks for D1–D4.

Tracking chambers

To avoid the edges of the tracking detectors, a cut is set on the track position at the back plane of TPM2 in the MRS and T2 in the FFS. This position is used because it is the narrowest part of the acceptance for the MRS and FFS respectively. The cuts used are

- TPM2: $-15 \text{ cm} < x < 20 \text{ cm}, -7 \text{ cm} < y < 3 \text{ cm}$
- T2: $-12 \text{ cm} < x < 17 \text{ cm}, -8 \text{ cm} < y < 6 \text{ cm}$

corresponding approximately to a 1 cm cut away from the experimental edges of the detectors, i.e. the region where we observe reconstructed tracks. See figure 4.9 for an example.

Time-of-flight wall

For the 2001 RHIC run the TOFW was not fully implemented, with only four of six panels instrumented (70 out of a nominal 125 scintillating slats were active). We observe a dropoff in track density close to the edges of the instrumented range, so a fiducial cut on the slat number has been imposed to remove this edge effect. In slat number, the cut is $25 \leq \text{slat} \leq 75$. See figure 4.10 for an example. The smooth dropoff on the left side of the distribution (low slat numbers) comes from the actual particle distribution, and the steepness varies with the D5 magnetic field (i.e. the mean amount of track bending). The sharp drop on the right side (high slat numbers) represents the edge of the TOFW instrumentation. As the shaded region shows, we impose a cut on both sides to remove any possible edge effects.

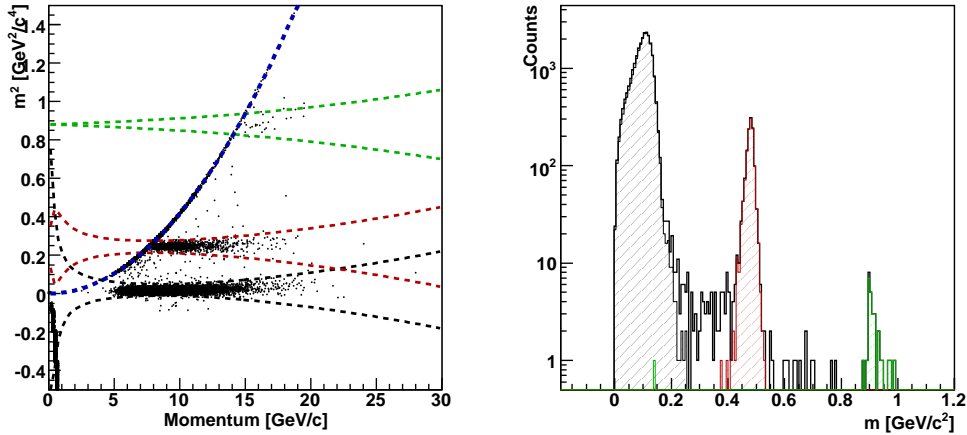


Figure 4.7: Particle identification from the FS RICH, from the $3^{o}1/3$ field setting. Left panel: m^2 vs. momentum with resolution fits as discussed in the text. The sharply rising line shows the threshold momentum. Right panel: The resulting separation in experimental m (both charge signs).

Note that the TOFW is designed to be symmetric around a straight line through the spectrometer, to give equal geometric acceptances for both charges in a single polarity. Since the TOFW design has 125 slats this implies a symmetry around slat 63, so clearly the above fiducial range gives asymmetric acceptance for positive and negative particles. The setup is such that for polarity A positive particles are favored, and vice versa.

The coverage in the $y - p_T$ plane of the disfavored particles is so narrow that it is heavily dominated by edge effects. See figure 4.11 for an example. For the 2001 charged particle production analysis, I have for this reason chosen to only include the favored charge sign from each spectrometer setting, i.e. positive particles from polarity A and negatives from polarity B.

For the 2003 datasets used in the first paper in chapter 5 the TOFW was better implemented, though still not fully functional, and from the experimental hit distributions a fiducial cut $29 \leq \text{slat} \leq 114$ was set. While still asymmetric, both charge signs here have reasonable $y - p_T$ coverage and have been used in the analysis.

Matching cuts

For each tracker–magnet–tracker pair, local tracks are matched as shown in figure 4.3. To remove accidental associations of unrelated local tracks, tracks that scatter off the edges of the magnets, have decayed between the trackers etc., cuts are imposed on the angle difference $|\psi_f - \psi_b|$ defined in figure 4.3, on the projected track y position at the magnet midplane, as well as the track slope in the vertical direction α_y . See figure 4.12 for example distributions. For the present analysis, wide cuts have been used so that they do not cut into the signal peak while still removing most uncorrelated tracks.

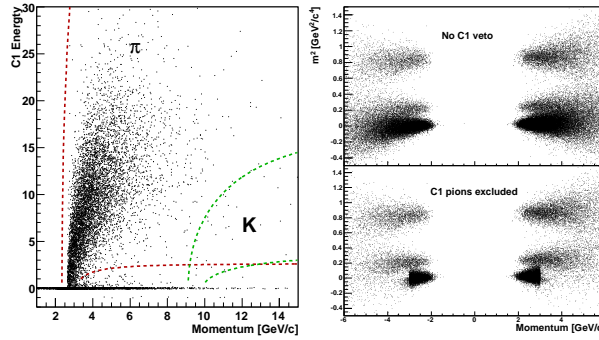


Figure 4.8: Left: C1 reconstructed energy vs. associated track momentum, for a 12° $1/4$ field setting. Lines show wide cuts around the theoretical energy response curve. Right: m^2 vs. momentum from H1 for all particles (top), and the same with pions identified in C1 excluded (bottom).

Projections to the interaction point

Currently the data sample contains all particles that are reconstructed through the spectrometers. This will also include a number of unwanted particles that have survived the fiducial cuts, like secondaries from weak decays and products of interactions with the beam pipe, trigger slats or magnet walls. The first case is especially important in the MRS which has a comparatively large acceptance, while the last case is significant for the FS which has a magnet positioned before the first tracking chamber.

To reduce the contribution of such particles, we can look at the track projection back to the known interaction point. Letting the projection go back to the global $x = 0$ plane, i.e. a vertical plane along the beam axis, we can set cuts in two dimensions:

1. The particle position in y at $x = 0$.
2. The distance from the particle position in z at $x = 0$ to the interaction point.

Figure 4.13 shows examples of such projections with the resulting cuts. In the analysis, the cuts are re-tuned for each setting by fitting gaussians to the experimental distributions. 2σ cuts are used around the fit mean, and the resulting losses are compensated for. On average, the cuts used are $\langle\sigma_y\rangle = 0.5$ cm for both spectrometers, $\langle\sigma_z^{MRS}\rangle = 5.3$ cm and $\langle\sigma_z^{FS}\rangle = 8.0$ cm.

It is clear from fig. 4.13 that some degree of background from secondaries apparently coming from the interaction point still remains under the signal peak. This effect is discussed below.

4.4 Corrections

At this point we have a raw yield of particles, i.e. just the number of particles per event that has been recorded by the spectrometer. This number must now be corrected for:

1. Loss of primary particles due to in-flight effects, such as absorption in the detector material, multiple Coulomb scattering in the traversed medium and weak decays of pions and kaons.

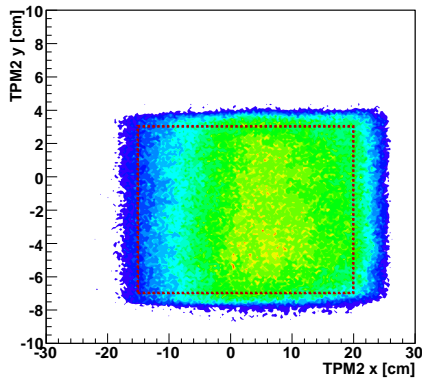


Figure 4.9: Fiducial cut on track position at the backplane of TPM2, 60° 1/4B field. The experimental edges and track density distribution varies somewhat with the field setting, so cuts are set that are inside the edges for all settings.

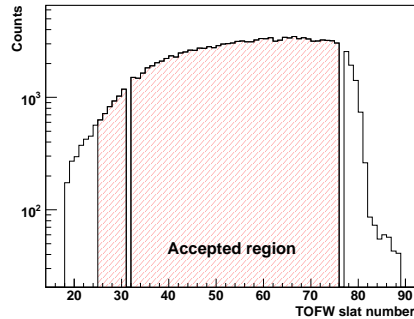


Figure 4.10: Fiducial cut on TOFW slat number. Figure shows all slats struck by reconstructed particles in a 60° 1/4B field setting (2001 run), and the shaded region shows the accepted hits. The two empty bins are defective slats.

2. Any remaining background from interactions with the detector material and charged decay products of unstable particles (i.e. secondaries).
3. Feed-down from $(\bar{\Lambda})\Lambda$ decay, which is given special treatment in the case of (anti)protons.
4. The geometrical acceptance of the detectors, since we are interested in the total number of particles produced and not just the ones that went through the spectrometer.
5. The combined efficiency of both the detectors themselves and the software used to reconstruct the tracks and determine the PID.
6. For protons identified using the RICH in 'veto mode' (see below), any contamination from misidentification of particles.
7. Any other effects that may bias the number of tracks seen, here especially the fact that the trigger system somewhat disfavors low-multiplicity events.

These corrections will now be discussed in turn.

Absorption, multiple scattering and in-flight weak decays

The effects of absorption, multiple Coulomb scattering and in-flight weak decays have been studied using a GEANT simulation of the full detector setup. GEANT allows us to specify which physics processes to include, so to study the individual contributions we first run the simulation with a given process turned off, and then compare this with a similar simulation with the process on. Note that we to a certain degree assume these

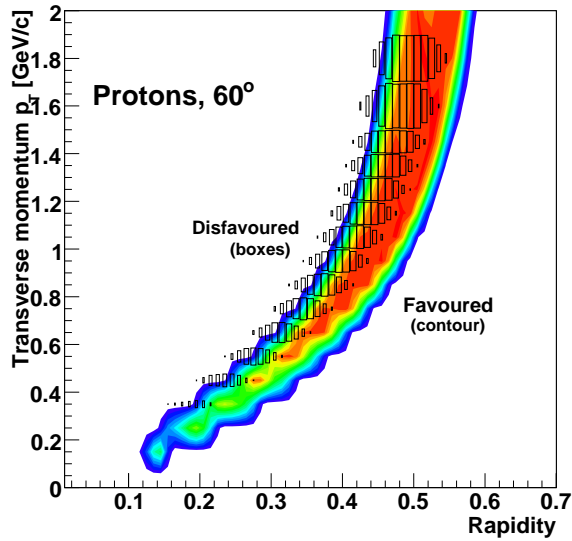


Figure 4.11: 2001 dataset: Comparison of proton acceptance at 60° for favored (contour) and disfavored (boxes) charges. Edge effects are felt where the color changes rapidly or the boxes are small. Cutting this area away leaves a wide usable coverage for the favored charge but not for the disfavored.

corrections to be independent of each other, so that e.g. absorption in a trigger slat can be studied independently of multiple scattering in the rest of the spectrometer.

All three processes have been studied as a function of momentum, spectrometer (MRS, FFS or full FS) and angle setting. Figure 4.14 shows example plots from MRS at 60° and FS at 4° . The most significant corrections are for kaon in-flight decay and p and \bar{p} losses due to interactions with detector material. The latter comes mainly from the beampipe and the trigger slats TMRF and TD1. Other corrections reach a level of $>95\%$ before $p = 1$ GeV/c.

Another effect which might be discussed as part of this set of corrections is the contribution to the p yield from protons knocked out of the beampipe or trigger slats. This has been evaluated for the BRAHMS 2001 setup in ref. [38] and found to be negligible for the p_T/m_T ranges we discuss. For the present analysis this is assumed to be the case also for $p + p$ collisions at the same energy. One thing that may need further checking is the additional effect of the trigger slats in front of the spectrometers, since these were not present for Au+Au in 2001. However, they are only expected to contribute in the momentum range $p_T < 500$ MeV/c [130], and as will be shown in the next chapter this region is not much used in the present analysis.

Background subtraction

As seen above, the cuts on the track projection to the interaction point leave a contribution of secondaries in the event sample. To estimate the magnitude of this effect, a more detailed analysis is made of the track y projections after all other cuts are applied.

The amount of decay products and results of secondary interactions will be both

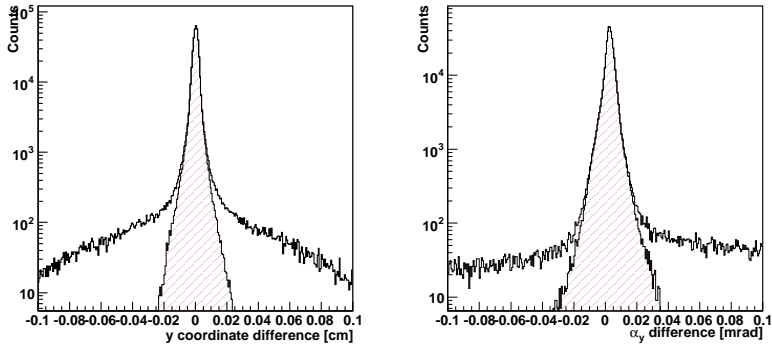


Figure 4.12: Effect of wide simultaneous cuts in the particle y position at the magnet midplane (left) and the track slope difference (left) in the FFS, i.e. for the T1–D2–T2 complex. Data from a 4° 1/4A run.

momentum and species dependent. The left panel of figure 4.15 shows the y projection for unidentified hadrons as a function of p_T for the 60° setting, and it is clear that the major background contribution lies at low momenta.

To get a qualitative estimate, the left panel of figure 4.15 is cut into p_T slices, and each plot is fitted with the sum of two Gaussian distributions. See the four right-hand panels of figure 4.15. Dividing the double Gaussian into a signal and a background distribution, the background is estimated from the fits as

$$F_{bg}(p_T) = \frac{\int_{\mu-2\sigma}^{\mu+2\sigma} f_{backgr}(y)}{\int_{\mu-2\sigma}^{\mu+2\sigma} f_{doublegauss}(y)} \quad (4.15)$$

where μ and σ are the mean and widths of the signal distribution. This is the same track projection region that is actually used in the analysis.

The same analysis is done for all angle settings and all particle species. For kaons and protons it is not possible to distinguish a background distribution from the signal peak, so no correction is applied for these particles. This is consistent with the background to a large extent coming from pions from in-flight weak decays, like the decay modes $\Lambda \rightarrow \pi + p$ and $K_s^0 \rightarrow \pi^+ + \pi^-$. Unfortunately, this also means that this method does not reduce the contribution to the proton yields from this kind of feed-down.

Figure 4.16 shows the calculated correction factor F_{bg} applied to the data, as a function of p_T , for two selected angle settings.

Feed-down corrections

Even after the above corrections, our measured data sample will invariably contain a certain contribution from the products of non-primary interactions or weak decays. In particular, the proton and antiproton samples will be contaminated by the products of the decay channels

$$\begin{aligned} \Lambda &\rightarrow p + \pi^- \\ \bar{\Lambda} &\rightarrow \bar{p} + \pi^+ \end{aligned}$$

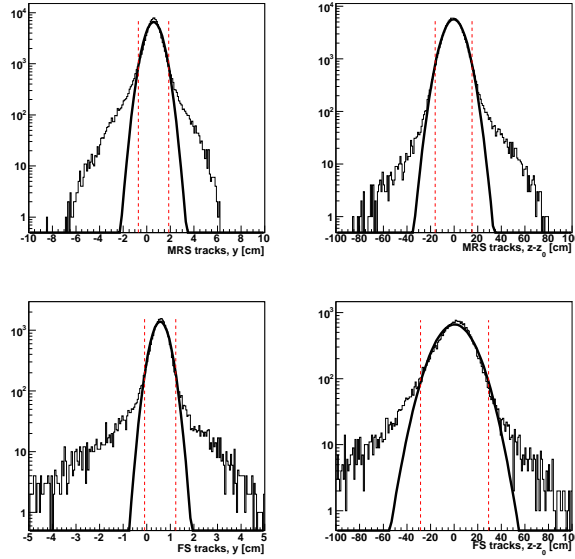


Figure 4.13: Examples of track projections to the $x = 0$ plane, with Gaussian fits and 2σ cuts (red lines). Data are from 60° (top row) and 3° (bottom row).

which occur with a 63.9% branching ratio [79]. The Λ has a lifetime of $c\tau = 7.89$ cm, meaning that most of them will decay before the first BRAHMS detectors. The kinematics of this process is such that the proton will carry most of the original momentum, and we get a pion that flies to one side while the proton continues almost in the direction of the original Λ particle. This in turn means that it will with a large probability fly through our spectrometer and survive the track projection cut, and be reconstructed in our analysis.

To correct for this effect, a GEANT simulation has been performed [131] throwing Λ s and protons through the spectrometer with a realistic thermal distribution, with a Λ/p ratio taken from experimental data. The p spectrum is then reconstructed using the full BRAHMS analysis framework, and the contributions from primary protons and from Λ decays can be separated.

The resulting corrections are shown in figure 4.17. They range from $<25\%$ to 0 over the momentum ranges used for the present analysis. The corrections are applied and discussed further in the fourth paper in chapter 5.

Acceptance corrections

The most significant correction applied to the data is the one for geometrical acceptance, since the BRAHMS spectrometers only cover a small part of the solid angle into which particles are emitted. Correcting for this is a rather involved process, since the acceptance depends on both the spectrometer angle and magnetic field setting, and the particle momentum, angle and species.

To find the correction, a full GEANT simulation of the detector is again used. A large number of particles are thrown in a (y, p_T) interval that is larger than the known edges of the acceptance at a given setting, and the particles are then reconstructed using the same fiducial cuts etc. that are used for the real analysis. The acceptance for a given y and p_T

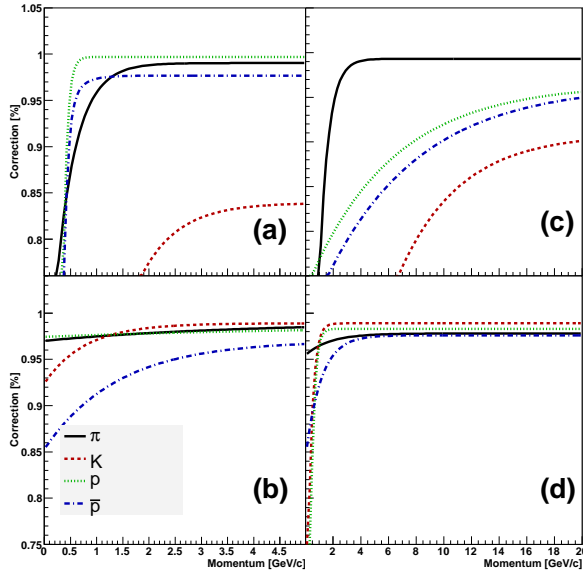


Figure 4.14: Examples of corrections for physical processes: a) Mult. scattering, in-flight weak decays and absorption, excluding the trigger slat, MRS, 60° . b) Effects of the trigger slat, MRS, 60° . c) As (a), for the full FS, 4° . d) As (b), for the full FS, 4° .

is then

$$\mathcal{A}cc(y, p_T) = \frac{\text{accepted particles}(y, p_T)}{\text{thrown particles}(y, p_T)} \cdot \frac{\Delta\phi}{2\pi} \quad (4.16)$$

where $\Delta\phi$ is the azimuthal angle range of the thrown particles. Note that we here assume that on average the distribution of charged particles will be azimuthally symmetric, since the event plane is randomly distributed.

The actual acceptance calculations have been done using the software package **SNac-cPack**, part of the BRAHMS software toolkit that combines GEANT, ROOT and specialized software to quickly produce reusable acceptance maps. This package was written by me for the collaboration as part of my PhD work, and is detailed in appendix D.

Figures 4.18 and 4.19 show examples of acceptance maps in (y, p_T) space for the MRS and FS respectively (60° and 12°), overlaid with experimental data. The correspondence is very good, with only a few single tracks falling outside the simulated acceptance edges. On average, MRS acceptances away from the edges lie around 0.5%, yielding a correction factor of 200, while at 3° the average correction is ~ 30 (3%). This increase comes from the fact that as we move forward in rapidity the same aperture will cover a larger azimuthal angle. This effect is stronger than the fact that the FS physical aperture is smaller than that of the MRS.

Note that the acceptance also varies as a function of the interaction point. This means that the analysis must also be done in narrow interaction point bins, which are then merged in the final analysis (see sec. 4.5). For the present analysis, bins with a width of 10 cm have been used, which is wider than the canonical BRAHMS value of 5 cm. 10 cm was chosen for statistics reasons, as the exact value of this bin width does not have any noticeable effect on the final results. (See discussion of systematic errors below.)

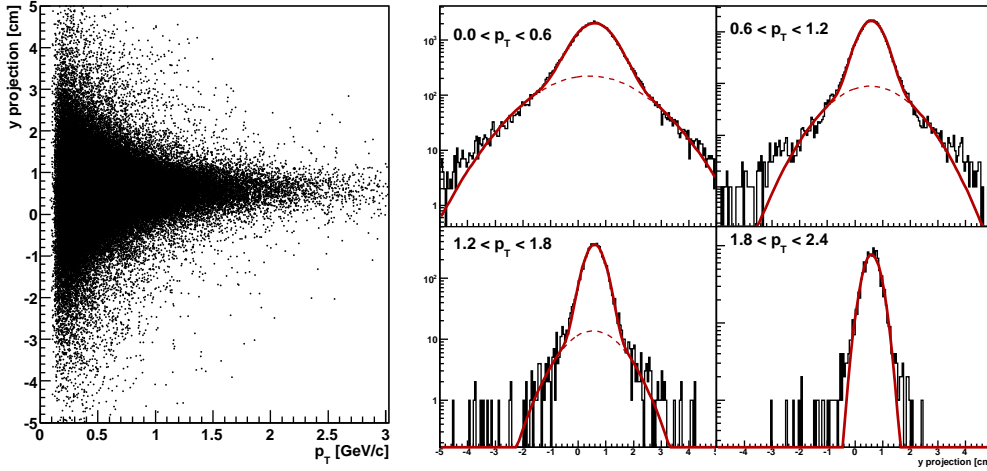


Figure 4.15: Example of background subtraction estimate, for unidentified charged hadrons ($h^+ + h^-$) at 60° . The left panel shows the y track projection coordinate at $x = 0$ as a function of p_T , while the four right-hand panels show projections for four p_T regions. Also shown are double-Gaussian fits and resulting background distributions.

Efficiencies

In practice, we will never be able to identify every charged particle that flies through the spectrometer. Both physical limitations such as gaps in the coverage of hodoscopes, and hardware and software limitations such as the inability to separate two close-lying clusters in a TPC (due both to detector resolution, the cluster deconvolution algorithm and statistical fluctuations in energy deposition), combine to give us a reconstruction efficiency that is less than 100%. To measure the absolute particle yield we must therefore estimate this efficiency for each detector component and reconstruction step.²

Tracking efficiency

The efficiency of TPC tracking in the MRS has been estimated via a track embedding algorithm, where simulated tracks from GEANT were inserted into real events and subsequently reconstructed. Tracking efficiency is defined as

$$\epsilon_{tr} = \frac{N_{reconstructed}}{N_{embedded}} \quad (4.17)$$

and has been studied as function of the TPC occupancy [132].

For the MRS, figure 4.20, left panel, shows the results for the combined efficiency of the two tracking chambers versus the summed number of TPC clusters.

For $p + p$ data, the average number of MRS clusters is $N_{cl} < 100$ per event, so the MRS tracking efficiency can be taken to be $\epsilon_{tr}^{MRS} \approx 94 \pm 1\%$. The results for protons are consistent with the π and K results shown.

For the FS, which has an array of five individual tracking detectors, another algorithm known as the reference track method has been used to estimate the total efficiency. This

²The discussion below closely follows that presented by Djamel Ouerdane and Peter H. L. Christiansen in their PhD works. [24, 23]

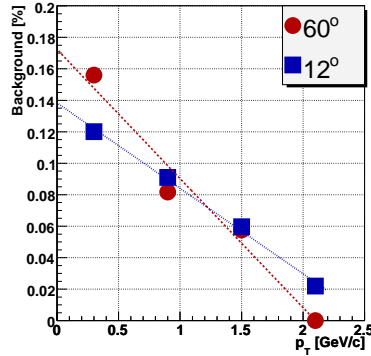


Figure 4.16: p_T -dependent background correction for unidentified charged hadrons, 60° and 12° settings, extracted from double-Gaussian fits as shown in fig. 4.15. Pion corrections are similar in shape and magnitude.

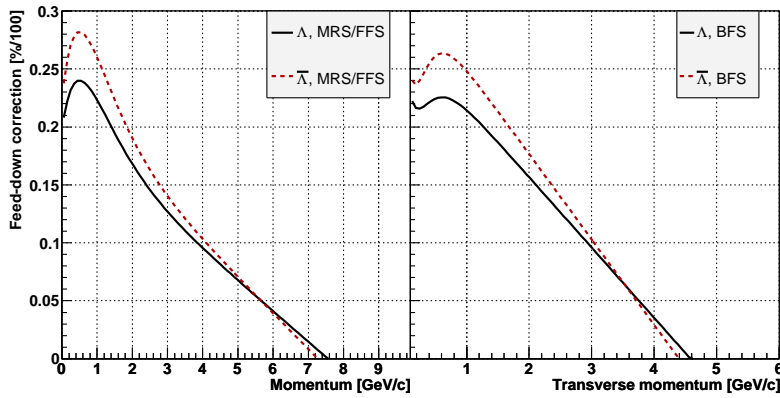


Figure 4.17: Feed-down corrections from Λ (solid lines) and $\bar{\Lambda}$ (dashed lines). Left panel: Correction for the MRS and the FFS, as a function of momentum. Right panel: Correction for the full BFS, as a function of transverse momentum.

method reconstructs a global track based on information from four of the five detectors, and then looks in the fifth detector for a track segment that is consistent with the global track (i.e. fulfills the matching criteria discussed above).

For the datasets in question here, both the drift chambers and the two FFS TPCs worked well for most settings, with some inefficiencies for certain run periods. These have been either excluded from the analysis, or treated specially. The right panel of fig. 4.20 shows two examples of combined FS tracking efficiency vs. momentum. The circles (upper curve) shows the FFS only (T1+T2) at a 12° setting, while the squares show the full FS (T1–T5) for a 4° setting. Data are from the 2001 $p + p$ run. The combined efficiency is calculated as the product of the efficiencies of all detectors that contribute to the track, i.e. in the simplest case

$$\epsilon_{FFS}^{tracking} = \epsilon_{T1} \cdot \epsilon_{T2} \quad (4.18)$$

$$\epsilon_{FS}^{tracking} = \epsilon_{FFS} \cdot \epsilon_{T3} \cdot \epsilon_{T4} \cdot \epsilon_{T5} \quad (4.19)$$

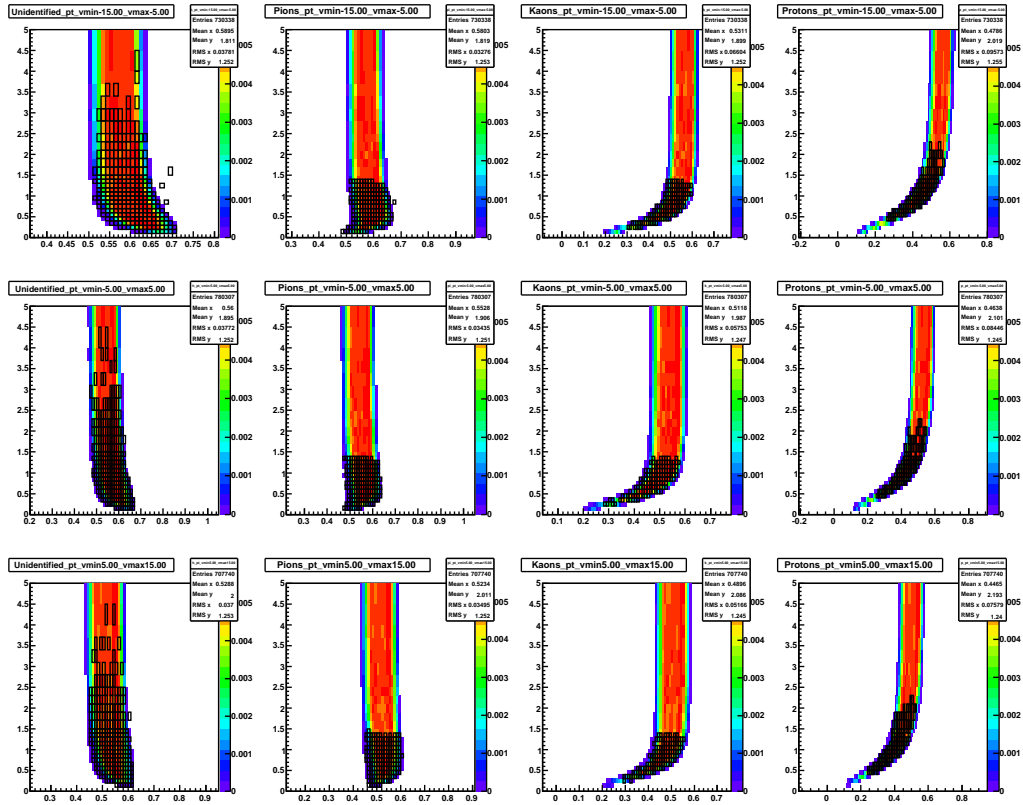


Figure 4.18: Acceptance maps for the MRS at 60° , overlaid with experimental data (boxes). The rows show three different vertex bins, while the columns from left to right show unidentified particles (in pseudorapidity), pions, kaons and protons.

PID efficiency

There is also some inefficiency in the matching of tracks to hits in the time-of-flight systems, and in the ring reconstruction of the RICH detector.

For the TOFW in the MRS, all slats are positioned on a smooth arc. While this design gives a wider coverage for the wall, it also introduces edge effects, e.g. when a particle moves through the wall close to the edge of a slat and thus depositing little energy. The FS hodoscopes have two staggered rows of slats, offset by one slat depth, to reduce this problem.

In order to estimate the overall slat efficiency, including losses from this and other effects, the distribution of hits associated to valid tracks is divided by the distribution of the number of times valid tracks intersect slats. For the 2001 dataset this correction is discussed in more detail in [23]. It is estimated to be $\sim 93\%$ for the part of the TOFW used in the analysis, and this correction is also used for the present analysis. For H1 this analysis has been performed especially for $p + p$ data, since the results presented in [23] have some issues related to high occupancy. Figure 4.21 shows sample efficiency distributions for H1 in 2001 $p + p$ data, as a function of momentum. It is clear that while there are some minor setting-by-setting variations, H1 consistently gives an efficiency $>98\%$ with no momentum dependence. This factor is multiplied into the tracking effi-

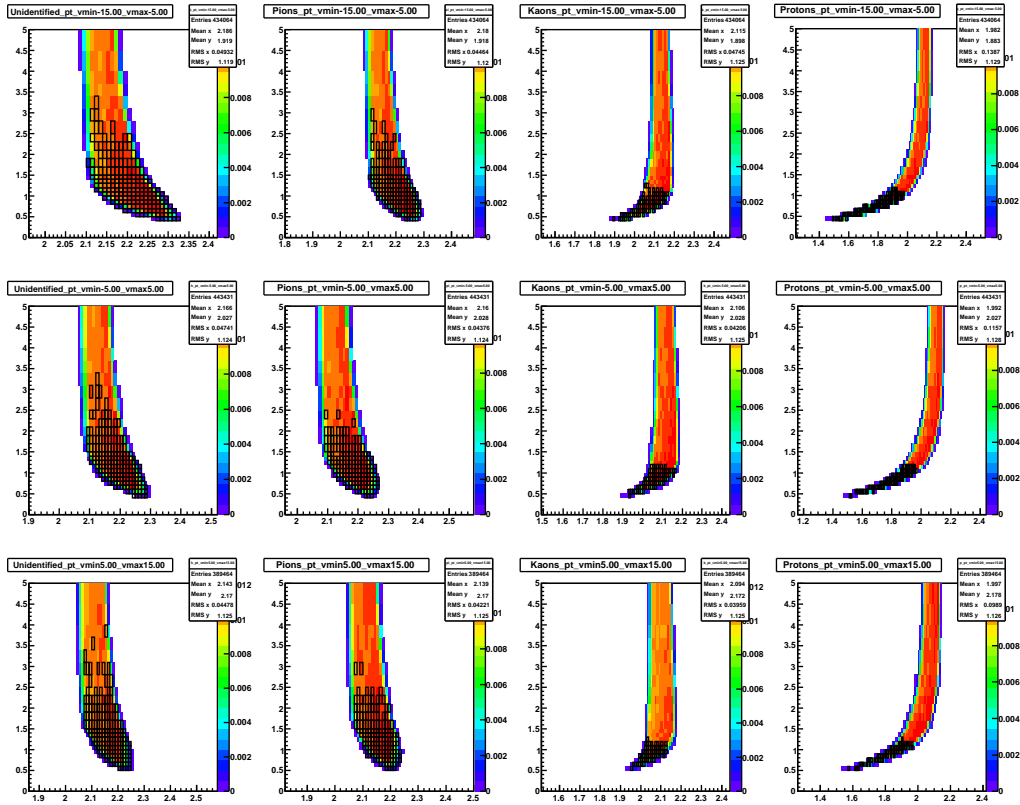


Figure 4.19: Acceptance maps for the FFS at 12° , overlaid with experimental data (boxes). The rows show three different vertex bins, while the columns from left to right show unidentified particles (in pseudorapidity), pions, kaons and protons.

ciency given above where H1 is used for PID. H2 has not been used for this analysis, so no efficiency study has been made.

Note that a correction for multiple hits in the same slat, which can not be separated in a hodoscope, is usually also added at this point. For the present $p + p$ analysis we rarely see more than one track per event, so the effect of this correction is negligible.

For the RICH detector no software tool for full efficiency calculations has been implemented. Instead, the ring reconstruction efficiency can be estimated by looking at pions identified in H2 and seeing if they can be matched to a RICH ring. This procedure will only depend on the particle β and not on its mass, so pion results can be recalculated to the corresponding momentum range at the same β values for other species.

While this procedure will be tainted by pion decays between H2 and RICH and is limited in momentum to the relatively small pion range covered by H2, it does give a sufficiently good approximation of the correction needed. Again, the correction is discussed in more detail in [23], and the resulting efficiency plot is shown in figure 4.22.

The resulting RICH efficiency is quite low close to the threshold value for a given particle species, starting at $\sim 10\%$, but then rises to an approximately constant value of $\sim 93\%$ over an interval of only 1 GeV/c.

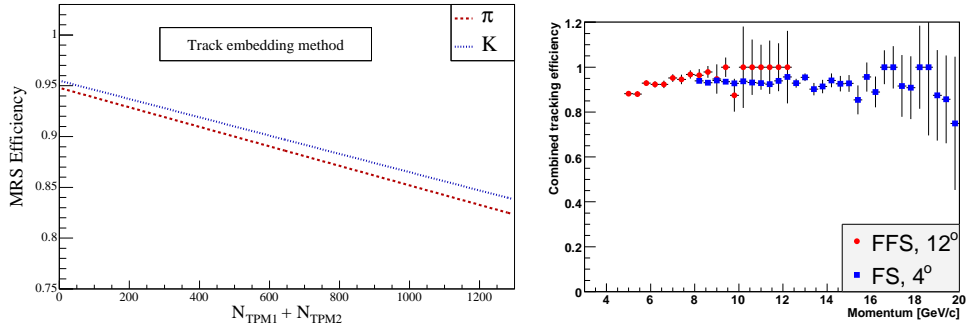


Figure 4.20: Tracking efficiency estimates.

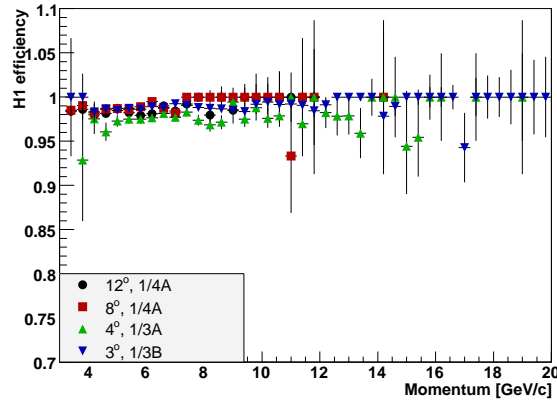


Figure 4.21: Sample efficiency distributions for the H1 hodoscope for 2001 data, as a function of momentum.

RICH contamination

As discussed in section 4.2 above, the identification of (anti-)protons at high rapidities (3° and 4°) is primarily done using the RICH as a veto counter. In [24] it is pointed out and extensively discussed that this indirect method can introduce contamination in the data from the following sources:

- RICH inefficiency. Failure to reconstruct a ring, e.g. from a pion above threshold, would cause this pion to be identified as a proton.
- Absorption and decays. A particle that has a track all the way through the FS but is absorbed or decays between T5 and the RICH will be identified as a proton unless the decay products are identified in the RICH.

The contamination in the proton sample identified by the indirect method has been studied in [24] for Au+Au data in the 2001 dataset using particles identified in H2. In brief, the method used studies the difference $1/\beta - 1/\beta_{proton}$ for particle velocities measured in H2, where β_{proton} is the velocity of a proton with the reconstructed momentum. See figure 4.23. We first plot pions and kaons positively identified in H2 and fit them to single Gaussians centered on the expected value (two leftmost columns), and then do the

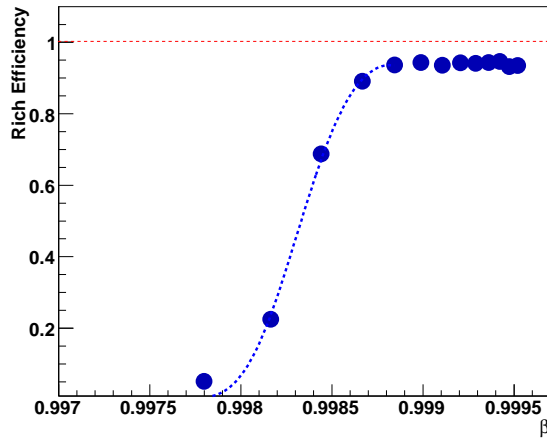


Figure 4.22: RICH efficiency as a function of the particle velocity β , calculated by projecting identified particles from H2 to the RICH plane and looking for a matching light ring. The dashed line is a fit to the data used to interpolate between the histogram bins. Original efficiency data from [23].

same for protons positively identified by rings in the RICH (third column). We now have the positions and widths of the $1/\beta - 1/\beta_{proton}$ distributions for π , K and $p(\bar{p})$. Finally, we plot the same distribution for protons identified via the veto method, and fit it to the sum of the three known Gaussians without fixing their integrals. See the rightmost column of figure 4.23. Integrating and summing the fitted pion and kaon Gaussians we find the relative contamination of these species in the proton sample. For both charge signs, a RICH inefficiency of $\sim 3\%$ is found via this method. (Note: the fact that the curves for positively identified protons in figure 4.23 are not centered on 0 comes from an offset in the time-of-flight calibration used. This does not affect the contamination analysis, since the offset affects all the distributions equally.)

For the present analysis, the sample of positively identified protons is not large enough to repeat the procedure. The results from Au+Au have therefore been used, i.e. the following correction factors:

$$\epsilon_{contam}^p = 9.2\% \quad (4.20)$$

$$\epsilon_{contam}^{\bar{p}} = 33.2\% \quad (4.21)$$

The difference comes from the low anti-proton multiplicity compared to the proton multiplicity, while the pion multiplicity is the same in both settings. As will be shown in the next chapter, the particle composition in $p + p$ at $\sqrt{s} = 200$ GeV is similar enough to Au+Au to warrant the use of the same contamination corrections. Possible errors introduced by this procedure are included in the systematic error discussed in section 4.10.

Multiplicity bias

Finally, any other biases of the event sample must be corrected for. For BRAHMS $p + p$ and $d + Au$ data, the most important such bias comes from the triggering system. As discussed above, GEANT simulations show that the four INEL rings see $71 \pm 5\%$ of the

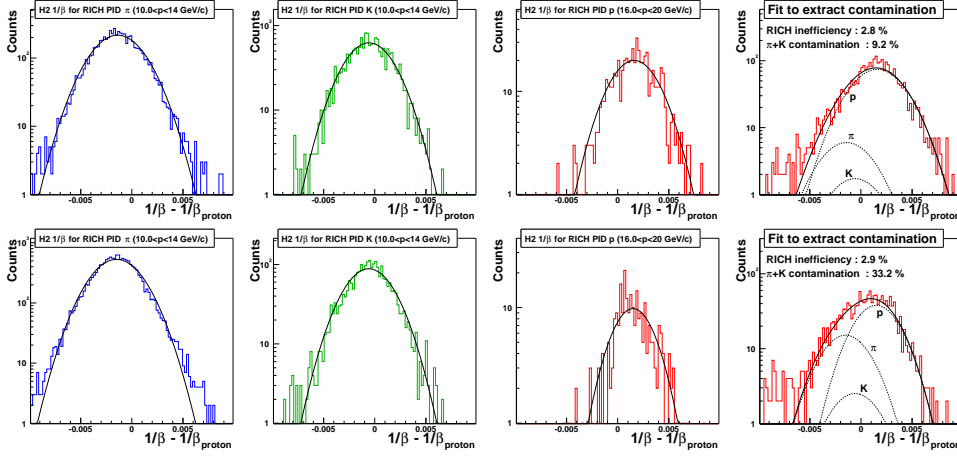


Figure 4.23: Extraction of RHIC contamination. On all plots the abscissa is $1/\beta$ measured by H2, subtracted the expected $1/\beta$ for a proton with the same momentum. Top, two left panels: Pions, and kaons identified by the RICH in the momentum interval, $10 < p < 14$ GeV/c, where proton identification is done by the veto method only. The distribution has been fitted by a Gaussian. Top, third panel: Same for protons identified via rings in the RICH, i.e. for the momentum interval $16 < p < 20$ GeV/c. Rightmost panel: The distribution of protons identified in the RICH by the veto method ($10 < p < 14$ GeV/c) fitted with the sum of the three Gaussians from the first plots, see text. Bottom row: Same for negative particles.

41 mb $p + p$ total inelastic cross-section [133]. Since a trigger is the requirement of a hit in one ring on either side of the interaction point, it is natural that this will bias the sample towards high-multiplicity events. The same simulation showed that the events recorded have on average 13% higher multiplicity than the total non-single-diffractive event sample, and correspondingly the final yield of particles must be corrected by a factor $1/1.13 = 0.885$.

4.5 Total corrections and data set combination

We now have the raw data, and a complete set of corrections for the dataset. To keep track of them all, and to ensure that errors are treated correctly, data and corrections are treated separately all the way until the very final step of the analysis.

Combining the correction plots

At this point the data are contained in $y - p_T$ histograms, one for each vertex bin in each setting. Corresponding histograms are constructed containing all the physics corrections, efficiencies, background subtractions and trigger scaledowns:

$$\begin{aligned}
 Corr|_{p_T, y} &= f_{scaledown} \cdot f_{mult.bias} \cdot f_{matching} \cdot f_{vtx} \cdot \\
 &\quad \epsilon_{tracking}(p) \cdot \epsilon_{PID}(p) \cdot \epsilon_{decay}(p) \cdot \epsilon_{mult.scatt.}(p) \cdot \epsilon_{absorption}(p) \cdot \\
 &\quad \delta_{feeddown}(p) \cdot \delta_{background}(p_T) \cdot \delta_{RICHcontam}
 \end{aligned} \tag{4.22}$$

where all factors are detailed in the discussion above. (Some, like the feiddown correction, are only applied for the relevant particles.) Here, f factors are constants applied to the whole histogram. ε factors are momentum-dependent factors that compensate for loss of particles, while δ factors remove contributions from unwanted tracks. (Note that f_{matching} and f_{vtx} refer to factors compensating for losses due to cuts in track matching parameters and projections to the interaction point respectively, as discussed in section 4.3. All other factors were discussed in the previous section.)

The histograms are then merged with the acceptance maps according to the following equation (see appendix A.4 on page 102 for reasoning and derivation):

$$\text{CORR}|_{v,s,p_T,y} = \frac{\text{CORR}|_{p_T,y}}{2\pi N_{ev}(v) \mathcal{A}CC|_{s,v,p_T,y} \times b_{p_T} \times b_y} \quad (4.23)$$

where subscript s notes the current spectrometer setting, v identifies the vertex bin and $N_{ev}(v)$ the corresponding raw number of events. The factors b_{p_T} and b_y are the bin widths of the histograms. Now, the 2D histogram CORR contains all correction and normalization for vertex bin v .

Merging all settings

For each data set s characterized by a spectrometer angle and a magnetic field, all vertex bins are summed up as follows:

$$\text{DATA}|_{s,p_T,y} = \sum_v \text{DATA}|_{v,s,p_T,y} \quad (4.24)$$

$$(\text{CORR}|_{s,p_T,y})^{-1} = \sum_v (\text{CORR}|_{v,s,p_T,y})^{-1} \quad (4.25)$$

where the sum is running over the vertex bin v . The last term can then be inverted for each (p_T, y) cell, so that the normalized and corrected differential yield for one setting reads

$$dN|_{s,p_T,y} = (\text{DATA}|_{s,p_T,y}) \times (\text{CORR}|_{s,p_T,y}) \quad (4.26)$$

However, to cover as much of the $y - p_T$ plane as possible the 2001 dataset covers several angle and magnetic field settings of the spectrometer. We wish to combine all these settings s into one averaged 2D histogram containing all the normalized data, and this is done according to the same procedure:

$$\langle dN|_{p_T,y} \rangle = \frac{\sum_s dN|_{s,p_T,y} \times W|_{s,p_T,y}}{\sum_s W|_{s,p_T,y}} \quad (4.27)$$

where the weight $W|_{s,p_T,y}$ is defined as

$$W|_{s,p_T,y} = \frac{1}{\text{CORR}|_{s,p_T,y}} \quad (4.28)$$

to ensure that (p_T, y) cells with large corrections (corresponding to a low statistical significance) carry low weights. With these definitions, eq. 4.27 can be rewritten

$$\langle dN|_{p_T,y} \rangle = \left(\sum_s \text{DATA}|_{s,p_T,y} \right) \times \left(\sum_s \frac{1}{\text{CORR}|_{s,p_T,y}} \right)^{-1} \quad (4.29)$$

i.e. a form that conserves the statistical form of $\text{DATA}|_{s,p_T,y}$. Other choices for the weights would not give this factorized form and hence not the straight sum of contributing counts. In this form, weights W 's can be interpreted as an effective number of events. When the resulting yield is zero in a cell, there can be two explanations: either the correction factor is zero, in which case the cell was excluded from the acceptance from the beginning, or there was no particle (data) in the cell. In the latter case, the measurement is still valid (as well as the weight factor) and keeping zero cells is important when cells are averaged over to make projections to the p_T axis. A discussion on the subject can be found in [24], as well as in appendix A.

4.6 Final $d^2N/dydp_T$ maps

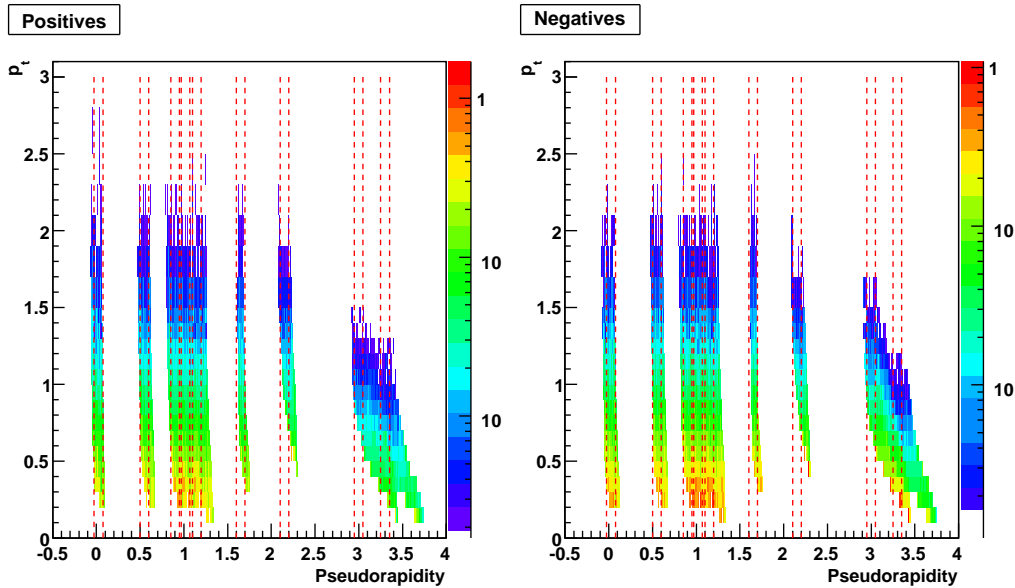


Figure 4.24: Normalized $\eta - p_T$ distribution of the full 2001 $p + p$ dataset, for unidentified charged particles (h^\pm).

Figures 4.24 and 4.25 show the resulting $y - p_T$ distributions for the full 2001 dataset, for unidentified charged hadrons and identified particles respectively. The lines show the areas that will be used later to project spectra onto the p_T axis.

It is clear that while the present dataset does not fully cover the $y - p_T$ plane, enough coverage exists to measure particle production as a function of rapidity up to approximately $y \sim 3$. Note, however, that the p_T ranges covered by the different settings vary significantly and in some instances do not overlap at all. This is an unfortunate feature of the data sample, since when extrapolating the spectra to the total yield we would like to fit them over the same p_T or m_T range.

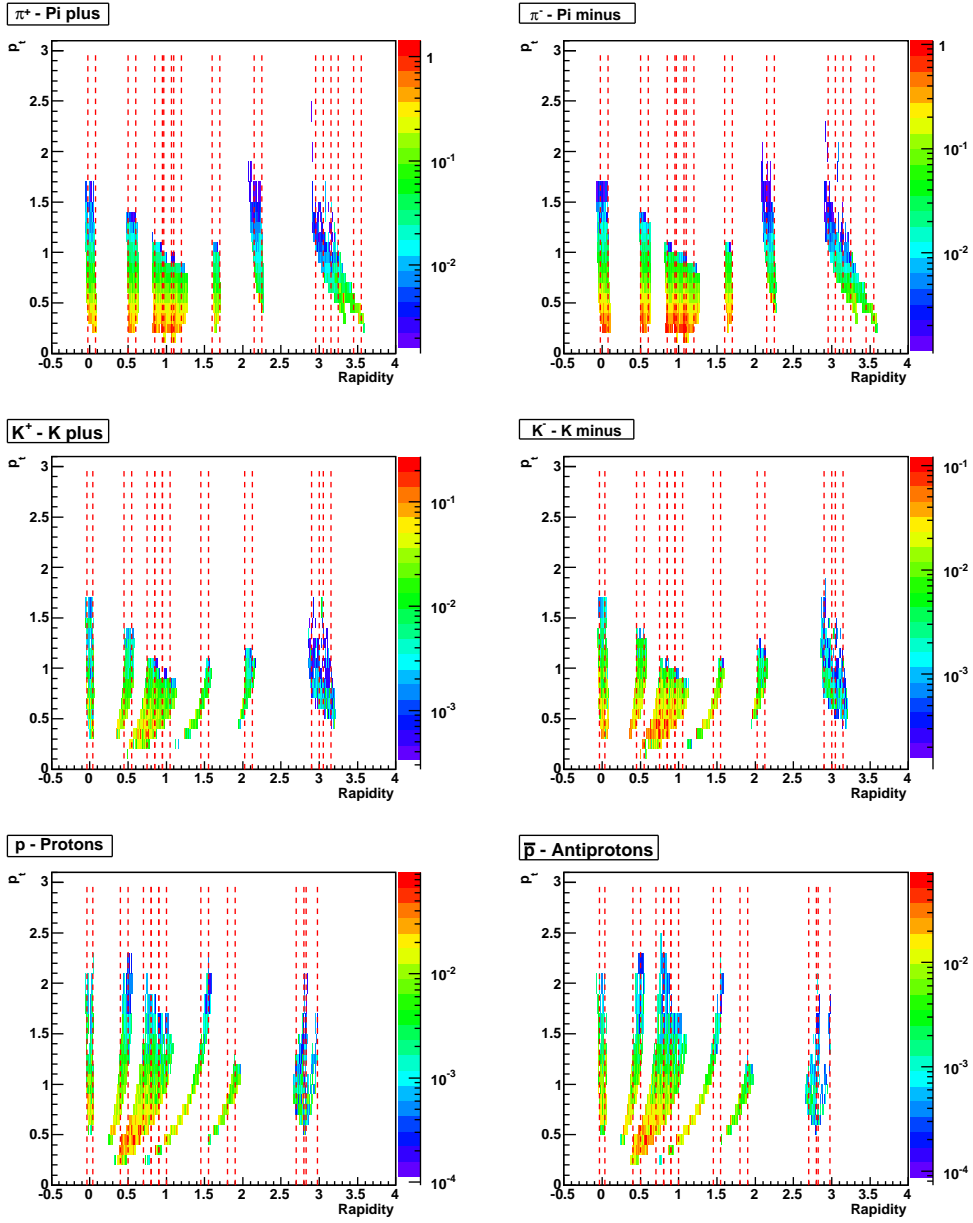


Figure 4.25: Normalized $y - p_T$ distribution of the full 2001 $p + p$ dataset, for π^\pm , K^\pm , p and \bar{p} . Lines represent the edges of projections to the p_T axis that become the normalized spectra.

4.7 Like-particle ratios

The first and simplest analysis one can do with such a dataset is to divide the distributions for particles that are identical except for their charge (π^+ and π^- , K^+ and K^- , p and \bar{p}), to construct the like-particle ratios as a function of p_T and rapidity. In this ratio, all corrections except the \bar{p} absorption cancel out, so for the present dataset this analysis was done before most of the above results were available.

The results of this analysis are presented in the paper *Forward and midrapidity like-particle ratios from p + p collisions at $\sqrt{s} = 200$ GeV*, published in **Phys.Lett.B607:42-50,2005** and reprinted in the next chapter.

Unlike the analysis that is described above, the like-particle ratio analysis uses both positive and negative particles from the MRS for each polarity. While one charge sign is disfavored because of the uneven geometrical acceptance of the TOFW, this does not negatively affect the results since we can write the ratios as

$$\frac{n^-}{n^+} = \sqrt{\frac{n_A^- \cdot n_B^-}{n_A^+ \cdot n_B^+}} \quad (4.30)$$

where n is any particle specie and n_A^- denotes the observed number of negative particles from polarity A etc. Each factor is a function of (y, p_T) , and can be written out as

$$n_{pol}^{ch}(y, p_T) = \frac{N_{pol}^{ch}(y, p_T) \cdot Corr^{ch}(y, p_T)}{\mathcal{A}cc_{pol}^{ch}(y, p_T) \cdot N_{pol}^{events}} \quad (4.31)$$

where ch is the charge sign, pol is the polarity of the MRS magnet and N_{pol}^{ch} is the number of particles actually observed. Since for our spectrometer $\mathcal{A}cc_A^+ = \mathcal{A}cc_B^-$, and similar for opposite charge signs and polarities, eq. 4.30 reduces to

$$\frac{n^-}{n^+} = \sqrt{\frac{N_A^- \cdot N_B^-}{N_A^+ \cdot N_B^+}} \cdot \frac{Corr^-}{Corr^+} \quad (4.32)$$

i.e. both acceptance effects and the dependence on the number of events cancel out, and we are only sensitive to the actual observed number of particles and any difference in physics corrections between a particle and its antiparticle. For pions and kaons, we also have $Corr_A^+ = Corr_B^-$, further simplifying the analysis.

For the FS we only see one charge sign per polarity, so there we still need the normalization to the number of events. The acceptance still cancels out as above.

We do not observe any vertex dependence of the $\frac{n^-}{n^+}(y, p_T)$ factors, but since the acceptance correction is vertex dependent we still perform the analysis in 10 cm vertex bins. The results from different bins are added using a straight average, and projections of the results onto the p_T axis are made using rapidity intervals of $\Delta y \leq 0.1$. The resulting $\frac{n^-}{n^+}(p_T)$ distributions are fitted to extract particle ratios at the various rapidity values, as discussed in the third paper in chapter 5.

4.8 Particle spectra

The next step in the analysis of the absolute particle yields is to project sections of figs 4.24 and 4.25 onto the p_T axis to create spectra. This is done according to the following

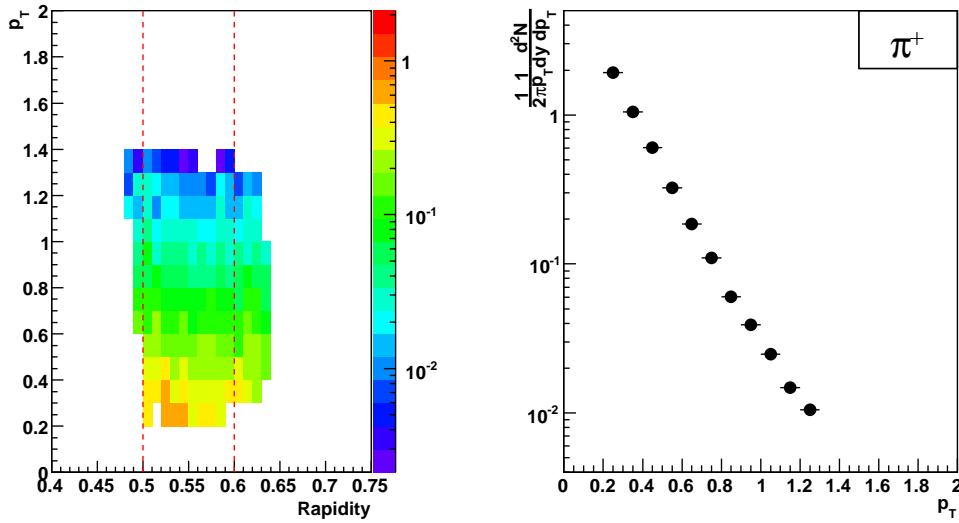


Figure 4.26: Averaged projection of data within interval Δy (between the lines) to the p_T axis. The histogram in the right panel is a normalized particle spectrum.

formula:

$$N(p_T) = \left(\sum_y \sum_s \text{DATA}|_{s,p_T,y} \right) \times \left(\sum_y \sum_s \frac{1}{\text{CORR}|_{s,p_T,y}} \right)^{-1} \quad (4.33)$$

with $y - \Delta y/2 \leq y \leq y + \Delta y/2$. Note that Δy is the sum of the widths of bins within the projected slice that have a nonzero correction value. This way we get the correct normalization to unit rapidity even if a bin within the acceptance has no counts. The full normalized p_T spectrum is then defined as

$$\frac{1}{2\pi p_T} \frac{d^2N}{dp_T dy}(p_T) \equiv \frac{1}{2\pi} \frac{N(p_T)}{p_T \Delta y} \quad (4.34)$$

where p_T in the denominator is the center of the histogram bin. Figure 4.26 shows an example projection and the resulting spectrum. See also app. A.2 for a discussion of the normalization used in eq. 4.34.

The results of this procedure for charged particles, identified and unidentified, are presented in a self contained form in the paper draft *Rapidity dependence of charged particle production from p + p collisions at $\sqrt{s}=200$ GeV*, reprinted in chapter 5. Note however that there I have analyzed the spectra as a function of the transverse mass $m_T \equiv \sqrt{p_T^2 + m^2}$ rather than the transverse momentum. The reason for this is related to the fit function used to extrapolate the spectra, as discussed in the next section.

The same procedure was also used for the 2003 dataset to extract the unidentified hadron spectra presented in the paper *On the evolution of the nuclear modification factors with rapidity and centrality in d + Au collisions at $\sqrt{s} = 200$ GeV*, published in **Phys.Rev.Lett.93:242303,2004** and reprinted in the next chapter.

4.9 Fitting the spectra

To find the total particle production within a given rapidity interval, dN/dy , we need to extrapolate the spectra found in the previous section to cover all values of p_T or m_T . For this, we need to assume a functional form and fit it to the spectra.

Commonly used functions for this analysis are single exponentials in m_T and double exponentials, power laws and Boltzmann distributions in p_T . The physical basis for testing these forms is as follows:

- Single exponential in m_T : Distribution, according to Fermi or Bose statistics, of particles from a thermalized source.
- Double exponential in p_T : The same, but taking into account the possibility that there may be two sources of different temperatures. (This is done because we observe that the spectral slope changes as a function of p_T .)
- Boltzmann distribution p_T : Classical thermal distribution, which is the high temperature limit of the distributions from quantum statistics.
- Power law p_T : Modification of thermal spectra due to collective flow and rescattering.

Once a spectrum is well fitted to such a function, i.e. we can perform a fit with a reasonable value of χ^2/DOF , then the total yield can easily be calculated under the above assumptions. See appendix A.3 for details.

Fit function analysis

For generality, all four functional forms have been attempted fitted to the experimental spectra. See examples of this analysis in figures 4.27, 4.28 and 4.29, where a single spectrum from π^+ , K^+ and p respectively has been fitted.

For individual spectra there is some variation in which functional form gives the best fit. In general, however, the p_T (m_T) coverage of the present dataset is so short that it is hard to distinguish between the forms. The only form that consistently gives good fit results is the single exponential in m_T , so this function has been chosen for all spectra for consistency. The deviation from exponential form that some spectra show is instead included in the systematic error, discussed in the next section.

The exception from this practice is the spectra of unidentified charged hadrons. Here we are not constrained by the particle identification limitations of the experiment, and we also have higher statistics. These spectra can only be well fit to a power law dependence.

The mathematics of integrating the spectra and extracting the total yields and inverse slope parameters is discussed in appendix A.3.

4.10 Systematic errors

The final step of the analysis is the evaluation of any systematic errors introduced by the analysis procedure. Ideally, a detailed Monte Carlo study of the full detector setup and analysis chain would describe these errors, but in practice this is hard to do. Instead, we rely on estimates from the data.

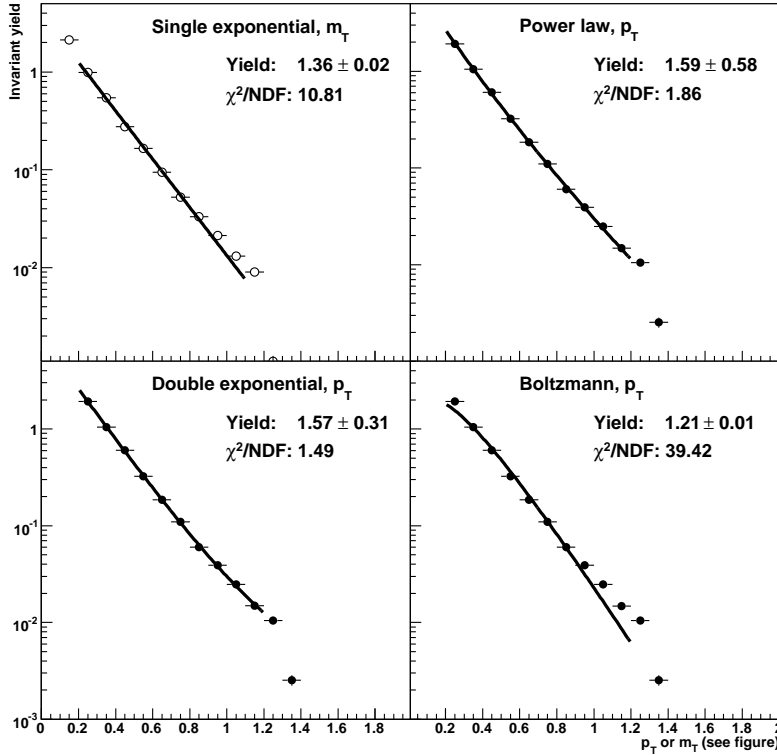


Figure 4.27: Comparison of common fit functions for extrapolation to high and low p_T . Spectrum shown: π^+ at $y \sim 0.5$. Closed symbols: p_T Open symbols: m_T

Following a discussion in [24], point-to-point systematic errors on the integrated yields are divided into two categories that are estimated separately:

- Errors from the fit functions discussed in the previous section, and the subsequent extrapolation to get the integrated yields
- Errors from the rapidity range selected to project onto the p_T/m_T axis

In addition, there may be errors from the overall normalization and corrections that apply equally to all spectra.

Note that the discussion in this section only relates to the analysis total yield analysis presented in the unpublished fourth paper in chapter 5. For systematic error estimates relating to other results, see separate discussions in the first and third papers in chap. 5.

Errors from the fits

To estimate the stability of the fits used to extrapolate the data, one can

- vary the fit range, by moving the end points of the fits by one bin up or down
- vary the m_T bin size
- fit with other functions that could describe the spectra

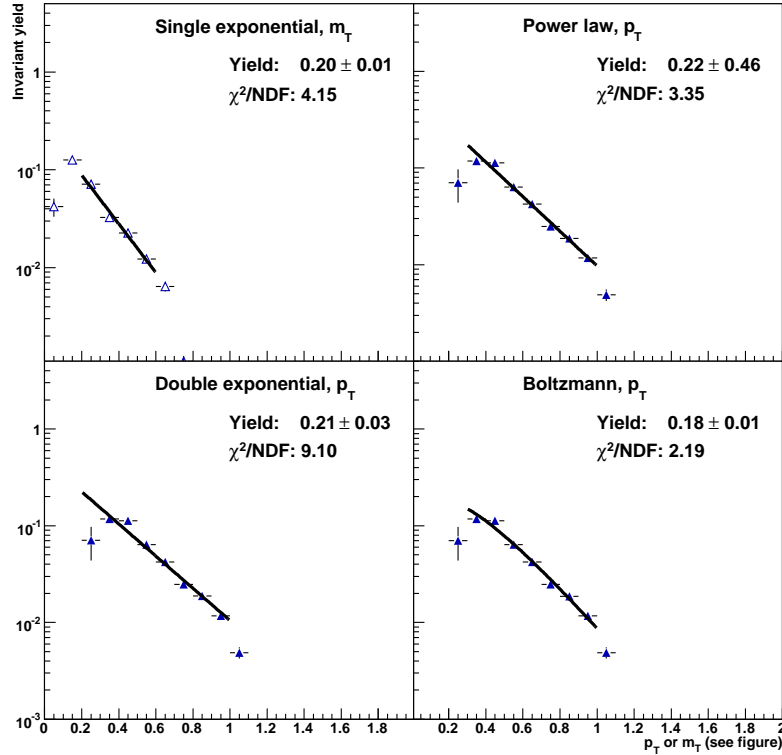


Figure 4.28: Comparison of common fit functions for extrapolation to high and low p_T . Spectrum shown: K^+ at $y \sim 0.8$. Closed symbols: p_T Open symbols: m_T

After evaluating these different contributions, the total systematic error from the fits is calculated as

$$\sigma_{fit} = \sqrt{\sum_i (x - x_i)^2} \quad (4.35)$$

where x_i is the extrapolated yield after variation i and x is the original yield.

For the estimation of errors from different fit functions, I have chosen the one form that on average best fits the spectra except for the single exponential. For the pions and kaons this is the power law dependence in p_T , while for protons it is the Boltzmann distribution in p_T . The selected functions consistently give a $\chi^2/\text{DOF} \sim 2$. (See previous section for a discussion of the functional forms.)

Some 'sanity checks' on the modified yields and the χ^2 value of the fit have been imposed to ensure that the new fits do indeed follow the data. In a few cases where the fit is very sensitive a flat assumption of a 10% uncertainty is used, based on worst-case estimates from neighboring rapidity intervals. Most values lie between 0.2% and 2.0%, with a slight increase towards the more forward angles. This is due mostly to the shorter fit ranges.

Errors from the rapidity projection ranges

To estimate any systematic errors from the rapidity ranges selected for projection onto the p_T/m_T axis (see dashed lines in figures 4.24 and 4.25), the ranges are varied by

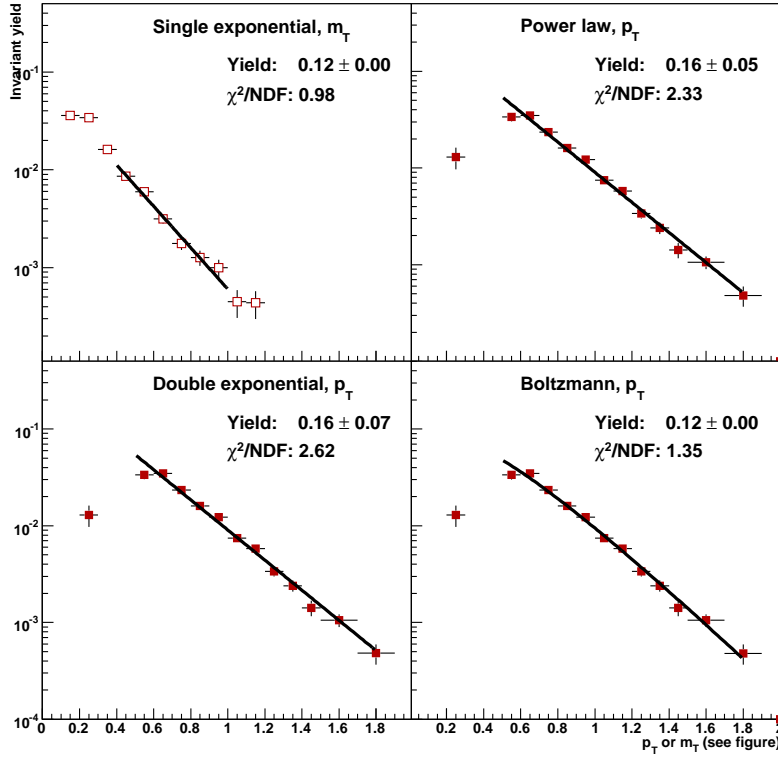


Figure 4.29: Comparison of common fit functions for extrapolation to high and low p_T . Spectrum shown: p at $y \sim 0.8$. Closed symbols: p_T Open symbols: m_T

$\Delta y = 0.02$ (corresponding to two histogram bins in the figures shown). Since most of the acceptances for single settings are quite narrow, the effect of this is to move the edge effects to other parts of the spectrum.

The results of this procedure vary setting by setting between 0.5% and 5%, with no noticeable angle dependence.

Other sources and total systematic errors

Refs. [24] and [23] discuss in detail systematic errors from the combination of different settings covering the same portions of $y - p_T$ space. The present analysis and dataset is such that there is no such overlap, so this source of errors is not relevant here. (Instead we have higher statistical errors.)

Other potential non-negligible sources of systematic errors include

- the tracking efficiency corrections
- corrections for in-flight decay, multiple scattering etc.
- the normalization to $1/N_{events}$
- the width of the vertex bins used in the analysis

y	-0.05	0.55	0.90	1.02	1.15	1.65	2.20	2.93	3.15	3.40	
π^+	5.7	6.2	6.4	6.5	12.2	6.9	9.0	5.0	11.2	9.8	
y	0.03	0.55	0.90	1.02	1.15	1.65	2.20	2.50	2.93	3.10	3.40
π^-	5.2	10.2	5.7	8.2	12.3	8.7	5.6	8.4	5.6	8.5	8.2
y	-0.05	0.50	0.80	0.90	1.00	1.50	2.08	2.95	3.10		
K^+	10.1	9.3	7.6	5.1	5.3	5.1	11.2	11.2	11.2		
y	0.00	0.50	0.80	0.90	1.00	1.50	2.08	2.35	2.95	3.10	
K^-	9.0	8.6	6.8	5.1	5.2	8.6	11.2	11.2	5.0	11.2	
y	-0.02	0.45	0.75	0.85	0.95	1.50	1.90	2.72	2.80		
p	5.5	12.9	8.4	5.0	6.3	6.1	11.2	13.0	10.9		
y	0.00	0.45	0.75	0.85	0.95	1.50	1.90	2.72	2.80		
\bar{p}	5.5	8.0	11.5	9.2	11.2	11.0	11.2	11.2	10.1		

Table 4.3: Combined point-to-point systematic errors from all sources discussed in text. Uncertainty values are given in % of the total yield.

- the estimate of the fraction of the cross section seen, and the multiplicity bias of the triggering system
- for p and \bar{p} at 3 and 4° , the RICH contamination factor

Changing these factors within their respective uncertainties leads to an estimate of an overall systematic error of $\sigma_{other} < 5\%$. This effect is also added into the total systematic error (6% for p and \bar{p} at 3 and 4° due to the last item above).

The combined systematic errors from all sources discussed above are tabulated in table 4.3, where the values are given in % of the total yield at that rapidity. The errors range from 5% to 13%, mostly reflecting the problems getting a stable fit to the spectra. This is in turn linked to the statistics of the data sample taken in 2001. See further discussion in chapters 5 and 6.

Part II

Papers and conclusions

Chapter 5

Brief introduction to the papers

This chapter includes reprints of three published papers, and a preprint of a fourth that is being prepared for publication by the BRAHMS collaboration. In the following I give a very brief introduction to the papers.

5.1 On the evolution of the nuclear modification factors with rapidity and centrality in $d + \text{Au}$ collisions at $\sqrt{s} = 200 \text{ GeV}$

On June 18 2003, all four RHIC experiments gave a common press conference announcing the first publications of $d+\text{Au}$ data at $\sqrt{s} = 200 \text{ GeV}$, compared with $\text{Au}+\text{Au}$ data at the same energy [47, 134, 135, 136]. The main conclusion was clear and unanimous: The high- p_T suppression seen in $\text{Au}+\text{Au}$ collisions (see sec. 1.3) was *not* present in $d+\text{Au}$ at midrapidity, presenting a strong case for the presence of a dense medium with a high degree of gluonic bremsstrahlung in central $\text{Au}+\text{Au}$ collisions. BRAHMS also showed in our publication [47] that the suppression in $\text{Au}+\text{Au}$ was present also at pseudorapidity $\eta \sim 2.2$, indicating that the dense medium indeed extended over several units of rapidity.

The obvious question posed by this is how the $d+\text{Au}$ system behaves at higher rapidities. This was first addressed in the first of the four papers in this chapter, where we show nuclear modification factors R_{dAu} over three units of rapidity. Its main, and unexpected, conclusion is that while there is no suppression at midrapidity in $d+\text{Au}$ collisions, there is a gradual transition to a suppressed state as the rapidity increases. One possible interpretation of this observation is that the incoming gold nucleus may be in a state known as a Color Glass Condensate (see sec. 1.3 and later in this introduction), which then also becomes the initial state for $\text{Au}+\text{Au}$ collisions at $\sqrt{s} = 200 \text{ GeV}$. Other mechanisms for suppression of low- x partons in the Au nucleus, e.g. nuclear shadowing, have also been proposed. This has spawned a lot of discussion and theoretical work, see e.g. [59, 137, 138, 139] (selection of more than 90 citations of this paper to date).

This publication is based on the $d+\text{Au}$ and $p + p$ datasets collected during the 2003 RHIC run. As an early part of my PhD work I participated in the analysis leading up to these results, performing one of several parallel analyses used for consistency checking. I made calibrations and performed most of the data reduction for both datasets, and I also participated in writing the paper itself though I am not the corresponding author.

5.2 The rapidity and centrality dependence of nuclear modification factors at RHIC: What does bulk particle production tell us about the nuclear medium?

After publication of the first paper, I was invited to give a talk on these topics at the 42nd International Winter Meeting on Nuclear Physics, Bormio, Italy, in 2004. The second paper is the proceeding from this talk, containing a detailed discussion of nuclear modification factors measured by BRAHMS. Some results from the first paper are repeated, and compared with other BRAHMS results for completeness.

The rapidity dependence of the R_{dAu} factors is discussed in terms of both the Color Glass Condensate (CGC) picture, and nuclear shadowing. In brief, the CGC is a state hypothesized on the basis of observation in deep inelastic scattering at HERA (see ref. [16] of the second paper and figure 1.4 on page 7). It was seen that as the momentum transfer between the incoming lepton and the struck hadron increases, the observed gluon density function

appears to diverge at small values of x_F . This means that there is a high density of so-called 'wee gluons' carrying a very small fraction of the nucleon momentum, and due to the finite size of the nucleon one must assume that at some point these gluons will start to fuse due to self interaction (see schematic illustration in figure 5.1). This fused state can be seen to take on the properties of a condensate, and to evolve on timescales that are long compared to the duration of a typical heavy ion interaction. Interestingly, such a state seems also to be treatable within the framework of classical field theory, providing an analytical window on the complex initial state of ultrarelativistic heavy ion interactions. For an recent, excellent review of the properties of the CGC, see ref. [140]. Nuclear shadowing, on the other hand, is a depletion of low- x_F partons in nuclear systems, due to a destructive interference reducing the probability of interactions with partons at the back of an incoming nucleus. This effect is also able to describe the data in the first two papers, see e.g. [141].

Also, the importance of proper $p + p$ reference data for the interpretation of interactions involving nuclei is stressed. This becomes one of the motivations for the detailed study of $p + p$ collisions at $\sqrt{s} = 200$ GeV presented in the next two papers.

5.3 Forward and midrapidity like-particle ratios from $p + p$ collisions at $\sqrt{s} = 200$ GeV

This is the first paper discussing in detail the $p + p$ dataset taken during the 2001 RHIC run. The set was intended as a so-called 'soft survey', meaning that we attempted in the time available to cover as much of the $y-p_T$ plane within our acceptance as possible.

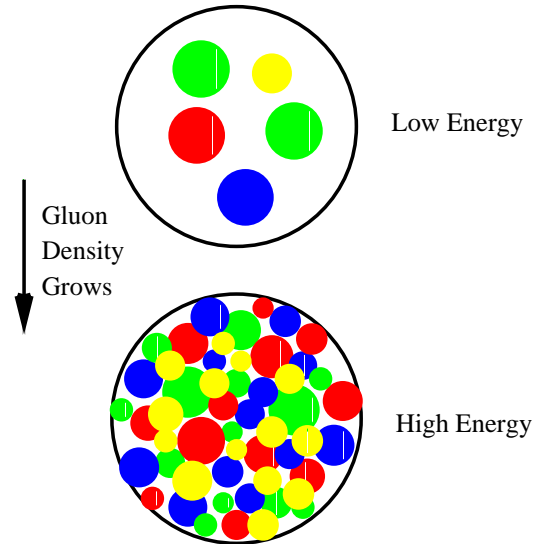


Figure 5.1: Saturation of 'wee partons' as the energy increases. Figure from [140].

This means that while there are a considerable number of different measurements, none have high enough statistics to extend into the so-called high- p_T region. What we get from this set is a survey of the bulk particle production, which comes mainly from soft processes.

This paper discusses the first observable for identified particles one can make from such a dataset, the like-particle ratios. This is a relatively easy measurement since all geometrical acceptances and most systematic effects and other corrections cancel out. We show the ratios as function of rapidity, and note that there is no transverse momentum dependence within our acceptance. Energy systematics, system size comparisons and model calculations are presented, and we note the effect of charge and isospin conservation at the highest rapidities.

For this publication I have both performed the data reduction and analysis, in collaboration with Kris Hagel at Texas A&M University, and authored the paper. To date, the paper has been cited 5 times, most recently in a theoretical study of parton distributions and pion production at RHIC energies [142].

5.4 Rapidity dependence of charged particle production from $p + p$ collisions at $\sqrt{s} = 200$ GeV (in preparation)

The final paper presents normalized charged particle m_T spectra and average total multiplicities from $p + p$ collisions at $\sqrt{s} = 200$ GeV. It is an extension of the analysis performed in the previous paper, with corrections for geometrical acceptance and other effects applied. The analysis leading up to this paper has been presented in detail in chapter 4 of this thesis. Many connected results such as the degree of nuclear stopping, the excitation functions of average multiplicities and unlike particle ratios are given, as are charged hadron spectra versus p_T for use in nuclear modification factors up to $p_T \approx 4.5$ GeV/c. For an extended discussion of the estimate of baryon stopping per incident nucleon, see appendix C.

This paper represents the last part of my PhD work, and the analysis has been performed solely by me. It is not yet submitted for publication, but has been written up and presented for internal review in the BRAHMS collaboration. Its present state is such that all physics results are ready and presented, but not all have been thoroughly discussed and interpreted. The final version of the paper will probably discuss a slightly reduced number of topics, but in greater detail, and may include data from the high-statistics $p + p$ sample taken by BRAHMS in 2005. As mentioned above, this dataset is mainly a survey and as such is not suited for precision measurements at individual rapidities. This is especially true for measurements at the most forward angles covered, where both statistical and systematic errors are presently large. The addition of the 2005 dataset would improve the overall quality of the results, especially in this crucial region close to the beam rapidity, but it should not significantly alter the overall conclusions drawn in the present thesis.

Chapter 6

Conclusions and outlook

The main results of this thesis were presented in the papers reprinted in the previous chapter. Here I will only reiterate some of the main physics conclusions, and take a brief look towards the future.

6.1 Conclusions

This thesis has discussed various aspects of charged particle production in hadronic interactions at $\sqrt{s} = 200$ GeV, either directly from or related to $p + p$ collisions. All data presented were taken with the BRAHMS spectrometer at RHIC during the running periods of 2001 and 2003, which in addition to $p + p$ included Au+Au and d +Au collisions.

The main relation of $p + p$ collisions to larger systems is through the nuclear modification factor, e.g. the factor

$$R_{dAu} = \frac{d^2 N^{dAu} / dp_T d\eta}{\langle N_{coll} \rangle d^2 N^{NN} / dp_T d\eta}. \quad (6.1)$$

which was discussed at length in the first two papers of chapter 5 and also in the fourth. At RHIC energies a suppression of high- p_T particle production in central Au+Au collisions has been well documented, and BRAHMS has shown that this suppression extends at least up to $\eta \sim 3$. It has also been seen that in a d +Au collision there is no such suppression at midrapidity, leading to the picture of a hot and dense fireball in Au+Au events that slows the high- p_T particles through gluon bremsstrahlung.

In this thesis, I have shown R_{AA} factors from central Au+Au collisions for identified pions, kaons and protons, using BRAHMS' published spectra from Au+Au and my own results from $p + p$. The main conclusions are that while the pions follow the trend seen for all charged hadrons, kaons are systematically less suppressed. The protons have a steeper slope with transverse momentum, and reach the $R_{AA} = 1$ line, indicating no suppression, at $p_T \sim 1.5$ GeV/c. I have also shown that there is no rapidity dependence of these results, up to $y \sim 3$. From this we can conclude that whatever the nature of the emitting source in a central Au+Au collision, it seems to extend at least three units of rapidity out from $y = 0$. This is supportive of a picture of the fireball as a hot and dense, longitudinally extended region of medium that suppresses high- p_T particles, i.e. has large gluonic bremsstrahlung. Note, however, that other explanations such as the

effects of nuclear shadowing or low- x parton saturation in the initial state have not been ruled out and continue to be investigated.

For d +Au collisions I have shown that while BRAHMS measures an enhancement of the R_{dA} factor at midrapidity, there is a gradual transition to a suppressed state at $\eta \sim 3$. A possible interpretation of this unexpected result is that the initial state of an incoming gold nucleus at this energy is the color glass condensate. An alternative explanation may be strong nuclear shadowing. This topic is still much discussed in the field, and will probably not be resolved until similar measurements at forward rapidities at LHC energies are made (see the next section).

The main analysis documented in this thesis and presented in the third and fourth papers of chapter 5 relates directly to the $p + p$ collisions themselves. Charged like-particle ratios at $\sqrt{s} = 200$ GeV have been shown to be quite similar to those from central Au+Au collisions, while the deviations hint at interesting physics. At high rapidity, i.e. $y > 2$, the π^-/π^+ ratio decreases from unity, showing the effects of charge and isospin conservation in this region. The ratios show a limiting fragmentation-like behavior, and we see already here that the \bar{p}/p ratio at $y = 0$ is higher than in Au+Au, indicating a lesser degree of nuclear stopping in $p + p$.

These results are borne out in the full analysis of identified charged particle production, where we observe that the limits we can put on nuclear stopping, or average rapidity loss, in $p + p$ at $\sqrt{s} = 200$ GeV are about one unit of rapidity lower than in Au+Au. This leads to the conclusion that the underlying processes that lead to energy loss for particle production in $p + p$ and Au+Au collisions are not quite equivalent at these energies. While differences between such systems are of course expected, they should be kept in mind when making comparisons such as nuclear modification factors.

Finally, we note from comparisons with midrapidity data from both higher and lower energies that both the K/π and \bar{p}/π ratios seem to rise abruptly from one approximately constant level to another between SPS and RHIC energies. We can not identify the actual shape of this transition, but it is highly likely that it is non-smooth and quite abrupt. More $p + p$ data runs at RHIC at lower energies are needed to fill this gap.

6.2 Outlook

What is next for the subjects touched upon in this thesis? For $p + p$ collisions at $\sqrt{s} = 200$ GeV, what has been presented here is the first dataset taken by BRAHMS in 2001. The set was meant to be a 'soft survey', giving an overall view of the global characteristics throughout the $y - p_T$ diagram. This has been achieved, but not with high accuracy and good statistics. Several later $p + p$ datasets exist and are currently being analyzed, that contain high statistics data samples at some of the more interesting regions highlighted by the present analysis — both the midrapidity region for comparisons with other systems to high transverse momenta, and the forward region for fragmentation region physics, nuclear stopping studies and the question of the Color Glass Condensate. Analysis of these sets should be finalized over the coming years, and combined with the present survey results for a thorough understanding of particle production in $p + p$ collisions at $\sqrt{s} = 200$ GeV.

In parallel with this analysis, work continues on understanding Au+Au and d +Au collisions, and lately also collisions of copper on copper (Cu+Cu), i.e. a system of inter-

mediate size. Comparisons of these widely varying systems should yield much information on the requirements for the hot and dense medium discovered in Au+Au collisions to be produced, and the tool of choice for such comparisons are the nuclear modification factors. All such factors should be made with RHIC $p + p$ measurements as their baseline, and the global differences between the systems as found from the work just outlined should be kept closely in mind when making interpretations.

While $\sqrt{s} = 200$ GeV is the top RHIC energy for Au+Au, the accelerator is capable both of colliding nuclei at lower energies, and indeed to reach $\sqrt{s_{NN}} = 500$ GeV for $p + p$ collisions. Au+Au collisions at $\sqrt{s_{NN}} = 63$ GeV have already been recorded, and $p + p$ reference data at this energy should ideally be taken. Such a run has been proposed as part of the 2006 RHIC running, and BRAHMS is at present getting ready to record this dataset.

On to the LHC

The next step after RHIC is the LHC, where the ALICE experiment is being built for heavy ion studies. The LHC, which will likely begin operations in 2007, will be able to collide Pb+Pb up to $\sqrt{s_{NN}} = 6300$ GeV and $p + p$ up to an unprecedented $\sqrt{s} = 14$ TeV. The Alice Physics Performance Report [143] discusses $p + p$ physics in this new energy regime, both as a reference for nucleus–nucleus interactions, and as a physics topic in its own right. Subjects that receive special mention include mechanisms for baryon number transport, strangeness and heavy flavor production, jet studies, the excitation functions of particle multiplicities and even double–parton collisions.

It is clear that the study of $p + p$ collisions and their comparison to interactions of larger nuclei are, and will continue to be, a fruitful part of the study of the strong nuclear force. This thesis has added some more pieces to the puzzle, and both RHIC and the LHC will keep on adding more in the years to come.

Part III
Appendices

Appendix A

Kinematics and mathematics

Some mathematical definitions and calculations employed in the text will be briefly reviewed here.

A.1 Kinematic formulas

Center-of-mass energy

Consider a general $2 \rightarrow 2$ interaction as shown in figure A.1, with incoming four-momenta $p_1 = (E_1, \mathbf{p}_1)$, $p_2 = (E_2, \mathbf{p}_2)$ and outgoing momenta $p_3 = (E_3, \mathbf{p}_3)$, $p_4 = (E_4, \mathbf{p}_4)$. Each has an energy $E_i = \sqrt{m_i^2 + \mathbf{p}_i^2}$ where m_i is the rest mass (using $c \equiv 1$). The Lorentz-invariant total energy, conserved in this reaction, is given by the Mandelstam variable s :

$$\begin{aligned} s &= (p_1 + p_2)^2 = (p_3 + p_4)^2 \\ &= m_1^2 + 2E_1E_2 - 2\mathbf{p}_1 \cdot \mathbf{p}_2 + m_2^2 \end{aligned} \quad (\text{A.1})$$

The center-of-mass energy \sqrt{s} used throughout this thesis is thus

$$\sqrt{s} = \sqrt{(p_1 + p_2)^2} \quad (\text{A.2})$$

For A+A collisions it is usually denoted $\sqrt{s_{NN}}$, which means the center-of-mass energy per nucleon pair.

Coordinates and rapidity

The coordinate system used by BRAHMS, and indeed by most high energy experiments, is defined in figure A.2, with the beams coming in along the z axis and colliding at $x = y = z = 0$.

The rapidity variable is defined as

$$y = \frac{1}{2} \ln \left(\frac{E + p_z}{E - p_z} \right) \quad (\text{A.3})$$

where p_z denotes the momentum component along the z axis. Under a relativistic boost in the z -direction to a frame with velocity β' , y transforms as $y \rightarrow y - \tanh^{-1} \beta'$. From this we can deduce that the shape of the rapidity distribution dN/dy of produced particles

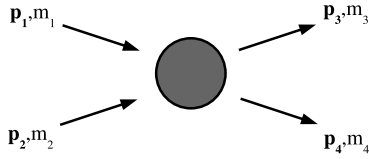


Figure A.1: A generic 2→2 reaction.

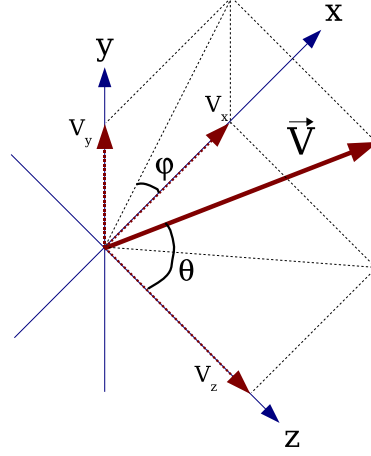


Figure A.2: Coordinate system, as used in this thesis.

form a collision is invariant. This also gives the useful relation $y = \tanh^{-1} \beta$, and from $\gamma = (1 - \beta^2)^{-1/2}$ we can deduce $y = \cosh^{-1} \gamma$.

For $p \gg m$ the definition of rapidity can be expanded to obtain

$$\begin{aligned} y &= \frac{1}{2} \ln \left(\frac{\sin^2(\theta/2) + m^2/4p^2 + \dots}{\cos^2(\theta/2) + m^2/4p^2 + \dots} \right) \\ &\approx -\ln [\tan(\theta/2)] \equiv \eta \end{aligned} \quad (\text{A.4})$$

where $\cos(\theta) = p_z/p$. The last relation defines the pseudorapidity η , used e.g. for unidentified hadrons.

Another measure that is often used in place of rapidity is the so-called Feynman- x variable, defined as

$$x_F \equiv p_L / p_L^{max} \quad (\text{A.5})$$

Here p_L is the longitudinal momentum of the particle, and p_L^{max} is the maximum value that this momentum can have for the given reaction. For a $p + p$ collision in the center-of-mass system, as studied in this thesis, p_L^{max} is equal to the momentum of the incoming target or projectile proton.

A.2 Invariant cross section and transverse momentum

The quantity $E \frac{d^3\sigma}{dp^3}$, where σ is the total interaction cross section, is an invariant under Lorentz transformations. Introducing the coordinate system of figure A.2 and assuming that on average collisions are symmetric about the z axis (i.e. the angle ϕ), we can re-express this invariant as the differential number of particles per event:

$$E \frac{d^3\sigma}{\sigma dp^3} = \frac{1}{2\pi} \frac{1}{p_T} \frac{d^2N}{dy dp_T} \quad (\text{A.6})$$

where $p_T = p \cdot \sin(\theta)$ is the *transverse momentum*. The $1/2\pi$ factor comes from integrating over ϕ . We have also divided each side by the total cross section to get a dimensionless measure of the number of particles.

We can also define the *transverse mass* of an identified particle with mass m , through

$$m_T = \sqrt{p_T^2 + m^2} \quad (\text{A.7})$$

Inserting this into equation A.6 and transforming the differential, we find that we can also express the invariant cross section as

$$E \frac{d^3\sigma}{\sigma dp^3} = \frac{1}{2\pi} \frac{1}{m_T} \frac{d^2N}{dy dm_T} \quad (\text{A.8})$$

i.e. identical in form to the p_T expression. Throughout this thesis, these two forms are used as coordinates on the ordinate of particle spectra plots.

From the transverse mass and the formulas for the rapidity above, we can also deduce the relations

$$E = m_T \cosh y \quad (\text{A.9})$$

$$p_z = m_T \sinh y \quad (\text{A.10})$$

A.3 Fit functions

To extrapolate the p_T and m_T spectra discussed in chapters 5 and 6, they have been fitted with one of the following functional forms:

$$\text{Exponential in } m_T : A \exp \left[-\frac{(m_T - m)}{T} \right]$$

$$\text{Power law in } p_T : B \left(1 + \frac{p_T}{p_0} \right)^{-n}$$

The T parameter of the exponential is called the *inverse slope parameter* and is identified as the apparent temperature of the particle source. This terminology originates from statistical physics, where distribution functions are given by the Fermi or Bose statistics (quantum case) or Boltzmann statistics (classical case, high temperature limit of the quantum distributions). The coefficients A and B are normalization factors that can be related to the integrated yield at rapidity y . For example, the coefficient A is obtained as follows:

$$\begin{aligned} \frac{dN}{dy} &= \int_m^\infty 2\pi m_T A \exp \left[-\frac{(m_T - m)}{T} \right] dm_T \\ &= 2\pi A \int_m^\infty m_T \exp \left[-\frac{(m_T - m)}{T} \right] dm_T \\ &= 2\pi A \left\{ -T m_T \exp \left[-\frac{(m_T - m)}{T} \right] \right\}_m^\infty + 2\pi A T \int_m^\infty \exp \left[-\frac{(m_T - m)}{T} \right] \\ &= 2\pi A T m + 2\pi A T \left\{ -T \exp \left[-\frac{(m_T - m)}{T} \right] \right\}_m^\infty \\ &= 2\pi A T (m + T), \text{ so that} \\ A &= \frac{dN/dy}{2\pi T (m + T)} \end{aligned}$$

For the power law, B is obtained through

$$\begin{aligned}
 \frac{dN}{dy} &= \int_0^\infty 2\pi p_T B \left(1 + \frac{p_T}{p_0}\right)^{-n} dp_T \\
 &= 2\pi B \int_0^\infty p_T \left(1 + \frac{p_T}{p_0}\right)^{-n} dp_T \\
 &= 2\pi B \left[\frac{p_0 p_T}{1-n} \left(1 + \frac{p_T}{p_0}\right)^{1-n} \right]_0^\infty - 2\pi B \int_0^\infty \frac{p_0}{1-n} \left(1 + \frac{p_T}{p_0}\right)^{1-n} dp_T \\
 &= 0 \text{ (if } n > 1) - 2\pi B p_0 \left[\frac{p_0}{(1-n)(2-n)} \left(1 + \frac{p_T}{p_0}\right)^{2-n} \right]_0^\infty \\
 &= \frac{2\pi B p_0^2}{(1-n)(2-n)}, \text{ if } n > 2, \text{ so that} \\
 B &= \frac{(n-1)(n-2)}{2\pi p_0^2} \frac{dN}{dy}
 \end{aligned}$$

The power n has to fulfill the condition $n > 2$. Experimentally, fits to unidentified charged hadron spectra in this thesis give $n \gtrsim 20$.

A.4 Merging vertex bins and settings

When averaging histogram cells in the $1/N \cdot 1/p_T \cdot d^2N/dydp_T$ distributions to combine different vertex bins and settings, as described in section 4.5, and also to project spectra onto the p_T axis as done in sec. 4.8, a problem occurs for bins with no counts. If there are counts, we have an error (\sqrt{n}) and can use the error as weight in a weighted average calculation, but for our purposes we also want to include the empty data bins with a non-zero correction factor. The following is a brief discussion on how to do this properly, following a derivation outlined in ref. [24].

The information we have available consists of measurements for $p_i = n_i/N_i \cdot \varepsilon_i$ where

- p_i is the ‘‘probability’’ in one event for observing one particle in the cell i (i.e. $1/N \cdot 1/p_T \cdot d^2N/dydp_T$). This is the value we must determine.
- N_i is the he number of events accepted in an event sample.
- ε_i is the overall acceptance, efficiency, $1/p_T$, etc., i.e. all correction factors.
- n_i is the actual measured number of particles in the cell.

We want to determine the best possible estimate for p_i and the error, \hat{p} and $\sigma_{\hat{p}}$. The cell count n_i can be assumed to be Poisson distributed:

$$P(n_i) = \frac{\mu_i^{n_i}}{n_i!} \exp(-\mu_i) \quad (\text{A.11})$$

where $\mu_i = N_i \cdot \varepsilon_i \cdot p$.

Using the maximum likelihood method we can construct the likelihood function:

$$L(p) = \prod_i P(n_i) = \prod_i \frac{\mu_i^{n_i}}{n_i!} \exp(-\mu_i) \quad (\text{A.12})$$

To find \hat{p} we take the logarithm

$$\begin{aligned} \log L(p) &= \sum_i n_i \log \mu_i - \log n_i! - \mu_i \\ &= \sum_i n_i \log N_i \epsilon_i + n_i \log p - \log n_i! - N_i \epsilon_i p \end{aligned} \quad (\text{A.13})$$

and differentiating with respect to p

$$\begin{aligned} \frac{d \log L(p)}{dp} &= \sum_i \frac{n_i}{p} - N_i \epsilon_i = 0 \Rightarrow \\ \hat{p} &= \frac{\sum_i n_i}{\sum_i N_i \epsilon_i} \end{aligned} \quad (\text{A.14})$$

This expression has a simple interpretation. The numerator is the total number of measured particles and the denominator is the total number of tries scaled for efficiency etc.

For a large event sample we can assume that the statistical error purely comes from the numerator, and so the relative error on the calculated probability is just the relative error on the numerator:

$$\sigma_{\hat{p}} = \frac{\hat{p}}{\sqrt{\sum_i n_i}} \quad (\text{A.15})$$

This is the relation that is used for the merging equations in sections 4.5 and 4.8. Note that the appendices of ref. [24] includes a Monte Carlo simulation that shows the validity of the above assumptions and estimates.

Appendix B

BRAHMS spectrometer resolution

The precision with which we can determine the track momentum and trajectory is limited by factors such as the intrinsic angular resolution of the spectrometer and multiple Coulomb scattering experienced by the particles. This determines the quality and range of our particle identification capabilities, and it affects the shape of the final particle spectra, so it is important to understand it properly.

A thorough discussion of the different contributions to the overall resolution is given in the PhD thesis by C. E. Jorgensen [21]¹. I will here only summarize the main points, as a foundation for the experimental determination of resolutions presented in chapter 4.

B.1 Angular and momentum resolution

A track through the BRAHMS spectrometer has two main characteristics — its momentum, as determined from the bending through the magnets, and its position as determined in the tracking chambers. The latter can be translated into measurements of angles, and we can define two main resolutions: the bending angle resolution $\sigma_{\Delta\theta}$, and the momentum resolution σ_p .

Bending angle resolution

The bending angle resolution $\sigma_{\Delta\theta}$ of the spectrometer is in turn determined by two main contributions:

- The multiple Coulomb scattering suffered by a particle as it traverses the detector medium and surrounding air. This process results in a Gaussian smearing of width $\sigma_{\theta_{ms}} = K/\beta p$, where K is a material constant for each detector segment. Typical values of K in BRAHMS are $2 - 5 \cdot 10^{-3}$ GeV/c (see [21] for details).
- The accuracy with which the local track angle is measured by the trackers. Assuming that the track position is sampled at N points separated by distances l , this width can be calculated through linear regression to be

$$\sigma_{\theta_{track}} = \frac{\sigma_x}{l} \sqrt{\frac{12}{N(N^2 - 1)}} \quad (\text{B.1})$$

¹See section 4.2.4 of ref. [21].

where σ_x is the intrinsic spatial resolution of a measured point. For the BRAHMS trackers, this typically gives a resolution of $\sigma_{\theta_{track}} \approx 0.001 \text{ mrad}$.

From these contributions, we calculate a total bending angle resolution of

$$\sigma_{\Delta\theta} = \sqrt{\sigma_{\theta_{ms}}^2 + (\sigma_{\theta_f}^2 + \sigma_{\theta_b}^2)} \quad (\text{B.2})$$

where $\sigma_{\theta_{f,b}}$ are the angular resolutions for a front (f) and back (b) detector pair.

Momentum resolution

For the total momentum resolution σ_p , we start with the equation for determining the momentum p from a tracker pair f and b :

$$p = \frac{qB\Delta L}{\sin\theta_f - \sin\theta_b} \frac{1}{\sqrt{1 - \alpha_y^2}}. \quad (\text{B.3})$$

where $\Delta\theta \equiv \sin\theta_f - \sin\theta_b$ is the total bending angle between the trackers and α_y is the slope of the track in the y direction. Using the small-angle approximation and gathering the units, we get $p = 0.3B\Delta L/\Delta\theta^2$. The momentum resolution can then be expressed as

$$\frac{\sigma_p^2}{p^2} = \frac{\sigma_{\Delta\theta}^2}{\Delta\theta^2} = \sigma_{\Delta\theta}^2 \frac{p^2}{(0.3B\Delta L)^2} = \left(\frac{K^2}{\beta^2 p^2} + \sigma_{\theta_{f+b}}^2 \right) \frac{p^2}{(0.3B\Delta L)^2}, \quad (\text{B.4})$$

which gives

$$\sigma_p^2 = \frac{1}{(0.3B\Delta L)^2} \left(\frac{K^2 p^2}{\beta^2} + \sigma_{\theta_{f+b}}^2 p^4 \right). \quad (\text{B.5})$$

The above equations can be used in combination to extract realistic values for the resolutions of the BRAHMS spectrometers. This has been done in ref. [21], and the numbers found are consistent with those we observe in experimental data. In the next section, I will determine the resolutions experimentally through fits to the particle identification plots, to make certain that we know the fraction of the total yield that lies within the cuts set. This effectively shortens the momentum range where we can perform certain PID, but this was deemed acceptable for the present analysis.

B.2 Transverse momentum resolution

The final charged particle spectra will be presented as a function of the transverse momentum $p_T = p \sin\theta$, where θ is the polar angle relative to the beamline, or of the transverse mass $m_T = \sqrt{p_T^2 + m^2}$. A Gaussian uncertainty in p_T will have the effect of hardening the spectra, i.e. on average shifting the measured transverse momentum to a higher value. This is because our measured spectra are strongly decreasing with p_T , so an upward shift will add relatively more to the yield than a downward shift.

²Here the charge of the particle is set to one and the factor 0.3 comes from the conversion of the units ($[p] = \text{GeV}/c$, $[B\Delta L] = \text{Tm} = \text{Ns}/\text{Cm}$ and the charge $q = 1.6 \times 10^{-19} \text{ C}$)

The p_T resolution is a function of the momentum and angular resolutions σ_p and σ_θ , and can be found through propagation of errors:

$$\sigma_{p_T}^2 = \left(\frac{\partial p_T}{\partial p} \sigma_p \right)^2 + \left(\frac{\partial p_T}{\partial \theta} \sigma_\theta \right)^2 = (\sin \theta)^2 \sigma_p^2 + p^2 (\cos \theta)^2 \sigma_\theta^2. \quad (\text{B.6})$$

It is clear that at midrapidity (around 90°) this resolution will be dominated by the momentum resolution, while at forward angles the angular resolution is dominant. From the information above, it is possible to “deconvolute” the p_T spectra, removing the effects of resolution smearing. This is important for high- p_T analyses where the exact shapes of the spectra reveals interesting physics, but it has not been done for the present analysis.

Appendix C

Estimating net–baryon production and stopping

This appendix discusses in more detail the estimate of net–baryon production from net–protons used in the fourths paper in chapter 5, and how the stopping estimate is calculated.

As discussed in ref. [55], the average rapidity loss $\langle\delta y\rangle = y_p - \langle y\rangle$ of the nucleons participating in a heavy ion collision can be used to quantify the degree of stopping. $\langle y\rangle$ is calculated as

$$\langle y\rangle = \frac{2}{N_{part}} \int_0^{y_p} y \cdot \frac{dN_{(B-\bar{B})}(y)}{dy} \cdot dy, \quad (\text{C.1})$$

where N_{part} is the number of participating nucleons in the collision and $dN_{(B-\bar{B})}(y)/dy$ is the distribution of net–baryons.

What we measure in BRAHMS is the distribution of net–protons $dN_{(p-\bar{p})}(y)/dy$ over the rapidity interval $0 \lesssim y \lesssim 3$, while at $\sqrt{s} = 200$ GeV the projectile rapidity is $y_p = 5.36$. This means that we must

1. estimate the net–baryon production from the net–proton distribution within our acceptance
2. extrapolate the estimated $dN_{(B-\bar{B})}(y)/dy$ up to the projectile rapidity, using conservation of total net baryon number

In the following I discuss how this has been done for BRAHMS $p + p$ data, following a discussion in refs. [54, 24]

C.1 Estimating the net–baryon distribution

The net–baryon yield in a $p + p$ collision can be summed up as the production of all baryons minus the production of all antibaryons:

$$n_B = n_p + n_n + n_\Lambda + n_{\Sigma^+} + n_{\Sigma^-} \quad (\text{C.2})$$

where $n_x = N_x - N_{\bar{x}}$ is the net yield of a single baryon species. Heavier baryon species are assumed not to contribute significantly to the net–baryon distribution at this energy.

Ξ production is evaluated as part of the Λ contribution, since $\Xi \rightarrow \Lambda\pi^0$ with a branching ratio of 99.51% [79].

To estimate $dN_{(B-\bar{B})}(y)/dy$ we use the fact that we have a measured distribution of $n_{p,meas}$, and equation C.2 can be rewritten as

$$n_B = n_{p,meas} \cdot \frac{n_p + n_n + n_\Lambda + n_{\Sigma^+} + n_{\Sigma^-}}{n_p + c_1 n_\Lambda + c_2 n_{\Sigma^+}} \quad (\text{C.3})$$

The factor in the denominator is just $n_{p,meas}$ written out as a sum of contributions from primary protons (n_p), primary Λ s misidentified as protons ($c_1 n_\Lambda$) and the same for Σ^+ ($c_2 n_{\Sigma^+}$). Using a full GEANT simulation of the BRAHMS spectrometer as it was during 2001 data taking, the coefficients have been estimated in [54] to be $c_1 = 0.53 \pm 0.05$ protons for each Λ and $c_2 = 0.49 \pm 0.05$ protons for each Σ^+ decay. This estimate is for Au+Au collisions, and so may be slightly different for $p+p$ since the slopes of the Λ and p distributions will be different for the two systems. To make a safe estimate, we use $c_1 = c_2 = 0.5 \pm 0.1$ for the present analysis.

Net-neutrons

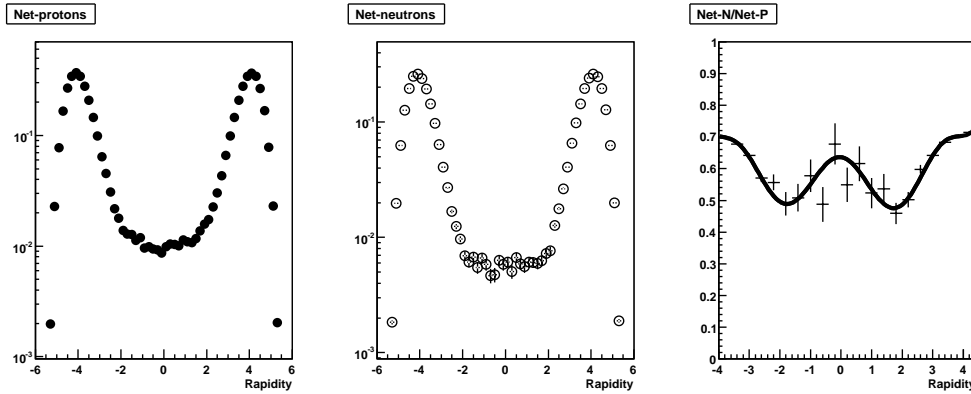


Figure C.1: Net-proton (left) and net-neutron (center) distributions from PYTHIA. The right panel shows the ratio n_n/n_p as a function of rapidity, and a 6th order polynomial fit used to extract numerical values.

No measurement of neutron production in $p+p$ collisions exists at RHIC energies, but nucleon production is in general well described by commonly used string fragmentation models. To estimate the net-neutron distribution as a function of rapidity, a PYTHIA simulation at $\sqrt{s} = 200$ GeV has been used. The result is shown in figure C.1, where the left and middle panels show the n_p and n_n distributions respectively. The right panel shows the ratio of the net-curves, n_n/n_p , and (solid line) a 6th-order polynomial fit. This functional form was chosen because it is the lowest order function that reproduces the global features of the data.

From this simulation and fit, we find that the ratio varies from $n_n/n_p = 0.50 \pm 0.03$ to $n_n/n_p = 0.70 \pm 0.03$ within the range $|y| < 3$.

Net-lambdas

To estimate n_Λ we use preliminary data from the STAR experiment, as these are the only experimental values available at this energy. In reference [144] from the Quark Matter 2002 conference, STAR show production spectra of $\Lambda + \bar{\Lambda}$ and $\Xi + \bar{\Xi}$ in $p + p$ collisions at $\sqrt{s} = 200$ GeV, and also quote values for the ratios $\bar{\Lambda}/\Lambda$ and $\bar{\Xi}/\Xi$. See table C.1.

$\Lambda + \bar{\Lambda}$	$\bar{\Lambda}/\Lambda$	$\Xi + \bar{\Xi}$	$\bar{\Xi}/\Xi$	p	\bar{p}
0.066 ± 0.006	0.88 ± 0.09	0.0036 ± 0.0012	0.90 ± 0.09	0.096 ± 0.002	0.079 ± 0.002

Table C.1: Strange particle production in $p + p$ collisions at $\sqrt{s} = 200$ GeV. Preliminary hyperon data from STAR [144]. (Anti-)Proton data are from [119] and [118].

From these values we can calculate the total and net production n_Λ and n_Ξ . Since $\Xi \rightarrow \Lambda\pi^0$ with a branching ratio of 99.51% and we are unable to distinguish between the two, Ξ production is added into the Λ production. As noted in the paper on $p + p$ yields in chapter 5, STAR has also reported midrapidity values of (anti-)proton production. The spectra are shown in ref. [118], where they also quote a total hyperon feed-down correction of 20% for both species. The integrated values are presented in ref. [119] without this hyperon correction. In table C.1 (and in chapter 5) I list the STAR yields from [119] with the 20% correction included. Using only STAR values we can now estimate that $n_\Lambda/n_p = 0.38 \pm 0.05$ at $|y| < 0.5$.

For the sake of this analysis, we will assume that n_Λ/n_p is constant over the rapidity range $|y| < 3$.

Net-sigmas

The yields of Σ^+ and Σ^- have not been measured at RHIC, in any collision type. In thermal models for Au+Au collisions $N_{\Sigma^+} \sim N_{\Sigma^-}$ and $N_{\Sigma^-} \sim 0.1 \cdot N_p$ [145] at RHIC ($\sqrt{s_{NN}} = 130$ GeV). Since strangeness production is heavily enhanced in heavy ion reactions compared to $p + p$ this value will be lower for the present analysis. Around midrapidity, PHENIX have shown that $(n_\Lambda/n_p)_{Au+Au} \approx 0.9$ at $\sqrt{s_{NN}} = 130$ GeV, yielding a ratio of $(n_\Lambda/n_p)_{Au+Au}/(n_\Lambda/n_p)_{p+p} \approx 2.4$ using the $p + p$ values cited above.

Taking this as a guide, we estimate $n_{\Sigma^+}/n_p = n_{\Sigma^-}/n_p = 0.05 \pm 0.04$ in $p + p$ collisions at $\sqrt{s} = 200$ GeV, the large error reflecting the uncertainty of this estimate. Again, we assume that the ratio is constant over the rapidity interval covered by the data.

Final conversion factor and net-baryon distribution

Adding all this together, we can calculate a total conversion factor from net-protons to net-baryons that varies from $n_B = 1.58 \pm 0.06 \cdot n_{p,meas}$ to $n_B = 1.71 \pm 0.07 \cdot n_{p,meas}$ over the range $0 < y < 3$.

In the following sections, the measured net-proton distribution is scaled up by this factor to calculate the net rapidity loss. The left panel of figure C.2 shows the original n_p and calculated n_B distributions.

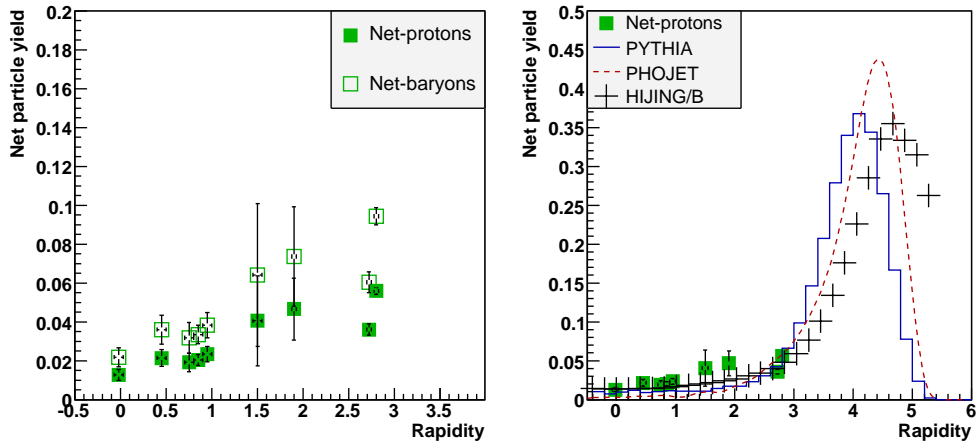


Figure C.2: Left panel: Net-baryon and net-proton distributions from $p + p$ collisions at $\sqrt{s} = 200$ GeV. Right panel: Net-proton distribution overlaid with model calculations from PYTHIA (histogram), PHOJET (dashed line), and HIJING/B (plus-line).

C.2 Fit functions and results

The next task is to extrapolate the $dN_{(B-\bar{B})}(y)/dy$ up to the beam rapidity and then calculate $\langle y \rangle$. We know that the total integral of the net-baryon curve must be equal to the initial conserved baryon number of the reaction, i.e. 2 for a $p + p$ collision. Looking at the right panel of figure C.2 it is clear both from the integral over the region $0 < y < 3$ and from the model calculations shown that most of this baryon yield lies outside of the measured region. Fitting the region $0 < y < 3$ to a first-order polynomial gives a reasonable χ^2 , and integrating gives $\langle B - \bar{B} \rangle = 0.16 \pm 0.02$ ($0 < y < 3$).

We now have three options on how to place the remaining baryon yield, one semi-realistic and two extremes:

1. In a bell-shaped curve with a centroid between $y = 3.0$ and $y_p = 5.36$, as indicated by model calculations
2. In a narrow peak just outside the experimental acceptance, at $y = 3.5$
3. In a narrow peak just inside projectile rapidity, at $y = 5.0$

While the first case probably gives a good approximation of the real net-baryon curve, the second and third options will give absolute upper and lower limits on the net rapidity loss given what we have measured. We therefore calculate all three, to find a probable value inside a known interval.

For the second and third cases, the $\langle y \rangle$ value can be easily calculated from equation C.1 using the linear fit discussed above. We get

$$\langle \delta y \rangle_{max} = 1.6 \pm 0.1 \quad (\text{C.4})$$

$$\langle \delta y \rangle_{min} = 0.3 \pm 0.1 \quad (\text{C.5})$$

The first case requires a bit more work. In ref. [54], two possible parameterizations of the unknown net-baryon peak are suggested — a sixth-order polynomial in y , the

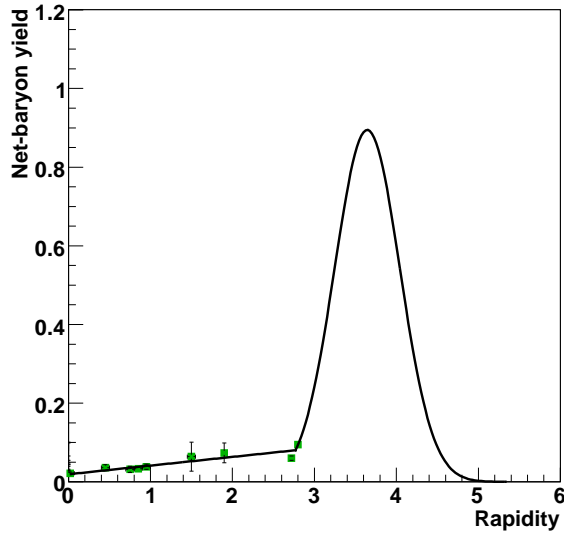


Figure C.3: Realistic estimate of the total stopping, by fitting a Gaussian to the two highest net-baryon points and constraining its integral to the remaining baryon number. See text for curve parameters.

lowest order polynomial which can be constrained to have the right shape and integral, and a Gaussian in momentum space, calculated through $p = m \sinh(y)$. However, as seen in the right panel of figure C.2, there is a wide variety of predictions for this functional form and distinguishing between them is not possible from the dataset presented in this thesis.

To make a simple estimate of a realistic value for the baryon stopping, we fit a Gaussian to the last two points of the net baryon distribution and require both that it have the right integral and that it goes to 0 around the beam rapidity. See figure C.3. The fitted curve has a mean of $\mu = 3.6$, the same as the PYTHIA curve for net-protons in figure C.2. Inserting this curve into formula C.1, we estimate a realistic value of the total rapidity loss per incident nucleon to be

$$\langle \delta y \rangle_{mean} = 1.3 \tag{C.6}$$

(No error is given, since this is just an estimate from one possible realistic function.)

Appendix D

SNAccPack, an acceptance package for BRAHMS

As part of my work on charged particle production in $p + p$ collisions, I have developed a general software tool called SNAccPack¹ for easy generation of acceptance maps for the BRAHMS geometry. Being both fast, disk space efficient and general in the sense that it is usable for all BRAHMS runs and configurations, SNAccPack offers significant advantages over other available packages. In the following I briefly review its main features and give examples of generated maps. For full details on usage, I refer to the README file included with the source code.

SNAccPack is available to the BRAHMS collaboration through our CVS repository. To check it out, do

```
> klog
> cvs checkout snaccpack
```

on a machine with access to the repository.

D.1 SNAccPack basics

At first glance, SNAccPack is an organized collection of python programs and runner scripts for the GEANT simulation package [127] and the ROOT analysis framework [146]. SNAccPack produces, through a four step procedure, ROOT files containing acceptance maps for unidentified charged hadrons, pions, kaons, protons and deuterons, for a specific BRAHMS setup. For identified particles, both $y - p_T$ and $y - m_T$ maps are provided. A setup here means a given detector configuration, spectrometer angle, magnetic field fraction and polarity. These acceptance maps are based on full GEANT simulations of the BRAHMS detector setup.

The four steps needed to produce a map are as follows:

1. Run the script `snaccpack.py` with a given run and number of events as input, to produce a number of geometry and input files for the later steps. Detector setup,

¹SNAccPack is an acronym for *Somewhat New Acceptance Package*. The 'somewhat' comes from the fact that it is based on an earlier, less generalized acceptance package by Peter Christiansen.

	Step 1	Step 2	Step 3	Step 4
Time [minutes]	1	60	120	5
File size [Mb]	0	1000/1M events	100/1M events	1

Table D.1: Example SNAccPack run statistics, using the BRAHMS computing farm.

field settings etc. are specified through the given run, which SNAccPack uses to extract information from the run and geometry databases.

2. Run GEANT, or more specifically the BRAG implementation of the BRAHMS geometry in GEANT, using the shell scripts generated in step 1. Commands are available both for running GEANT jobs interactively, and for submitting them simultaneously to a CONDOR queue. The cdat files that contain the simulation output are large, and take a long time to read through. This has been one of the limiting factors for easy use of GEANT in BRAHMS. Note that only energy loss through interactions with matter is simulated in SNAccPack. Other effects, such as in-flight weak decays or multiple scattering in detector materials must be explicitly corrected for elsewhere.
3. Once the GEANT simulations are done, run another set of shell scripts generated in step 1 that read the cdat output files and rewrite them as ROOT tree structures. Little information is lost in this step, but the ratio of the file sizes is approximately 10:1.
4. Finally, tune and run a set of ROOT macros, also generated in step 1, that read the simulation ROOT trees and write the final acceptance maps to small (<1Mb), easy-to-use ROOT files. Fiducial cuts and vertex ranges are selected in this final step, so remaking maps is quick if one wants to change analysis parameters.

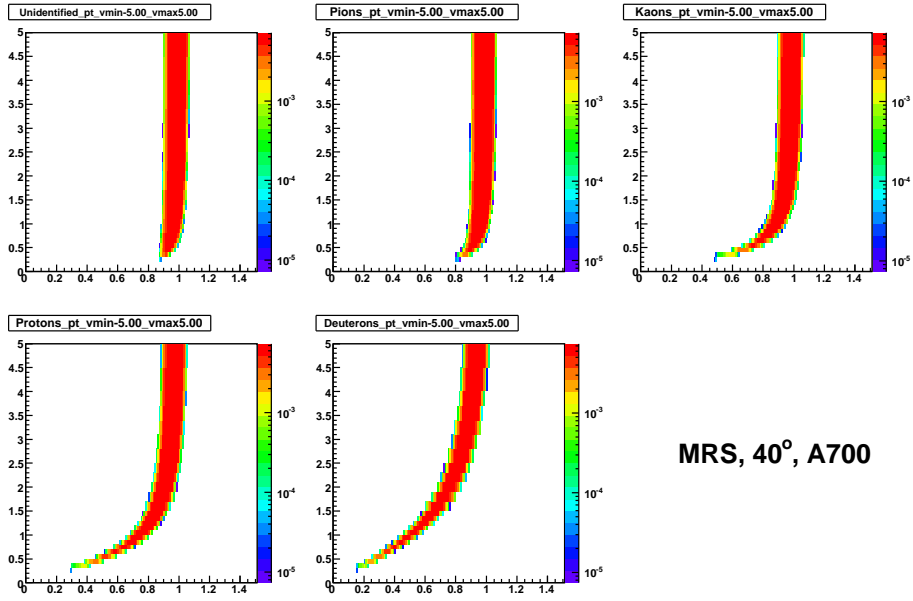
In addition, some example code is also provided to read and use SNAccPack maps in analysis code. It is possible both to get the entire maps as 2-dimensional histograms, and single-particle acceptance values for a given PID, rapidity and p_T or m_T .

Table D.1 lists example time and storage requirements for a SNAccPack run, generating 20 million events for a single setting. The time estimates shown assume job submission to the BRAHMS computing farm, and that at least 20 farm CPUs are available for use. This is normally the case under regular work conditions. From these numbers, it is possible to generate acceptance maps for an entire dataset (usually consisting of approximately 20 different settings) in 2-3 days.

D.2 Example maps

Figures D.1, D.2 and D.3 show example acceptance maps generated by SNAccPack for the MRS (40°), FFS (12°) and full FS (3°) respectively, using the detector setup of the 2001 $p+p$ data. They also show the evolution of the BRAHMS acceptance as function of rapidity and p_T as we move from midrapidity to the most forward rapidities.

All maps exhibit a central region where the acceptance value is approximately constant, and an edge where it drops rapidly. This edge corresponds to particles flying close to the physical edges of the spectrometer. In an analysis situation this edge is removed,



MRS, 40° , A700

Figure D.1: Acceptance maps generated by SNAccPack. 20 million events. Setting: MRS, 40° , 700A

since there may be effects close to the edges of the spectrometer that are not properly simulated by GEANT. Note that as we move forward in rapidity, this flat, mid-acceptance region becomes narrower in rapidity, and the edge becomes more pronounced.

For comparisons of SNAccPack acceptance maps with experimental data, see section 4.4 on page 67.

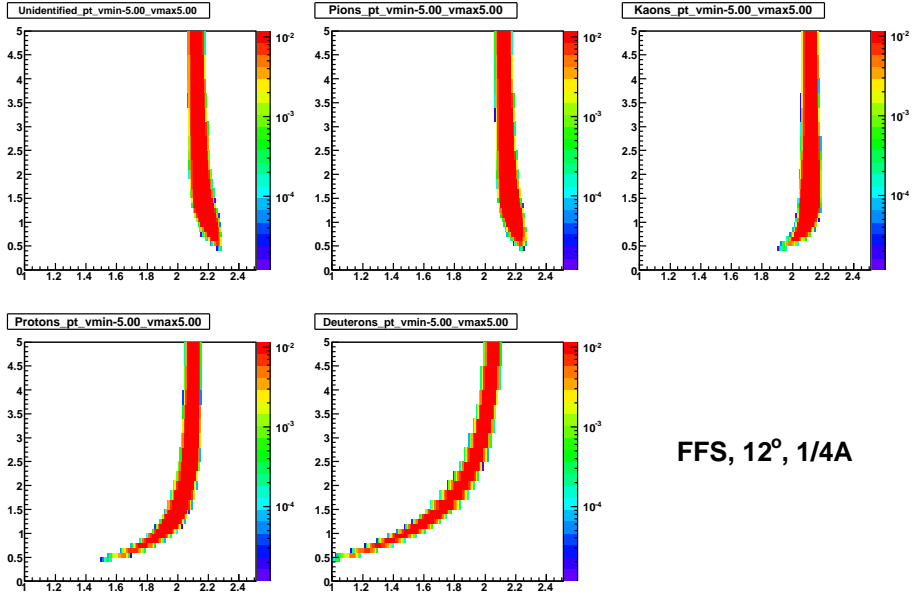


Figure D.2: Acceptance maps generated by SNAccPack. 20 million events. Setting: FFS, 12° , 1/4A

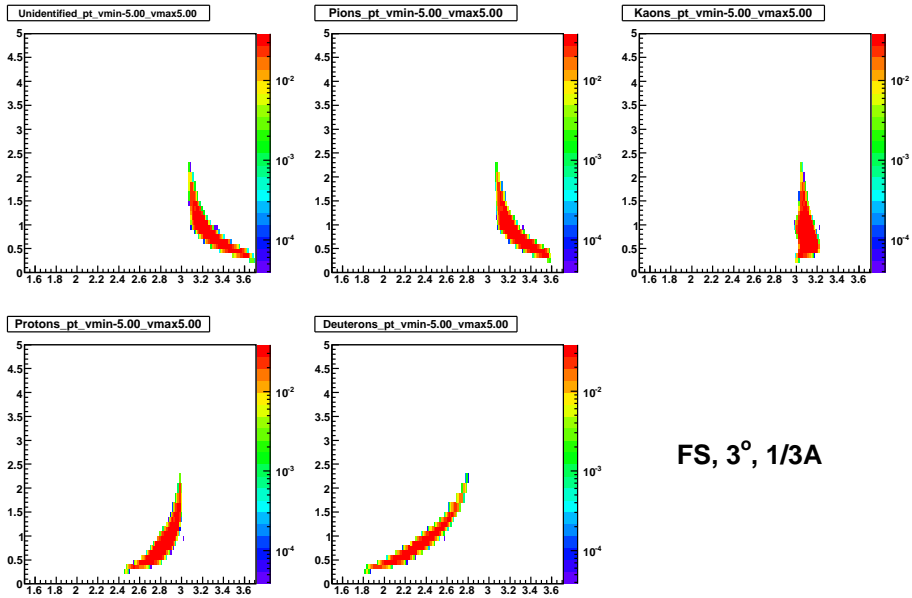


Figure D.3: Acceptance maps generated by SNAccPack. 20 million events. Setting: FS, 3° , 1/3A

Appendix E

The BRAHMS collaboration

At the time of writing, the BRAHMS collaboration has the following members and institutions:

I. Arsene¹⁰, I. G. Bearden⁷, D. Beavis¹, C. Besliu¹⁰, B. Budick⁶, H. Bøggild⁷,
C. Chasman¹, C. H. Christensen⁷, P. Christiansen⁷, J. Cibor⁴, R. Debbe¹, E. Enger²,
J. J. Gaardhøje⁷, M. Germinario⁷, K. Hagel⁸, H. Ito¹¹, A. Jipa¹⁰, F. Jundt³, J. I. Jørdre⁹,
C. E. Jørgensen⁷, R. Karabowicz⁴, E. J. Kim⁵, T. Koscic⁴, T. M. Larsen², J. H. Lee¹,
Y. K. Lee⁵, S. Lindal², G. Løvholden², Z. Majka⁴, A. Makeev⁸, M. Mikelsen²,
M. Murray⁸, J. Natowitz⁸, B. Neumann¹¹, B. S. Nielsen⁷, D. Ouerdane⁷, R. Płaneta⁴,
F. Rami³, C. Ristea¹⁰, O. Ristea¹⁰, D. Roehrich⁹, B. H. Samset², D. Sandberg⁷,
S. Sanders¹¹, I.S.Zgura¹⁰, R. A. Sheetz¹, P. Staczal⁷, T. S. Tveter², F. Videbæk¹,
R. Wada⁸, I. S. Zgura¹⁰

¹ Brookhaven National Laboratory, Upton, NY 11973-5000, USA

² Fysisk Institutt, University of Oslo, Blindern, Norway.

³ IReS, University Louis Pasteur, Strasbourg, France.

⁴ Jagiellonian University, Krakow, Poland.

⁵ Johns Hopkins University, Baltimore, USA.

⁶ New York University, USA.

⁷ Niels Bohr Institute, University of Copenhagen, Denmark.

⁸ Texas A&M University, College Station. USA

⁹ University of Bergen, Norway.

¹⁰ University of Bucharest, Romania

¹¹ University of Kansas, USA.

Also see the authors listings of the papers reprinted in chapter 5.

List of Figures

1.1	Elementarity, a history	3
1.2	The elements of the Standard Model. Figure from [4].	4
1.3	The running coupling constant	6
1.4	Proton parton density function vs. x at $Q^2 = 20\text{GeV}^2$	7
1.5	Lattice QCD results show a phase transition	8
1.6	Effective quark potential	8
1.7	Nuclear phase diagram	9
1.8	Heavy ion collision geometry	10
1.9	Impact parameter and centrality illustration	11
1.10	Stopping vs. transparency	12
1.11	Collision evolution at RHIC	13
1.12	$dN/d\eta$ at $\sqrt{s} = 200$ GeV vs. centrality	14
1.13	$dN/d\eta$ per participant pair vs. \sqrt{s}	14
1.14	dN/dy for identified particles at $\sqrt{s} = 200$ GeV from BRAHMS	15
1.15	BRAHMS IDd particle spectra around midrapidity, and blast wave fits	16
1.16	Charged like-particle ratios from Au+Au vs. rapidity, and rapidity correlations	17
1.17	Nuclear modification factors for charged hadrons in Au+Au at $\sqrt{s} = 200$ GeV from BRAHMS. [47]	18
1.18	v_2 from STAR. Plot from [28].	19
1.19	Stopping in A+A collisions vs. energy. Data from [54].	19
2.1	Diagrams for elastic (left) and single diffractive (right) scattering in a $p + p$ collision.	24
2.2	String excitation and fragmentation	25
2.3	Two string formation mechanisms for a $p + p$ collisions: a) Longitudinal excitation. b) Color exchange. Figure from [75].	26
2.4	Two diagrams for nucleon-nucleon interactions in Regge theory. Left: Diquark conserving term. Note that both incoming nuclei are split into a quark and a diquark. Right: Diquark breaking term, where the top-most nucleon is split into three quarks through the exchange of another pomeron. Figures from [57].	27
2.5	Baryon junction	28
2.6	s-channel and t-channel reactions	30

2.7	Predictions from the HIJING (solid), HIJING/B (dashed) and HIJING/B with 'ropes' (dotted) compared with experimental data from SPS. The upper two panels show net-proton distributions in A+A collisions, while the lower right panel shows predictions for Au+Au collisions at RHIC energies. Figure from [98].	31
2.8	Statistical model description of multiplicities in $p + p$	33
2.9	$p + p$ and $p + \bar{p}$ total and elastic cross sections, as a function of collision energy. Compilation of data by the PDG [79].	35
2.10	Average multiplicities up to ISR energies. Data from [114]. Fits have been re-done here.	36
2.11	Meson production as a function of rapidity at $\sqrt{s} = 17.3$ GeV, as measured by the NA49 experiment at SPS. Plots from the thesis of C. Hoehne [117]. The pion data have recently been published in ref. [116].	37
2.12	Identified charged particle spectra from $p + p$ and $d + \text{Au}$ collisions at $\sqrt{s} = 200$ GeV, averaged over the rapidity interval $-0.5 < y < 0$. Data from the STAR collaboration [118].	37
2.13	Neutral pion production in $p + p$ collisions at midrapidity, measured by the PHENIX collaboration. Data from ref. [72].	38
2.14	$(h^+ + h^-)/2$ at $y=0$ over two orders of magnitude in incident energy. Compilation from [31], see references therein for data.	38
3.1	The RHIC accelerator complex. Figure from [21].	39
3.2	Schematic view of the RHIC interaction region. 'Yellow' and 'Blue' are the names of the two accelerator rings. Figure from [21].	40
3.3	An overview of the BRAHMS detector setup for the 2001–2002 run.	41
3.4	The full BRAHMS acceptance in $y - p_T$ for pions, kaons and protons. The gray region shows the area accessible to our PID systems, assuming design resolution, while the blue and red regions show the acceptances for example spectrometer settings. Figure from [21].	43
3.5	The BRAHMS coordinate system, relative to the beam line and the two spectrometers.	44
3.6	The inelastic counter setup.	45
3.7	TPC electron drift and readout plane	47
3.8	Tracking in the Drift Chambers	48
3.9	Track line crossing hodoscope slats in the FS	49
3.10	Side views of the Cherenkov detectors implemented for the 2001 and 2003 runs. Left: C1, a threshold detector. Right: RICH, a ring-imaging detector, with spherical focusing mirror and segmented image plane.	51
4.1	Number of triggers used in the analysis of the 2001 $p + p$ dataset. See also table 4.2 on page 59.	55
4.2	Example of experimental resolution of vertex determination from INEL counters.	56
4.3	Track matching geometry in BRAHMS	57

4.4	Left: Correlation of the momentum from D2 with the momentum from D4, for data from the 3° setting. The line is $p_{D2} = p_{D4}$. Right: The refitted FS momentum (see text) versus the average momentum from D2 and D4.	58
4.5	Particle identification from the MRS time-of-flight wall, from the 60° 1/4 field setting. Left panel: m^2 vs. momentum with resolution fits as discussed in the text. Right panel: The resulting separation in experimental m^2 , where the unshaded histogram shows all accepted particles.	60
4.6	As figure 4.5, for H1 at 20° 1/12 field.	61
4.7	Particle identification from the FS RICH, from the 3° 1/3 field setting. Left panel: m^2 vs. momentum with resolution fits as discussed in the text. The sharply rising line shows the threshold momentum. Right panel: The resulting separation in experimental m (both charge signs).	62
4.8	Left: C1 reconstructed energy vs. associated track momentum, for a 12° 1/4 field setting. Lines show wide cuts around the theoretical energy response curve. Right: m^2 vs. momentum from H1 for all particles (top), and the same with pions identified in C1 excluded (bottom).	63
4.9	Fiducial cut on track position at the backplane of TPM2, 60° 1/4B field. The experimental edges and track density distribution varies somewhat with the field setting, so cuts are set that are inside the edges for all settings.	64
4.10	Fiducial cut on TOFW slat number. Figure shows all slats struck by reconstructed particles in a 60° 1/4B field setting (2001 run), and the shaded region shows the accepted hits. The two empty bins are defective slats.	64
4.11	2001 dataset: Comparison of proton acceptance at 60° for favored (contour) and disfavored (boxes) charges. Edge effects are felt where the color changes rapidly or the boxes are small. Cutting this area away leaves a wide usable coverage for the favored charge but not for the disfavored.	65
4.12	Effect of wide simultaneous cuts in the particle y position at the magnet midplane (left) and the track slope difference (left) in the FFS, i.e. for the T1–D2–T2 complex. Data from a 4° 1/4A run.	66
4.13	Examples of track projections to the $x = 0$ plane, with Gaussian fits and 2σ cuts (red lines). Data are from 60° (top row) and 3° (bottom row).	67
4.14	Examples of corrections for physical processes: a) Mult. scattering, in-flight weak decays and absorption, excluding the trigger slat, MRS, 60° . b) Effects of the trigger slat, MRS, 60° . c) As (a), for the full FS, 4° . d) As (b), for the full FS, 4°	68
4.15	Example of background subtraction estimate, for unidentified charged hadrons ($h^+ + h^-$) at 60° . The left panel shows the y track projection coordinate at $x = 0$ as a function of p_T , while the four right-hand panels show projections for four p_T regions. Also shown are double-Gaussian fits and resulting background distributions.	69
4.16	p_T -dependent background correction for unidentified charged hadrons, 60° and 12° settings, extracted from double-Gaussian fits as shown in fig. 4.15. Pion corrections are similar in shape and magnitude.	70

4.17	Feed-down corrections from Λ (solid lines) and $\bar{\Lambda}$ (dashed lines). Left panel: Correction for the MRS and the FFS, as a function of momentum. Right panel: Correction for the full BFS, as a function of transverse momentum.	70
4.18	Acceptance maps for the MRS at 60° , overlaid with experimental data (boxes). The rows show three different vertex bins, while the columns from left to right show unidentified particles (in pseudorapidity), pions, kaons and protons.	71
4.19	Acceptance maps for the FFS at 12° , overlaid with experimental data (boxes). The rows show three different vertex bins, while the columns from left to right show unidentified particles (in pseudorapidity), pions, kaons and protons.	72
4.20	Tracking efficiency estimates.	73
4.21	Sample efficiency distributions for the H1 hodoscope for 2001 data, as a function of momentum.	73
4.22	RICH efficiency as a function of the particle velocity β , calculated by projecting identified particles from H2 to the RICH plane and looking for a matching light ring. The dashed line is a fit to the data used to interpolate between the histogram bins. Original efficiency data from [23].	74
4.23	RICH contamination	75
4.24	Normalized $\eta - p_T$ distribution of the full 2001 $p + p$ dataset, for unidentified charged particles (h^\pm).	77
4.25	Normalized $y - p_T$ distribution of the full 2001 $p + p$ dataset, for π^\pm , K^\pm , p and \bar{p} . Lines represent the edges of projections to the p_T axis that become the normalized spectra.	78
4.26	Averaged projection of data within interval Δy (between the lines) to the p_T axis. The histogram in the right panel is a normalized particle spectrum.	80
4.27	Comparison of common fit functions for extrapolation to high and low p_T . Spectrum shown: π^+ at $y \sim 0.5$. Closed symbols: p_T Open symbols: m_T	82
4.28	Comparison of common fit functions for extrapolation to high and low p_T . Spectrum shown: K^+ at $y \sim 0.8$. Closed symbols: p_T Open symbols: m_T	83
4.29	Comparison of common fit functions for extrapolation to high and low p_T . Spectrum shown: p at $y \sim 0.8$. Closed symbols: p_T Open symbols: m_T	84
5.1	Saturation of 'wee partons' as the energy increases. Figure from [140].	90
A.1	A generic $2 \rightarrow 2$ reaction.	100
A.2	Coordinate system, as used in this thesis.	100
C.1	Net-proton (left) and net-neutron (center) distributions from PYTHIA. The right panel shows the ratio n_n/n_p as a function of rapidity, and a 6th order polynomial fit used to extract numerical values.	110

C.2	Left panel: Net-baryon and net-proton distributions from $p + p$ collisions at $\sqrt{s} = 200$ GeV. Right panel: Net-proton distribution overlaid with model calculations from PYTHIA (histogram), PHOJET (dashed line), and HIJING/B (plus-line).	112
C.3	Realistic estimate of the total stopping, by fitting a Gaussian to the two highest net-baryon points and constraining its integral to the remaining baryon number. See text for curve parameters.	113
D.1	Acceptance maps generated by SNAccPack. 20 million events. Setting: MRS, 40° , 700A	117
D.2	Acceptance maps generated by SNAccPack. 20 million events. Setting: FFS, 12° , 1/4A	118
D.3	Acceptance maps generated by SNAccPack. 20 million events. Setting: FS, 3° , 1/3A	118

LIST OF FIGURES

Bibliography

- [1] C. Y. Wong. Introduction to high-energy heavy ion collisions. Singapore, Singapore: World Scientific (1994) 516 p.
- [2] L. P. Csernai. Introduction to relativistic heavy ion collisions. Chichester, UK: Wiley (1994) 310 p.
- [3] F. Halzen and A. D. Martin. *Quarks & leptons*. Wiley, 1984.
- [4] ATLAS Webpage at KEK. <http://atlas.kek.jp/sub/photos/Physics/PhotoPhysicsSM.html>.
- [5] Y. Fukuda et al. Evidence for oscillation of atmospheric neutrinos. *Phys. Rev. Lett.*, 81:1562–1567, 1998.
- [6] M. C. Gonzalez-Garcia and Yosef Nir. Developments in neutrino physics. *Rev. Mod. Phys.*, 75:345–402, 2003.
- [7] Robert Oerter. *The Theory of Almost Everything: The Standard Model, the Unsung Triumph of Modern Physics*. Pi Press, 2005.
- [8] R. Barate et al. Studies of quantum chromodynamics with the aleph detector. *Phys. Rept.*, 294:1–165, 1998.
- [9] Sonia Kabana. Pentaquarks: Review of the experimental evidence. *J. Phys.*, G31:S1155–S1164, 2005.
- [10] Shin Muroya, Atsushi Nakamura, Chiho Nonaka, and Tetsuya Takaishi. Lattice QCD at finite density: An introductory review. *Prog. Theor. Phys.*, 110:615–668, 2003.
- [11] Z. Fodor and S. D. Katz. A new method to study lattice QCD at finite temperature and chemical potential. *Phys. Lett.*, B534:87–92, 2002.
- [12] Victor Elias and Subhash Rajpoot. Low unifying mass scales without intermediate chiral color symmetry. *Phys. Rev.*, D20:2445, 1979.
- [13] A. D. Martin, R. G. Roberts, W. J. Stirling, and R. S. Thorne. Parton distributions incorporating QED contributions. *Eur. Phys. J.*, C39:155–161, 2005.
- [14] S. Chekanov et al. A zeus next-to-leading-order QCD analysis of data on deep inelastic scattering. *Phys. Rev.*, D67:012007, 2003.
- [15] R. Hagedorn. Statistical thermodynamics of strong interactions at high-energies. *Nuovo Cim. Suppl.*, 3:147–186, 1965.
- [16] Frithjof Karsch. Lattice results on QCD thermodynamics. *Nucl. Phys.*, A698:199–208, 2002.
- [17] P. Braun-Munzinger and J. Stachel. Particle ratios, equilibration, and the QCD phase boundary. *J. Phys.*, G28:1971–1976, 2002.
- [18] Helmut Satz. Limits of confinement: The first 15 years of ultra-relativistic heavy ion studies. *Nucl. Phys.*, A715:3–19, 2003.

- [19] CERN Press release, 2000. <http://pressold.web.cern.ch/PressOld/Releases00/PR01.00EQuarkGluonMatter.html>.
- [20] C. A. Ogilvie. Review of nuclear reactions at the ags. *Nucl. Phys.*, A698:3–12, 2002.
- [21] C. E. Jorgensen. *High p_T Charged Hadron Production at RHIC*. PhD thesis, Niels Bohr Institute, 2004.
- [22] Miklos Gyulassy and Xin-Nian Wang. Hijing 1.0: A monte carlo program for parton and particle production in high-energy hadronic and nuclear collisions. *Comput. Phys. Commun.*, 83:307, 1994.
- [23] D. Ouerdane. *Charged Pion and Kaon Production in Central Au+Au Collisions at $\sqrt{s_{NN}} = 200$ GeV*. PhD thesis, Niels Bohr Institute, 2003.
- [24] P. H. L. Christiansen. *Stopping in central $\sqrt{s} = 200$ GeV Au+Au collisions at RHIC*. PhD thesis, Niels Bohr Institute, 2003.
- [25] J. D. Bjorken. Highly relativistic nucleus-nucleus collisions: The central rapidity region. *Phys. Rev.*, D27:140–151, 1983.
- [26] L.D. Landau and S.Z. Belenkij. *Nuovo Cimento Supplement*, 3:15, 1956.
- [27] Hans J. Specht. Experimental conference summary. *Nucl. Phys.*, A698:341–359, 2002.
- [28] J. Adams et al. Experimental and theoretical challenges in the search for the quark gluon plasma: The STAR collaboration’s critical assessment of the evidence from RHIC collisions. *Nucl. Phys.*, A757:102–183, 2005.
- [29] B. B. Back et al. The PHOBOS perspective on discoveries at rhic. *Nucl. Phys.*, A757:28–101, 2005.
- [30] I. Arsene et al. Quark gluon plasma and color glass condensate at RHIC? the perspective from the BRAHMS experiment. *Nucl. Phys.*, A757:1–27, 2005.
- [31] K. Adcox et al. Formation of dense partonic matter in relativistic nucleus nucleus collisions at RHIC: Experimental evaluation by the PHENIX collaboration. *Nucl. Phys.*, A757:184–283, 2005.
- [32] I. G. Bearden et al. Pseudorapidity distributions of charged particles from Au + Au collisions at the maximum RHIC energy. *Phys. Rev. Lett.*, 88:202301, 2002.
- [33] B. B. Back et al. Charged particle multiplicity near mid-rapidity in central Au + Au collisions at $s^{*(1/2)} = 56$ -a/GeV and 130-a/GeV. *Phys. Rev. Lett.*, 85:3100–3104, 2000.
- [34] I. G. Bearden et al. Charged particle densities from Au + Au collisions at $s(\text{nn})^{*(1/2)} = 130$ -GeV. *Phys. Lett.*, B523:227–233, 2001.
- [35] B. B. Back et al. Centrality dependence of the charged particle multiplicity near mid-rapidity in Au + Au collisions at $s(\text{nn})^{*(1/2)} = 130$ -GeV and 200-GeV. *Phys. Rev.*, C65:061901, 2002.
- [36] B. B. Back et al. Comparison of the total charged-particle multiplicity in high-energy heavy ion collisions with $e^+ e^-$ and $p \bar{p}$ / anti- $p \bar{p}$ data. 2003.
- [37] K. Adcox et al. Centrality dependence of charged particle multiplicity in Au Au collisions at $s(\text{n n})^{*(1/2)} = 130$ -GeV. *Phys. Rev. Lett.*, 86:3500–3505, 2001.
- [38] I. Arsene et al. Centrality dependent particle production at $y = 0$ and y approx. 1 in Au + Au collisions at $s(\text{nn})^{*(1/2)} = 200$ - GeV. *Phys. Rev.*, C72:014908, 2005.
- [39] G. Gatoff and C. Y. Wong. Origin of the soft $p(t)$ spectra. *Phys. Rev.*, D46:997–1006, 1992.

- [40] Richard Witt. systematics and $m(t)$ -scaling. 2004.
- [41] Philip J. Siemens and John O. Rasmussen. Evidence for a blast wave from compressed nuclear matter. *Phys. Rev. Lett.*, 42:880–887, 1979.
- [42] J. Adams et al. Identified particle distributions in p p and Au + Au collisions at $s^{1/2} = 200$ -GeV. *Phys. Rev. Lett.*, 92:112301, 2004.
- [43] I. G. Bearden et al. Rapidity dependence of charged antihadron to hadron ratios in Au + Au collisions at $s^{1/2} = 200$ -GeV. *Phys. Rev. Lett.*, 90:102301, 2003.
- [44] P. Braun-Munzinger, J. Stachel, and Christof Wetterich. Chemical freeze-out and the QCD phase transition temperature. *Phys. Lett.*, B596:61–69, 2004.
- [45] F. Becattini, J. Cleymans, A. Keranen, E. Suhonen, and K. Redlich. Features of particle multiplicities and strangeness production in central heavy ion collisions between 1.7-a-GeV/c and 158-a-GeV/c. *Phys. Rev.*, C64:024901, 2001.
- [46] S. S. Adler et al. Identified charged particle spectra and yields in Au + Au collisions at $s^{1/2} = 200$ -GeV. *Phys. Rev.*, C69:034909, 2004.
- [47] I. Arsene et al. Transverse momentum spectra in Au + Au and d + Au collisions at $s^{1/2} = 200$ -GeV and the pseudorapidity dependence of high $p(t)$ suppression. *Phys. Rev. Lett.*, 91:072305, 2003.
- [48] J. Adams et al. Transverse momentum and collision energy dependence of high $p(t)$ hadron suppression in Au + Au collisions at ultrarelativistic energies. *Phys. Rev. Lett.*, 91:172302, 2003.
- [49] S. S. Adler et al. High- $p(t)$ charged hadron suppression in Au + Au collisions at $s^{1/2} = 200$ -GeV. *Phys. Rev.*, C69:034910, 2004.
- [50] B. B. Back et al. Charged hadron transverse momentum distributions in Au + Au collisions at $s^{1/2} = 200$ -GeV. *Phys. Lett.*, B578:297–303, 2004.
- [51] J. W. Cronin et al. Production of hadrons with large transverse momentum at 200-GeV, 300-GeV, and 400-GeV. *Phys. Rev.*, D11:3105, 1975.
- [52] R. Baier, Yuri L. Dokshitzer, S. Peigne, and D. Schiff. Induced gluon radiation in a QCD medium. *Phys. Lett.*, B345:277–286, 1995.
- [53] Peter F. Kolb and Ulrich W. Heinz. Hydrodynamic description of ultrarelativistic heavy-ion collisions. *Invited review for 'Quark Gluon Plasma 3'*, 2003.
- [54] I. G. Bearden et al. Nuclear stopping in Au + Au collisions at $s^{1/2} = 200$ -GeV. *Phys. Rev. Lett.*, 93:102301, 2004.
- [55] F. Videbaek and O. Hansen. Baryon rapidity loss and mid-rapidity stacking in high-energy nucleus-nucleus collisions. *Phys. Rev.*, C52:2684–2693, 1995.
- [56] D. Kharzeev. Can gluons trace baryon number? *Phys. Lett.*, B378:238–246, 1996.
- [57] A. Capella and B. Z. Kopeliovich. Novel mechanism of nucleon stopping in heavy ion collisions. *Phys. Lett.*, B381:325–330, 1996.
- [58] S. E. Vance, M. Gyulassy, and X. N. Wang. Baryon number transport via gluonic junctions. *Phys. Lett.*, B443:45–50, 1998.
- [59] Miklos Gyulassy and Larry McLerran. New forms of QCD matter discovered at RHIC. *Nucl. Phys.*, A750:30–63, 2005.
- [60] F. Karsch. The phase transition to the quark gluon plasma: Recent results from lattice calculations. *Nucl. Phys.*, A590:367c–382c, 1995.

- [61] J. Breitweg et al. Measurement of the proton structure function f_2 at very low q^{*2} at hermes. *Phys. Lett.*, B487:53–73, 2000.
- [62] C. Adloff et al. Deep-inelastic inclusive $e p$ scattering at low x and a determination of $\alpha(s)$. *Eur. Phys. J.*, C21:33–61, 2001.
- [63] S. Chekanov et al. Measurement of the neutral current cross section and f_2 structure function for deep inelastic $e^+ p$ scattering at hermes. *Eur. Phys. J.*, C21:443–471, 2001.
- [64] L. V. Gribov, E. M. Levin, and M. G. Ryskin. Semihard processes in qcd. *Phys. Rept.*, 100:1–150, 1983.
- [65] Alfred H. Mueller and Jian-wei Qiu. Gluon recombination and shadowing at small values of x . *Nucl. Phys.*, B268:427, 1986.
- [66] A. M. Stasto, K. Golec-Biernat, and J. Kwiecinski. Geometric scaling for the total $\gamma^* p$ cross-section in the low x region. *Phys. Rev. Lett.*, 86:596–599, 2001.
- [67] J. Breitweg et al. Measurement of the proton structure function f_2 and $\sigma(\text{tot})(\gamma^* p)$ at low q^{*2} and very low x at hermes. *Phys. Lett.*, B407:432–448, 1997.
- [68] Larry D. McLerran and Raju Venugopalan. Computing quark and gluon distribution functions for very large nuclei. *Phys. Rev.*, D49:2233–2241, 1994.
- [69] Edmond Iancu, Andrei Leonidov, and Larry D. McLerran. Nonlinear gluon evolution in the color glass condensate. i. *Nucl. Phys.*, A692:583–645, 2001.
- [70] Adrian Dumitriu and Jamal Jalilian-Marian. Scattering of gluons from the color glass condensate. *Phys. Lett.*, B547:15–20, 2002.
- [71] Daniel Stump et al. Inclusive jet production, parton distributions, and the search for new physics. *JHEP*, 10:046, 2003.
- [72] S. S. Adler et al. Mid-rapidity neutral pion production in proton proton collisions at $s^{*1/2} = 200\text{-GeV}$. *Phys. Rev. Lett.*, 91:241803, 2003.
- [73] T. Regge. *Nuovo Cimento*, 14:951, 1959.
- [74] V.N. Gribov. *Sov. Phys. JETP*, 53:654, 1967.
- [75] F. M. Liu et al. Multi-strange baryon production from identical pomerons in proton proton collisions. 2002.
- [76] Bo Andersson, G. Gustafson, G. Ingelman, and T. Sjostrand. Parton fragmentation and string dynamics. *Phys. Rept.*, 97:31, 1983.
- [77] G. Veneziano. Construction of a crossing - symmetric, regge behaved amplitude for linearly rising trajectories. *Nuovo. Cim.*, A57:190–197, 1968.
- [78] K. Werner. Strings, pomerons, and the venus model of hadronic interactions at ultrarelativistic energies. *Phys. Rept.*, 232:87–299, 1993.
- [79] S. Eidelman et al. Review of particle physics. *Phys. Lett.*, B592:1, 2004.
- [80] Xavier Artru. Classical string phenomenology. 1. how strings work. *Phys. Rept.*, 97:147, 1983.
- [81] K. Werner, F. M. Liu, S. Ostapchenko, and T. Pierog. A new string model: Nexus 3. *Heavy Ion Phys.*, 21:279–285, 2004.
- [82] M. Basile et al. The 'leading' baryon effect in strong, weak, and electromagnetic interactions. *Nuovo Cim. Lett.*, 32:321, 1981.
- [83] J. Benecke, T. T. Chou, Chen-Ning Yang, and E. Yen. Hypothesis of limiting fragmentation in high-energy collisions. *Phys. Rev.*, 188:2159–2169, 1969.

- [84] G. Bellettini et al. Experimental tests of limiting fragmentation at the isr. *Phys. Lett.*, B45:69–72, 1973.
- [85] P. Deines-Jones et al. Charged particle production in the pb + pb system at 158- GeV/c per nucleon. *Phys. Rev.*, C62:014903, 2000.
- [86] B. B. Back et al. The significance of the fragmentation region in ultrarelativistic heavy ion collisions. *Phys. Rev. Lett.*, 91:052303, 2003.
- [87] V. Topor Pop et al. Strangeness enhancement in p + a and s + a interactions at sps energies. *Phys. Rev.*, C52:1618–1629, 1995.
- [88] B. Z. Kopeliovich and B. G. Zakharov. Novel mechanisms of baryon number flow over large rapidity gap. *Z. Phys.*, C43:241, 1989.
- [89] A. Capella, E. G. Ferreira, and C. A. Salgado. Baryon and antibaryon production in hadronic and nuclear interactions. *Phys. Lett.*, B459:27–32, 1999.
- [90] G. C. Rossi and G. Veneziano. A possible description of baryon dynamics in dual and gauge theories. *Nucl. Phys.*, B123:507, 1977.
- [91] Horst Stoecker and W. Greiner. High-energy heavy ion collisions: Probing the equation of state of highly excited hadronic matter. *Phys. Rept.*, 137:277–392, 1986.
- [92] R. B. Clare and D. Strottman. Relativistic hydrodynamics and heavy ion reactions. *Phys. Rept.*, 141:177–280, 1986.
- [93] J. Brachmann et al. Non-equilibrium fluid-dynamics in the early stage of ultrarelativistic heavy-ion collisions. *Nucl. Phys.*, A619:391–412, 1997.
- [94] Torbjorn Sjostrand, Leif Lonnblad, Stephen Mrenna, and Peter Skands. Pythia 6.3: Physics and manual. 2003.
- [95] R. Engel and J. Ranft. Hadronic photon-photon interactions at high energies. *Phys. Rev.*, D54:4244–4262, 1996.
- [96] S. A. Bass et al. Microscopic models for ultrarelativistic heavy ion collisions. *Prog. Part. Nucl. Phys.*, 41:225–370, 1998.
- [97] L.I. Sarycheva L.N. Smirnova N.S. Amelin, L.V. Bravina. *Sov. J. Nucl. Phys.*, 51:327, 1990.
- [98] S. E. Vance, M. Gyulassy, and X. N. Wang. Baryon junction stopping at the sps and RHIC via hijing/b. *Nucl. Phys.*, A638:395c–398c, 1998.
- [99] A. Capella, U. Sukhatme, C-I Tan, and J. Tran Thanh Van. Dual parton model. *Phys. Rept.*, 236:225–329, 1994.
- [100] K. Geiger. Space-time description of ultrarelativistic nuclear collisions in the QCD parton picture. *Phys. Rept.*, 258:237–376, 1995.
- [101] J. Aichelin and Horst Stoecker. Quantum molecular dynamics. a novel approach to n body correlations in heavy ion collisions. *Phys. Lett.*, B176:14–19, 1986.
- [102] V.N. Gribov. *Sov. Phys. JETP*, 14:478 and 1395, 1961.
- [103] A. B. Kaidalov. Regge poles in QCD. 2001.
- [104] G. Calucci and D. Treleani. Mini - jets: Cross-section and energy distribution in very high-energy nuclear collisions. *Phys. Rev.*, D41:3367, 1990.
- [105] Bo Andersson, G. Gustafson, and B. Nilsson-Almqvist. A model for low p(t) hadronic reactions, with generalizations to hadron - nucleus and nucleus-nucleus collisions. *Nucl. Phys.*, B281:289, 1987.

- [106] Xin-Nian Wang and Miklos Gyulassy. A systematic study of particle production in p + p (anti-p) collisions via the hijing model. *Phys. Rev.*, D45:844–856, 1992.
- [107] V. Topor Pop et al. Baryon junction loops in hijing/banti-b v2.0 and the baryon/meson anomaly at RHIC. *Phys. Rev.*, C70:064906, 2004.
- [108] F. Becattini and Ulrich W. Heinz. Thermal hadron production in p p and p anti-p collisions. *Z. Phys.*, C76:269–286, 1997.
- [109] Francesco Becattini. Hadrosynthesis at sps and RHIC and the statistical model. *J. Phys.*, G28:1553–1560, 2002.
- [110] F. M. Liu, K. Werner, J. Aichelin, M. Bleicher, and Horst Stoecker. A micro-canonical description of hadron production in proton proton collisions. *J. Phys.*, G30:S589–S594, 2004.
- [111] Francesco Becattini. A thermodynamical approach to hadron production in e+ e- collisions. *Z. Phys.*, C69:485–492, 1996.
- [112] P. Braun-Munzinger, D. Magestro, K. Redlich, and J. Stachel. Hadron production in Au Au collisions at RHIC. *Phys. Lett.*, B518:41–46, 2001.
- [113] A. Andronic, P. Braun-Munzinger, and J. Stachel. Hadron production in central nucleus nucleus collisions at chemical freeze-out. 2005.
- [114] M. Antinucci et al. Multiplicities of charged particles up to isr energies. *Lett. Nuovo Cim.*, 6:121–128, 1973.
- [115] M. Aguilar-Benitez et al. Inclusive particle production in 400-GeV/c p p interactions. *Z. Phys.*, C50:405–426, 1991.
- [116] C. Alt et al. Inclusive production of charged pions in p p collisions at 158-GeV/c beam momentum. 2005.
- [117] C. Höhne. *System-Size Dependence of Strangeness Production in Heavy-Ion Collisions at 158 AGeV*. PhD thesis, Fachbereich Physik, Philipps-Universität Marburg, 2003. <http://archiv.ub.uni-marburg.de/diss/z2003/0627/>.
- [118] J. Adams et al. Pion, kaon, proton and anti-proton transverse momentum distributions from p + p and d + Au collisions at $s(\text{nn})^{1/2} = 200\text{-GeV}$. *Phys. Lett.*, B616:8–16, 2005.
- [119] Lijuan Ruan. Pion, kaon, proton and antiproton spectra in d + Au and p + p collisions at $s(\text{nn})^{1/2} = 200\text{-GeV}$ at the relativistic heavy ion collider. 2005.
- [120] E. F. Matathias. *Identified Particle Production in p+p and d+Au Collisions at RHIC Energies*. PhD thesis, Stony Brook University, 2004. Available at <http://www.phenix.bnl.gov/thesis.html>.
- [121] M. Adamczyk et al. The BRAHMS experiment at RHIC. *Nucl. Instrum. Meth.*, A499:437–468, 2003.
- [122] H. Hahn et al. The RHIC design overview. *Nucl. Instrum. Meth.*, A499:245–263, 2003.
- [123] K. H. Ackermann et al. STAR detector overview. *Nucl. Instrum. Meth.*, A499:624–632, 2003.
- [124] K. Adcox et al. PHENIX detector overview. *Nucl. Instrum. Meth.*, A499:469–479, 2003.
- [125] B. B. Back et al. The PHOBOS detector at RHIC. *Nucl. Instrum. Meth.*, A499:603–623, 2003.
- [126] S. Bultmann et al. The PP2PP experiment at RHIC: Silicon detectors installed in roman pots for forward proton detection close to the beam. *Nucl. Instrum. Meth.*, A535:415–420, 2004.

- [127] *GEANT Detector Description and Simulation Tool*. Available from <http://wwwasd.web.cern.ch/wwwasd/geant/>.
- [128] Pawel Staszal. BRAHMS analysis notes 27, 29, 34 and 38. Technical report.
- [129] Radek Karabowicz. Master's thesis, University of Krakow, 2002.
- [130] E. J. Kim and F. Videbaek. Private communication.
- [131] E. J. Kim. Private communication. See <http://kunuc10.phsx.ku.edu/ejkim/brahms/LambdaCorrection/lambdaFS.html>.
- [132] T. M. "Larsen. "efficiency calculations for the time projection chambers in the BRAHMS experiment at the RHIC accelerator". Master's thesis, University of Oslo, 2003.
- [133] H. Ito. Private communication.
- [134] J. Adams et al. Evidence from d + Au measurements for final-state suppression of high p(t) hadrons in Au + Au collisions at RHIC. *Phys. Rev. Lett.*, 91:072304, 2003.
- [135] S. S. Adler et al. Absence of suppression in particle production at large transverse momentum in $s(nn)^{1/2} = 200$ -GeV d + Au collisions. *Phys. Rev. Lett.*, 91:072303, 2003.
- [136] B. B. Back et al. Centrality dependence of charged hadron transverse momentum spectra in d + Au collisions at $s(nn)^{1/2} = 200$ -GeV. *Phys. Rev. Lett.*, 91:072302, 2003.
- [137] Dmitri Kharzeev, Yuri V. Kovchegov, and Kirill Tuchin. Nuclear modification factor in d + Au collisions: Onset of suppression in the color glass condensate. *Phys. Lett.*, B599:23–31, 2004.
- [138] Jamal Jalilian-Marian and Yuri V. Kovchegov. Saturation physics and deuteron gold collisions at RHIC. *Prog. Part. Nucl. Phys.*, 56:104–231, 2006.
- [139] Klaus Werner, Fu-Ming Liu, and Tanguy Pierog. Parton ladder splitting and the rapidity dependence of transverse momentum spectra in deuteron gold collisions at RHIC. 2005.
- [140] Larry McLerran. RHIC physics: The quark gluon plasma and the color glass condensate: 4 lectures. 2003.
- [141] Alberto Accardi and Miklos Gyulassy. Cronin effect and geometrical shadowing in d + Au collisions: pQCD vs. CGC. *J. Phys.*, G30:S969–S974, 2004.
- [142] Marta Czech and Antoni Szczurek. Unintegrated parton distributions and pion production in p p collisions at RHIC's energies. 2005.
- [143] (ed.) Carminati, F. et al. ALICE: Physics performance report, volume i. *J. Phys.*, G30:1517–1763, 2004.
- [144] Mark Heinz. Strange particle production in p + p collisions at $s^{1/2} = 200$ -GeV. *J. Phys.*, G31:S1011, 2005.
- [145] Wojciech Broniowski and Wojciech Florkowski. Strange particle production at RHIC in a single-freeze-out model. *Phys. Rev.*, C65:064905, 2002.
- [146] *ROOT Users Manual*. Available from <http://root.cern.ch>.